CONTROL DESIGN AND PERFORMANCE EVALUATION OF A HYBRID FLEXURE BEARING FOR PRECISION POINTING APPLICATIONS

BY

NATHAN ANDREW WEIR

DISSERTATION

Submitted in partial fulfillment of the requirements
for the degree of Doctor of Philosophy in Mechanical Engineering
in the Graduate College of the
University of Illinois Urbana-Champaign, 2022

Urbana, Illinois

Doctoral Committee:

Professor Andrew Alleyne, Chair and Director of Research
Professor Srinivasa Salapaka
Professor Ramavarapu Sreenivas
Professor William Messner, Carnegie Mellon University

Abstract

Gimbaled pointing systems are commonly used to aim and stabilize sensitive instrument payloads such as lasers, radars, cameras, and other electro-optical/infrared (EO/IR) sensors for a variety of commercial, scientific, and military applications. For precision imaging systems, overall performance is tied directly to the pointing system's ability to accurately point toward a target in inertial space and to reject disturbances that cause undesirable line of sight (LOS) motion. Any residual or uncompensated LOS motion, known as jitter, can degrade the quality of the captured images. The jitter requirements for future systems grow even more demanding as image sensor performance and resolution continue to improve, resulting in smaller pixel size and higher pixel densities. Thus, there is a critical need for improved jitter reduction techniques to enable the deployment of future higher-resolution imaging systems.

This research effort is motivated by a hybrid flexure bearing concept which was developed to reduce the effects of friction that degrade performance in precision pointing systems with conventional ball bearing joints. The hybrid flexure bearing concept combines the large travel advantage of a conventional ball bearing joint with the smooth, repeatable, and frictionless motion of a rotational flexure. This research seeks to advance the state-of-the-art in precision pointing through modeling, control design, and experimental evaluation of the hybrid flexure bearing concept.

A significant challenge associated with the development of precision motion control systems is the identification and modeling of friction. An accurate friction model is crucial for assessing the impact of bearing friction on pointing performance. A data-based dynamic friction model is proposed, which significantly improves friction model accuracy in both the time and frequency domains. Key friction model features are identified to better match frictional behavior observed in experiments. Simulation results are validated with measured friction data collected from the experimental testbed.

The closed-loop properties of general two-input single-output (TISO) feedback systems are described using the concepts of plant/controller alignment. In general, we show that it is desirable to design a controller that is well aligned with the plant in order to minimize the size of the closed-loop sensitivity functions and closed-loop interactions. A new graphical controller design approach is proposed which exploits the concept of plant/controller alignment using alignment contours on the conventional Bode plot. The utility of the approach is shown through its application to the hybrid flexure bearing system. The performance of a well-aligned and poorly aligned controller are evaluated in simulation and validated with an experimental testbed under a variety of base motion disturbances. Lastly, model-based friction compensation techniques are investigated using the data-based friction model. The overall pointing performance is improved by using a well-aligned controller and the data-based friction compensation approach, reducing both jitter and control energy usage.

To Amy, for her sacrifice.

Acknowledgments

There are many people who helped me complete this work. First of all, I would like to thank my advisor, Andrew Alleyne, for his guidance, insight, and eternal patience throughout my doctoral studies. Also, thanks to my committee members, Srinivasa Salapaka, R.S. Sreenivas, and Bill Messner for their helpful comments and constructive feedback. Thanks to those who made my time at the University of Illinois a more enjoyable experience, especially to the members of ARG — Justin, Malia, Herschel, Matt, Ashley, Pamela, Oyuna, Bryan, Spencer K., Spencer I., Sunny, Sarah, and Chris — for welcoming me into the fold and fostering a collaborative environment. It was refreshing to work with such a friendly, talented, and ambitious group of individuals.

Many thanks to those who have greatly impacted my career at Sandia. My deepest gratitude to Randy Rosenthal for making the experimental work possible. I am also grateful to those who have mentored me over the years and helped me grow as an engineer. Special thanks to Tony Smith, Pat Barney, and Ted Kim. Also, thanks to Steve Rodriguez, Mark Terhune, and Jason Payne for supporting me along the way — through the Doctoral Study Program and beyond.

Finally, I am indebted to my beautiful family — Amy, Audrey, and Parker — who endured this long journey with me. None of this would have been possible without their love, sacrifice, support, and encouragement. I am deeply grateful to them for giving me the opportunity.

Financial support for this research effort was provided by Sandia National Laboratories. Sandia is a multi-mission laboratory managed and operated by National Technology and Engineering Solutions of Sandia (NTESS), LLC, a wholly owned subsidiary of Honeywell International, Inc., for the U.S. Department of Energy's National Nuclear Security Administration under contract DE-NA-0003525. This dissertation has been authored by an employee of NTESS and describes objective technical results and analysis. The employee owns all right, title and interest in and to the dissertation and is solely responsible for its contents. Any subjective views or opinions that

might be expressed in the dissertation do not necessarily represent the views of the U.S. Department of Energy or the United States Government.

Table of Contents

List of Tables

List of Figures

List of Abbreviations

AC	Autocollimator
A/D	Analog-to-digital
ARS	Angular rate sensor
BLDC	Brushless DC (motor)
CLTF	Closed-loop transfer function
CSP	Cumulative spectral power
D/A	Digital-to-analog
DB-DHM	Data-based dynamic hysteresis model
DB-SFM	Data-based solid friction model
DHM	Dynamic hysteresis model
DOF	Degree(s) of freedom
EDM	Electrical discharge machining
EMF	Electromotive force
EO	Electro-optical
EOM	Equation(s) of motion
FEA	Finite element analysis
FOR	Field of regard
FRF	Frequency response function
FSM	Fast steering mirror
GM	Gain margin
GMS	Generalized Maxwell-slip
GUI	Graphical user interface

HDD	Hard disk drive
ID	Inner diameter
IMU	Inertial measurement unit
I/O	Input/output
IR	Infrared (radiation)
ISP	Inertially stabilized platform
LOS	Line of sight
LQG	Linear quadratic Gaussian
LTI	Linear time invariant
LTR	Loop transfer recovery
LUT	Look up table
MEMS	Microelectromechanical systems
MIMO	Multiple-input multiple-output
MOI	Moment of inertia
NMP	Non-minimum phase
OD	Outer diameter
ODE	Ordinary differential equation
OLTF	Open-loop transfer function
ORHP	Open right half plane
PD	Proportional derivative
PI	Proportional integral
PID	Proportional integral derivative
PM	Phase margin
PSD	Power spectral density
RMS	Root mean square
SFM	Solid friction model
SISO	Single-input single-output
SITO	Single-input two-output
SWaP	Size, weight, and power

TISO	Two-input single-output
TITO	Two-input two-output
VCM	Voice coil motor

List of Symbols

δ	Flexure deflection
ϕ	Relative angle
ϕ_1	Relative outer axis angle
ϕ_2	Relative inner axis angle
θ_b	Inertial base angle
θ	Inertial LOS angle
θ_1	Inertial outer axis angle
θ_2	Inertial inner axis angle
J	1-DOF testbed moment of inertia
J_1	2-DOF testbed outer axis moment of inertia
J_2	2-DOF testbed inner axis moment of inertia
k	Flexure stiffness
b	Flexure damping coefficient
k_f	Ball bearing linearized frictional stiffness
b_f	Ball bearing viscous friction coefficient
T_f	Ball bearing friction torque
T_m	BLDC motor torque (1-DOF testbed)
T_1	BLDC motor torque (2-DOF testbed)
T_2	VCM torque
σ	Dahl rest stiffness
T_c	Dahl running (or Coulomb) torque
α	Dahl shape factor

$\frac{dT}{d\theta}$	Friction slope function
u	Control input
y	Measured output
e	Measured error
d_i	Input disturbance
d_o	Output disturbance
n	Measurement noise
r	Reference input
C	Controller transfer matrix
G	Plant transfer matrix
L_I	Input loop transfer function
L_O	Output loop transfer function
S_I	Input sensitivity
S_O	Output sensitivity
T_I	Input complementary sensitivity
T_O	Output complementary sensitivity
$\phi(j\omega)$	Plant/controller alignment angle
g_1, g_2	Plant elements
c_1, c_2	Controller elements
c_0	Post-compensator
c_1', c_2'	Pre-compensator elements
P	Plant ratio
Q	Controller ratio
L_{PQ}	PQ loop transfer function
S_{PQ}	PQ sensitivity
T_{PQ}	PQ complementary sensitivity
M_a	Alignment magnitude contour
Φ_a	Alignment phase contour
$\mathcal{C}(L_O^*)$	Set of output equivalent controllers

ΔT_i	Sensor integration period
$\Delta\theta_i$	LOS motion over a sensor integration period
$\lvert\cdot\rvert$	Magnitude
$\angle$	Phase
$\lVert\cdot\rVert$	Induced matrix norm (i.e., maximum singular value) or standard vector 2-norm
$\mathcal{R}(\cdot)$	Column space
$\mathcal{R}_{\text{row}}(\cdot)$	Row space
$\overline{X}$	Complex conjugate of X

Chapter 1

Introduction

1.1 Background and Motivation

Inertially stabilized platforms (ISPs) are commonly used to aim and stabilize sensitive instrument payloads such as lasers, radars, cameras, and other electro-optical/infrared (EO/IR) sensors for a variety of commercial, scientific, and military applications [1]. Each application imposes different pointing requirements due to their unique objectives and operating environments. These applications span a wide spectrum, from consumer-grade handheld gimbals for stabilized photography and videography [2], to dedicated platforms like the Hubble or James Webb space telescopes for ultra-high pointing performance in astronomy [3].

This research effort focuses on the class of pointing systems which utilize a gimbal to suspend/isolate, orient, and stabilize a payload. A gimbal is an assembly of structure, bearings, and motors to which a payload is mounted and often carried on a wide variety of moving host vehicles, such as ground vehicles, ships, aircraft, and spacecraft. A typical two-axis gimbal, depicted in Fig. 1.1, provides the ability to 1) point the payload in a desired direction over a large field of regard (FOR), and 2) stabilize the payload line of sight (LOS) in the presence of base disturbances due to host vehicle motion. A gyroscope (or gyro), which senses rotational motion in inertial space, is directly mounted to the payload or gimbal assembly. Typically, the gyro is the primary feedback sensor used in the pointing control system.

Pointing requirements depend on many factors, but are primarily driven by the performance characteristics of the payload or instrument being stabilized. For imaging systems, overall performance is tied directly to the pointing system's ability to accurately point toward a target in inertial space and to reject disturbances that cause undesirable LOS motion. Any residual or uncompensated LOS motion, known as *jitter* [4], can degrade the quality of the captured images as

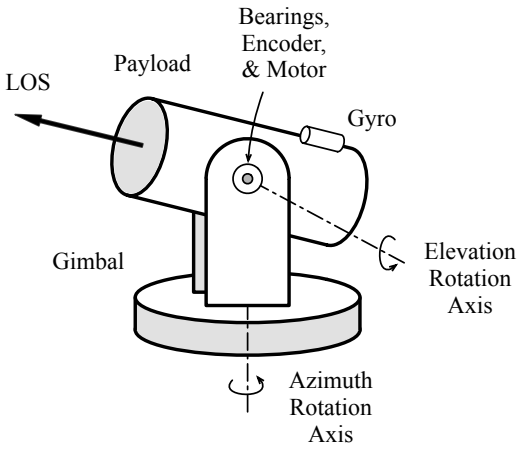

Figure 1.1: Two-axis gimbaled pointing system

depicted in Fig. 1.2. To avoid blurring, jitter should generally produce no more than ∼1/3 of a pixel of RMS motion at the image focal plane during the sensor integration time[1] [5]. Figure 1.3 shows a sequence of images taken of a point source of light with increasing jitter levels. Increased jitter causes a loss of contrast and sharpness in the captured images, thereby reducing the ability to resolve dim or closely spaced targets.

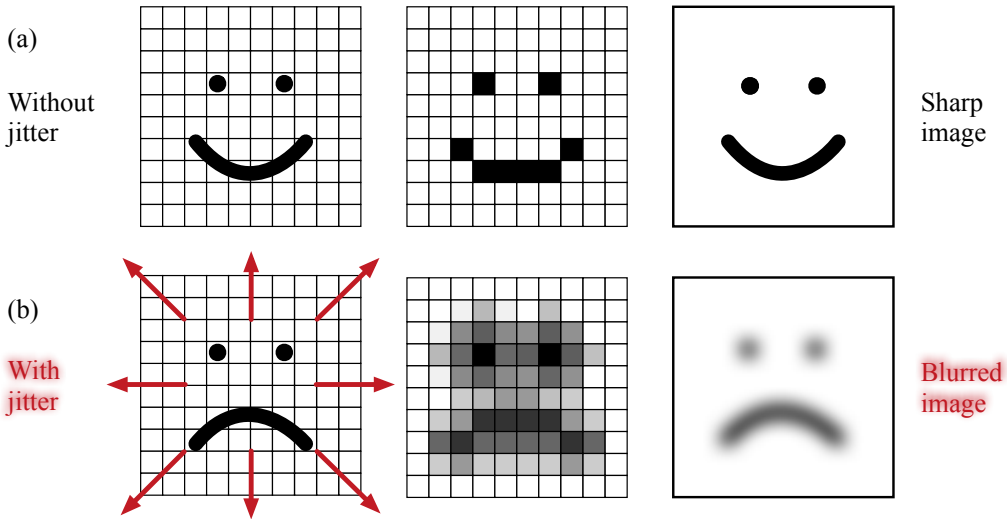

Figure 1.2: The effect of jitter on image quality: (a) without LOS motion, the ensquared energy is maximized, producing a sharp high-contrast image, (b) when LOS motion is significant, energy is smeared across multiple pixels, producing a blurred low-contrast image.

[1]The integration time is the period of time that an image sensor collects and accumulates charge due to incident photons. This is analogous to the shutter speed or exposure time in film cameras.

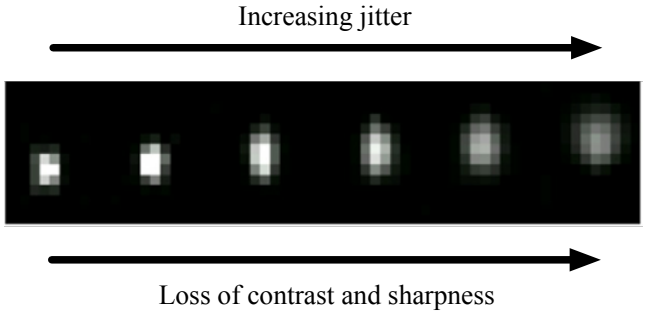

Figure 1.3: Increasing jitter causes loss of contrast and sharpness

As indicated in Fig. 1.4(a), significant performance gains have been accomplished over the past several decades. Nonetheless, the demands for better pointing and jitter continue to grow at a rapid pace. Jitter requirements for imaging systems are driven by the performance and resolution of the image sensor [4]. Optical image sensor performance and resolution have dramatically improved in recent years [6], resulting in smaller pixel size and higher pixel densities, as depicted in Fig. 1.4(b). However, the benefits of increased sensor resolution cannot be fully realized unless corresponding improvements in LOS stabilization accompany the sensor advancements [6]. Although state-of-the-art precision stabilization systems are capable of achieving jitter levels within the microradian range, the jitter requirements for future systems grow even more demanding as image sensor performance and resolution continue to improve. Thus, there is a critical need for improved jitter reduction techniques that will enable the deployment of future higher-resolution imaging systems.

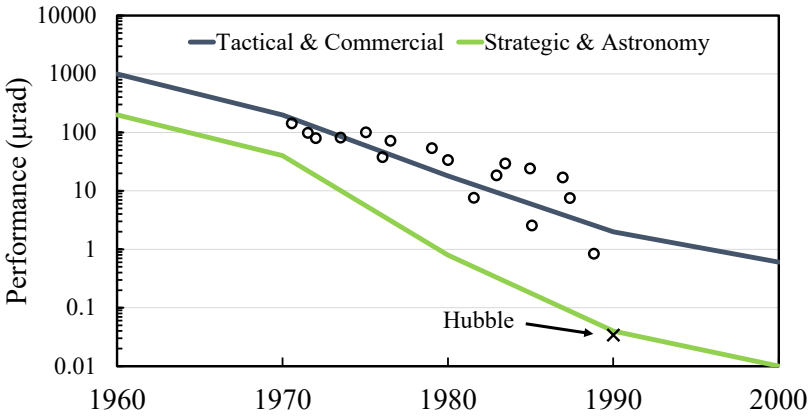

(a) Pointing performance trends (compiled from [7, 8])

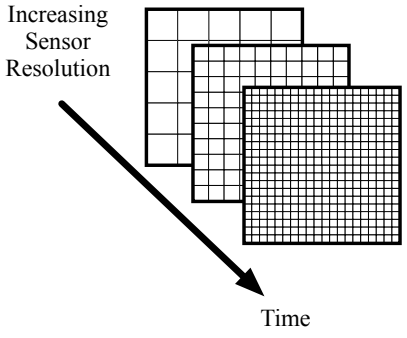

(b) Image sensor resolution trends

Figure 1.4: Pointing performance and sensor resolution trends

There are multiple disturbance sources that may contribute to LOS jitter in gimbaled pointing systems. These jitter sources can be categorized into three basic categories: structural flexibility, erroneous torque-equivalent inputs, and torque disturbances [1, 8]. Structural flexibility includes bending of the gimbal and/or displacement of optical components (e.g., lenses, mirrors) in the optical path. Structural effects are typically mitigated through appropriate stiffening of the mechanical structure. Erroneous inputs include gyro and sensor noise, quantization noise, and LOS/gyro misalignment. These effects can be minimized through appropriate sensor selection and assembly processes. Some common examples of torque disturbances include joint friction, motor cogging and ripple torques, cable stiffness, mass imbalance, and on-board shaking forces. A jitter error budget analysis is often used in the early stages of pointing system development to evaluate system-level design and hardware tradeoffs [6, 8, 9]. It is also a useful tool for identifying the significant contributors to jitter.

All the aforementioned disturbance sources will contribute to LOS jitter to some extent. However, in most applications the dominant source of jitter is due to bearing friction [6, 10]. Frictional disturbances may be attributed to ball bearing/seal friction or other rotating electrical interfaces such as cables or slip rings. For gimbaled systems, it is not uncommon for bearing disturbances to contribute more than 75% of the total error budget [8,10]. Figure 1.5 illustrates the basic principles of inertial stabilization for a single-axis gimbal. The fundamental concept behind *mass stabilization* is that the payload will stand still if no torques are applied. The inertial stabilization system utilizes an inner rate feedback loop to stabilize the LOS. Base motion disturbances are coupled to the LOS through the nonlinear bearing friction. For systems which undergo small motions with frequent velocity reversals, presliding friction effects dominate the system dynamics and the base motion disturbances and LOS become tightly coupled [11]. As a result, it can be difficult to achieve very high performance with basic linear PI or PID control design methods.

Other common control strategies used to improve performance include model-based friction compensation techniques [12], disturbance observers [13], and adaptive control methods [14]. Although these methods may help attenuate disturbances transmitted via nonlinear friction, they cannot remove their effects entirely and are sometimes difficult to implement in practice.

An alternative strategy for addressing the problem of friction is through modification of the

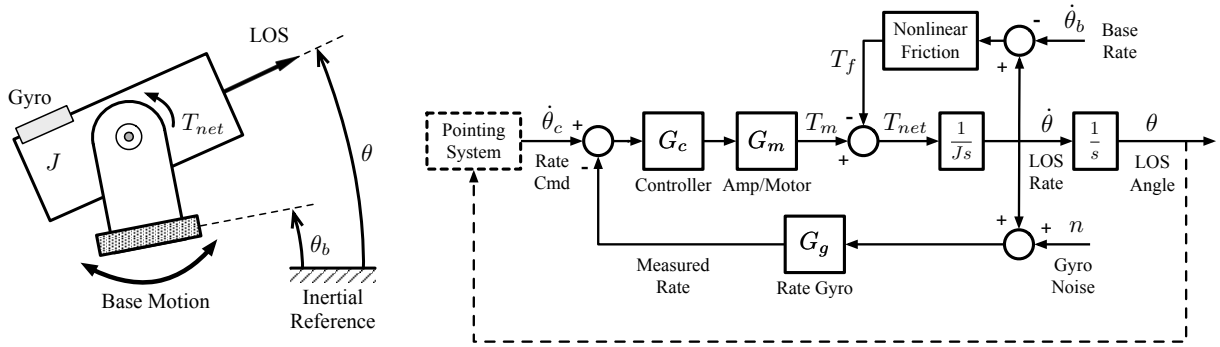

(a) Single-axis gimbal (b) Rate feedback loop

Figure 1.5: Principles of inertial stabilization

mechanical design itself. Non-contact bearing technologies such as gas lubricated bearings [15] or magnetic suspensions [16] can significantly reduce friction, but typically result in lower suspension stiffness and require additional size, weight, and power (SWaP) [1]. Fast steering mirrors (FSMs) can help correct for jitter, but require additional optical elements and feedback mechanisms within the optical path [17, 18]. High-quality precision ball bearings are commercially available, but are limited by the competing requirements for low friction versus high preload necessary for structural stiffness [19]. Furthermore, there are limited lubrication options for conventional ball bearings used in extreme environments that require vacuum compatibility and zero maintenance, such as space [15]. Flexure bearings offer several advantages over conventional ball bearings. Flexures are inherently frictionless and provide a means for smooth, linear, and repeatable motions [20]. The most significant limitation is that they can only provide a very limited range of motion. This is undesirable for most gimbaled pointing applications where it is usually necessary to point a payload over a large field of regard (FOR). To address this limitation, a hybrid approach is introduced in the following section.

1.2 Hybrid Flexure Bearing

This research effort is motivated by a hybrid flexure bearing concept which was developed to reduce the effects of friction that degrade performance in precision pointing systems with ball bearing joints [21–23]. The hybrid flexure bearing concept, depicted in Fig. 1.6, combines the large travel advantage of a conventional ball bearing joint with the smooth, repeatable, and frictionless

motion of a rotational flexure.

As shown in Fig. 1.7, incorporating the flexure provides an additional degree of freedom in the system which allows for independent actuation of both the ball bearing inner race and the relative rotation of the flexure. The ball bearing provides the large (coarse) motions required to point the LOS over a large field of regard, while the flexure provides the smooth, linear, repeatable motions for (fine) jitter control. A brushless DC (BLDC) motor serves as the primary (coarse-stage) actuator, while a set of voice coil motors (VCMs) provide the secondary (fine-stage) actuation. Additional details about the hybrid flexure bearing prototype hardware and experimental testbed are given in Chapter 2.

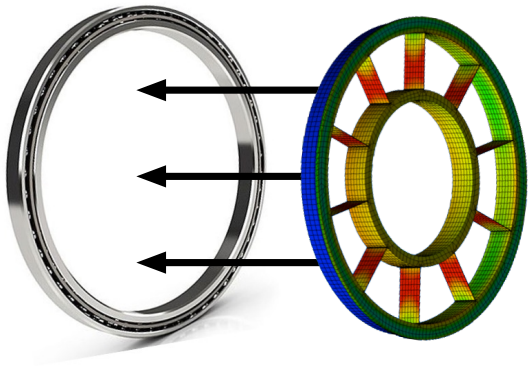

Figure 1.6: Combined ball bearing and rotational flexure joint

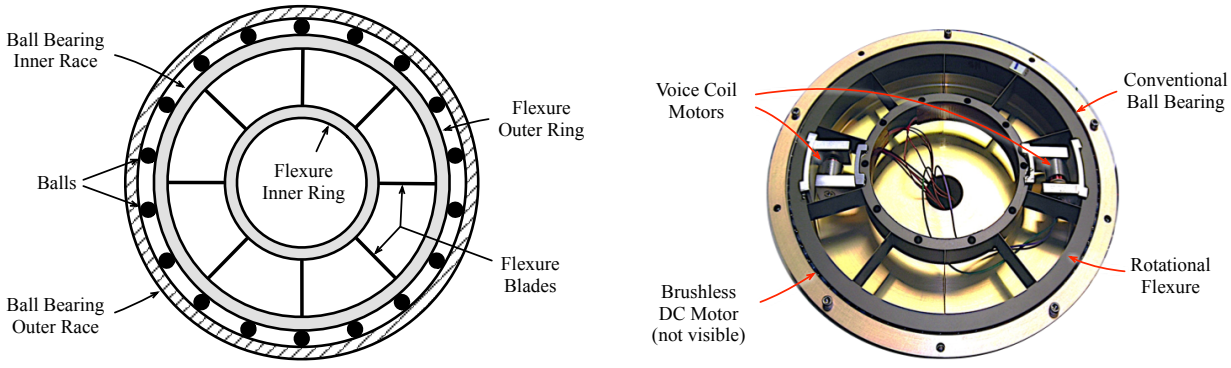

(a) (b)

Figure 1.7: Hybrid flexure bearing: (a) concept diagram and (b) prototype hardware

1.3 Research Objectives

This research seeks to advance the state-of-the-art in precision pointing through control design and evaluation of the hybrid flexure bearing concept. To achieve this goal, the following objectives are defined:

1) Develop an experimental testbed to fully characterize, model, and validate the hybrid flexure bearing prototype.
2) Develop an accurate model of the hybrid flexure bearing including nonlinear friction.
3) Identify and analyze closed-loop limitations.
4) Develop and evaluate potential control strategies for improved jitter rejection.
5) Validate control system approaches and performance with the experimental testbed.

1.4 Thesis Organization

The remainder of the thesis is organized as follows. Chapter 2 introduces the experimental system used to characterize and evaluate the hybrid flexure bearing concept. Building upon the foundations of previous work [21], this chapter describes several updates to the experimental testbed, including the integration of representative gimbal hardware and improved inertial sensors. These upgrades enable new test configurations to evaluate the hybrid flexure bearing under more realistic base disturbance environments.

Chapter 3 describes the dynamical model for the hybrid flexure bearing system. A significant challenge associated with the development of precision motion control systems is the identification and modeling of friction. In particular, dynamic (presliding) friction is often difficult to accurately model. For systems which undergo small motions with frequent velocity reversals, presliding friction effects dominate the system dynamics and the base motion disturbances and LOS become tightly coupled. An accurate friction model is crucial for assessing the impact of bearing friction on pointing performance. This chapter presents a data-based dynamic friction model that significantly improves friction model accuracy in both the time and frequency domains. Key friction model features are identified to better match frictional behavior observed in experiments. Simulation results are validated with measured friction data collected from the experimental testbed.

Chapter 4 describes the properties of general two-input single-output (TISO) feedback systems and introduces the concepts of plant and controller "directions" and "alignment". Due to the unique structure of TISO feedback systems, several closed-loop properties can be characterized using the concept of plant/controller alignment. In general, it is desirable to design a controller that is well aligned with the plant in order to minimize the size of the closed-loop sensitivity functions and closed-loop interactions. Poor plant/controller alignment indicates significant limitations in terms of closed-loop performance.

Chapter 5 introduces a graphical controller design approach for general TISO systems which exploits the concept of plant/controller alignment. Although the concept of alignment can be a useful analysis tool for a given plant/controller pair, it is not obvious how a controller should be designed to achieve good alignment. This chapter presents a new graphical design approach, based on the PQ method [24], which explicitly incorporates knowledge of alignment into the control design process.

Chapter 6 describes the application of the concepts of plant/controller alignment and the graphical control design approach to the hybrid flexure bearing testbed. Two case studies explore the performance of the hybrid flexure bearing concept. The first case study evaluates the tracking performance of the hybrid flexure testbed using relative position feedback. A design example shows the utility of the graphical control design approach using alignment contours. Two different control designs are compared: a controller that is poorly aligned with the plant, and a controller that is well aligned with the plant. The relative tracking performance of both designs are evaluated and experimentally validated. The second case study explores the impact of plant/controller alignment on the pointing performance of the hybrid flexure bearing using inertial rate feedback for LOS stabilization in the presence of base motion disturbances. The performance of a well-aligned and poorly aligned controller are evaluated in simulation and validated with the experimental testbed under a variety of base motion disturbances. Model-based friction compensation techniques are also investigated using the data-based dynamic friction model.

Finally, Chapter 7 summarizes the key contributions of this research effort and provides suggestions for future research directions.

Chapter 2

Experimental System

This chapter introduces the experimental system used to characterize and evaluate the hybrid flexure bearing concept. Building upon the foundations of previous work [21], this chapter describes several updates to the experimental testbed, including the integration of representative gimbal hardware and inertial sensors. These hardware upgrades enable new test configurations to evaluate the hybrid flexure bearing under more realistic base disturbance environments.

2.1 Flexure Design

Figure 2.1 depicts the rotational flexure design [21] evaluated in this study. The rotational flexure is a monolithic structure machined out of annealed titanium alloy (Ti-6Al-4V) using a wire electrical discharge machining (EDM) process. Additional measures were taken to minimize thermal distortions and residual stress during the manufacturing process. The outer diameter (OD) of the outer ring is 6 inches, the inner diameter (ID) of the inner ring is 3 inches, and the total part thickness is approximately 0.5 inches. The inner and outer rings of the flexure are connected by 10 equally-spaced flexure blades, arranged radially about the center of rotation. The thickness of each flexure blade is 0.01 inches.

Several design considerations were taken into account during the preliminary design phase of the flexure bearing [21]. The flexure geometry was primarily driven by the requirement to reuse/retrofit an existing gimbal design and bearing set. The form factor achieves the geometrical envelope necessary to mate with the existing ball bearing joint, and also provides an optical *coudé path* through the center of the gimbal's rotational joint.[1] The spacing between flexure blades allows sufficient clearance for the installation of actuators. The radial flexure blades provide compliance

[1] Coudé is the French word for elbow, referring to the reflection of the light path through one or more 90° turns.

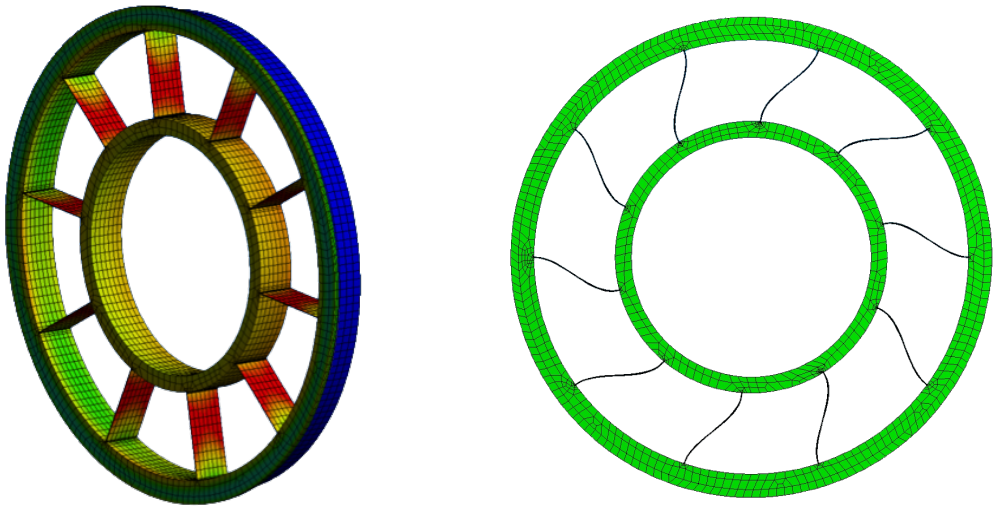

(a) (b)

Figure 2.1: Rotational flexure design [21]: (a) FEA model used for stress, thermal, and modal analysis. The color indicates the stresses as the blades deform. (b) Predicted blade deformations due to an angular displacement of 0.15° (shown at 140x scale).

(i.e., low stiffness) about the axis of rotation, while providing extremely high stiffnesses in the off-axis/lateral directions to maintain the structural integrity of the gimbal joint.

A finite element analysis (FEA) model, depicted in Fig. 2.1, was used to analyze the rotational flexure design [21]. Several different analyses were performed in [21], including linear static loading for stresses, linear static loading for stiffness (i.e., deflection analysis), modal analysis, and thermal analysis. In addition to the normal linear finite element analysis, a time-marching combined thermal-structural analysis was performed in order to evaluate changes in stiffness due to applied temperature gradients [22, 23]. The flexure was also designed to provide suitable strength for static and dynamic loads in the expected application environment.

Overall, the flexure provides excellent linearity and constant stiffness over the full range of motion, allowing up to ± 15 mrad of rotational deflection with an infinite fatigue life. The flexure can tolerate a maximum deflection of approximately ± 37 mrad before yield (i.e., permanent deformation) occurs in the flexure blades. Additional details regarding the design, analysis, and fabrication of the rotational flexure are given in [21–23]. Details about the flexure characterization, including measurement of stiffness and damping properties, can be found in Appendix A.

2.2 Testbed Description

An experimental testbed was designed and built to study the performance of the prototype hybrid flexure bearing as well as develop and evaluate potential control strategies [21]. Figure 2.2 depicts the various mechanical components that make up the original testbed assembly. The testbed is designed to be an accurate representation of a single gimbal joint used in precision pointing applications. The inner races of the ball bearings are clamped between the outer hub and the outer ring of the flexure. The outer races of the ball bearings are attached to the testbed housing by tightening the bearing clamp ring to the appropriate preload. The inner hub is attached to the inner ring of the flexure and provides a means for mounting additional sensors and payload hardware to the LOS rotation axis. A brushless DC (BLDC) motor drives the outer hub and ball bearings. The flexure is actuated by a set of voice coil motors (VCMs).

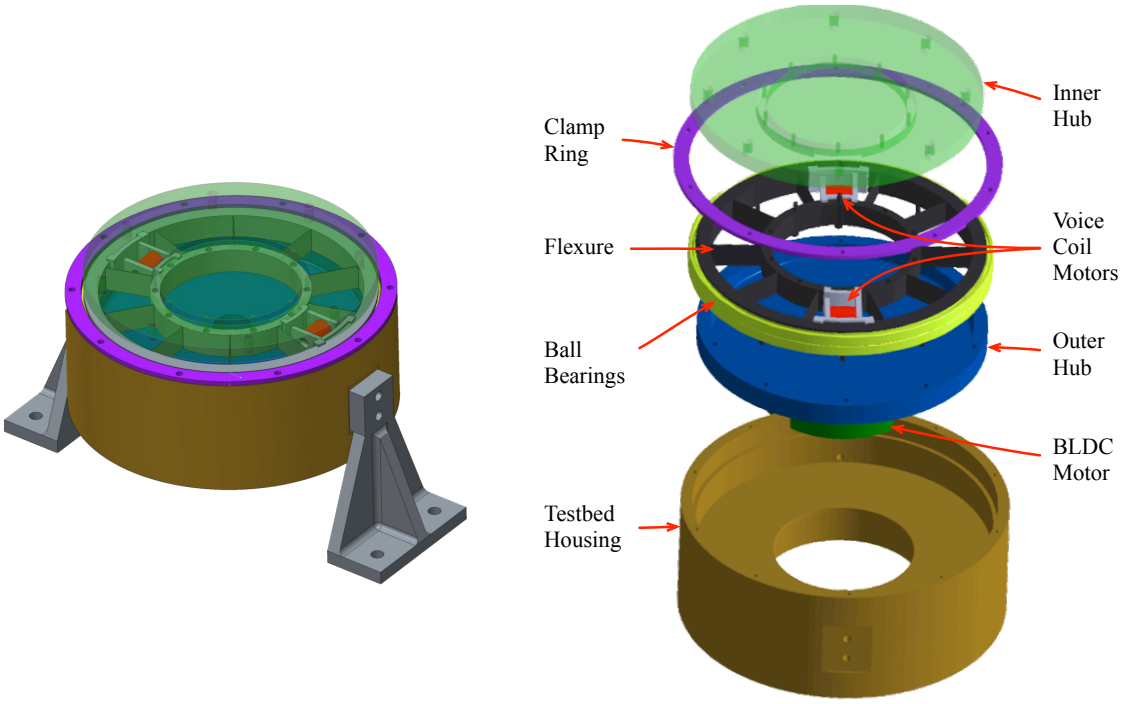

Figure 2.2: Testbed mechanical components and assembly

In this research effort, several updates are made to the experimental testbed, including the integration of representative gimbal hardware and inertial sensors. These hardware upgrades enable a new inertial test configuration to evaluate the hybrid flexure bearing under more realistic base

disturbance environments. Figure 2.3 depicts the two different experimental testbed configurations used in this work. The testbed hardware includes the components listed in Table 2.1. The two testbed configurations are described in greater detail below.

2.2.1 1-DOF testbed

The 1-DOF testbed, depicted in Fig. 2.3(a), represents a single-axis gimbal with a conventional ball bearing joint. This configuration allows for meaningful comparisons of performance between the hybrid flexure bearing and a conventional ball bearing joint. The 1-DOF testbed configuration is particularly useful for studying the frictional characteristics of the ball bearing joint. The rotation axis is suspended by a duplex pair of angular contact ball bearings. The ball bearings are precision ABEC class 7 bearings with a nominal preload of 25 lb. The ball bearing joint is actuated by a brushless DC (BLDC) motor. The BLDC motor is a slotless (toroidally wound) single-phase motor, which provides a peak torque capability of 81.3 in-oz and a limited angular excursion up to ± 20 deg. A high-resolution absolute optical encoder measures the rotation angle relative to the base. The encoder has an angular resolution of 1.5 nrad.[2] The angular rate of the LOS is measured by an inertial measurement unit (IMU) which can be mounted to the top plate during tests.

2.2.2 2-DOF testbed

The 2-DOF testbed, depicted in Fig. 2.3(b), has a nearly identical configuration to the 1-DOF testbed, with the addition of the rotational flexure joint which provides an additional degree of freedom in the system. The same BLDC torque motor serves as the primary (coarse-stage) actuator, while a set of voice coil motors (VCMs) provide the secondary (fine-stage) actuation. The VCMs are mounted in the spaces between the flexure blades and apply a tangential force between the inner and outer rings of the flexure. In early development, only two VCMs were installed into the rotational flexure [21]. For this effort, two additional VCMs were installed to provide additional torque capability. The four VCMs provide a total effective torque capability of 16.1 in-oz. The rotation of both the outer and inner axes are measured with a pair of high-resolution optical encoders. Both encoders have the same 1.5 nrad angular resolution.[2] In prior work, the relative

[2]Note that the full 32-bit resolution is below the noise floor of the encoder.

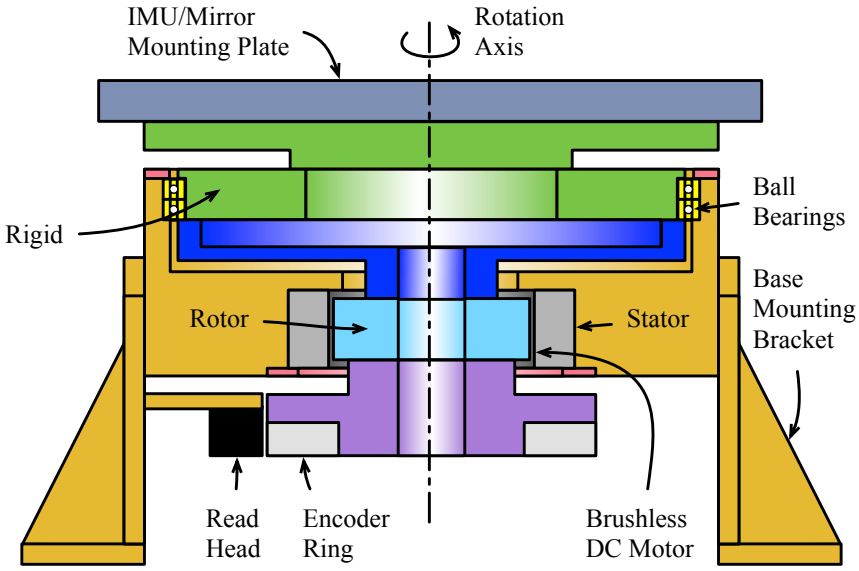

(a) 1-DOF testbed

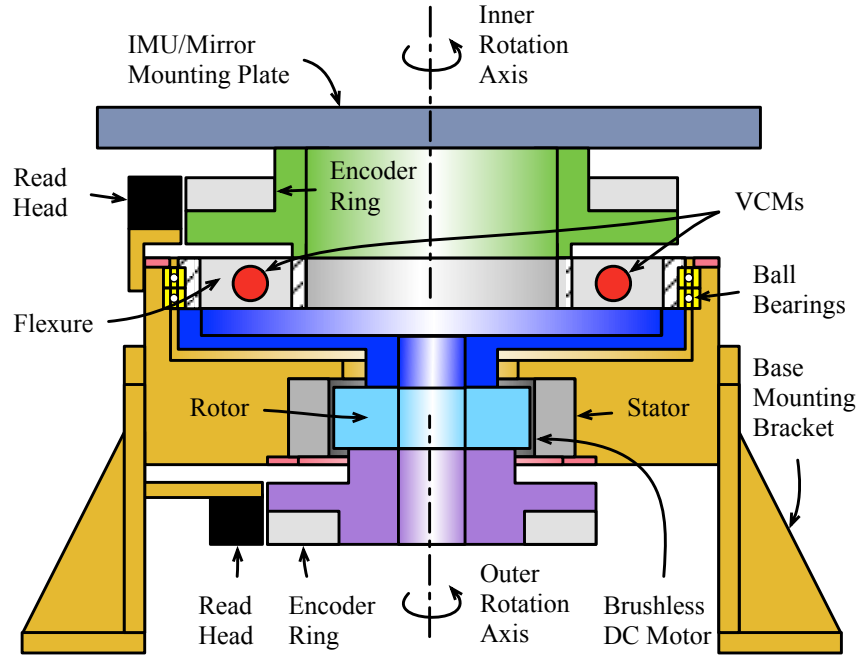

(b) 2-DOF testbed

Figure 2.3: Experimental testbeds: (a) The 1-DOF testbed represents a single-axis gimbal with a conventional ball bearing joint. (b) The 2-DOF testbed represents a single-axis gimbal with the hybrid flexure bearing joint.

deflection of the flexure was measured with a capacitive proximity sensor which proved difficult to calibrate [21]. For this work, a second optical encoder was integrated directly into the inner axis to obviate the need for repeated calibration. The inner axis of the flexure is directly attached to the payload LOS. The angular rate of the LOS is measured by an IMU which can be mounted to the top plate during tests.

Table 2.1: Testbed components

Component	**Manufacturer**	**Model/Part No.**
Ball bearings	Kaydon	SA060FZ6Z
Encoder ring (outer)	Renishaw	REXA30USA100B
Encoder ring (inner)	Renishaw	REXA30USA150B
Encoder readhead (outer)	Renishaw	RA32BAA100B30F
Encoder readhead (inner)	Renishaw	RA32BAA150B30F
Brushless DC motor	Axsys Technologies	BTM-35B
Voice coil motor	H2W Technologies	NCC01-04-001-1X
Embedded microcontroller	Freescale Semiconductor	MPC8270

2.3 Test Configurations

Two primary test configurations are used to study the performance of the hybrid flexure bearing concept. The first test configuration allows for relative motion testing (i.e., using relative encoder feedback only). The second test configuration supports inertial testing (i.e., using IMU feedback to inertially stabilize the LOS) in the presence of base motion disturbances. The two test configurations are described in greater detail below.

2.3.1 Relative test configuration

Figure 2.4 shows the 1-DOF and 2-DOF experimental testbeds in the relative test configuration. In this configuration, each testbed is mounted to a stationary optical table. This configuration simplifies testing because it does not require the use of external optics or optical sensors that must be properly aligned. Relative encoder measurements are the only sensors required for feedback in the control system. An IMU can be optionally mounted to the rotation axis of either testbed, but is not required for feedback. This test configuration is primarly used for system characterization, studying the frictional characteristics of the ball bearing joint, and for running system identification

tests to generate frequency responses for testbed model validation. Additional details about testbed system identification and model validation are given in Chapter 3.

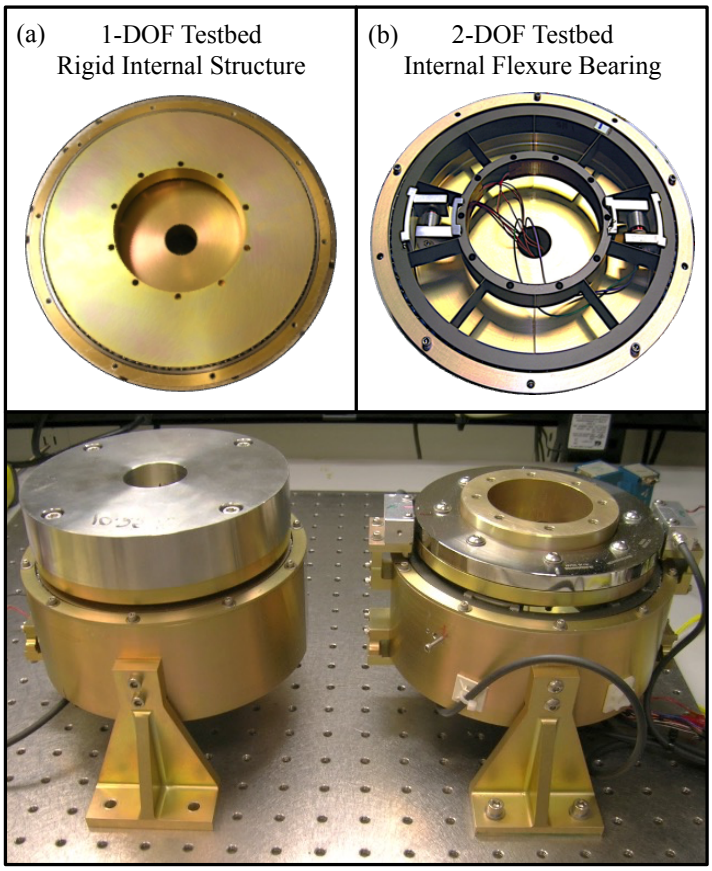

Figure 2.4: Experimental testbeds in the relative test configuration: (a) The 1-DOF testbed has a rigid internal structure in place of the rotational flexure. (b) The 2-DOF testbed incorporates the rotational flexure.

2.3.2 Inertial test configuration

Figure 2.5 depicts the inertial test configuration developed during this research effort. In this configuration, the testbed is mounted directly to a rotary stage which provides the ability to inject base motion disturbances into the testbed. The base motions are intended to mimic the disturbances generated by a moving or vibrating host vehicle. An IMU is mounted to the LOS rotation axis and provides the rate gyro feedback required for inertial stabilization. An autocollimator provides an optical reference that is used to score pointing performance. Table 2.2 lists the components used in the inertial test configuration.

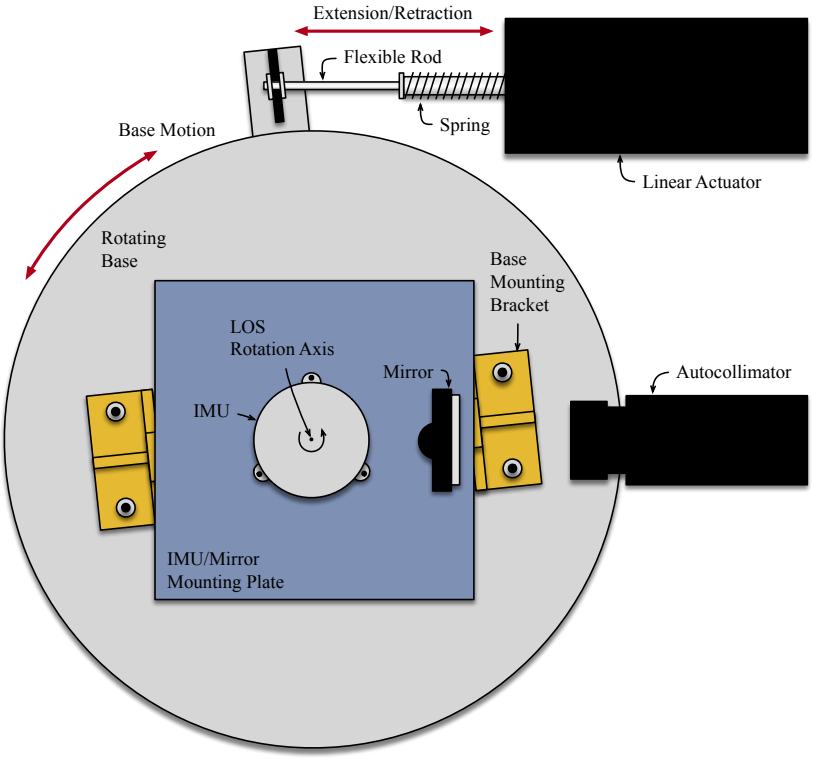

(a) Top view

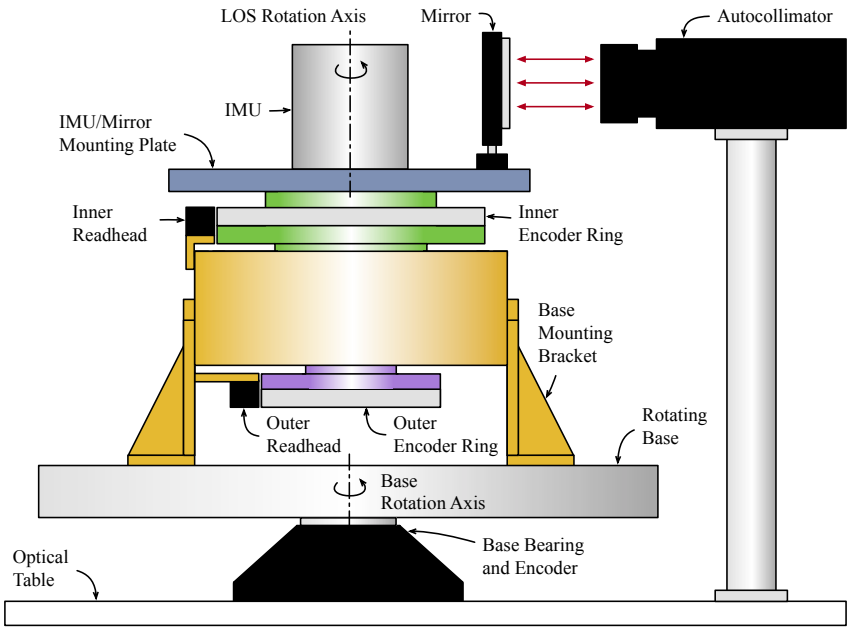

(b) Side view

Figure 2.5: Inertial test configuration diagram

Table 2.2: Inertial testbed components

Component	**Manufacturer**	**Model/Part No.**
Autocollimator	Micro-Radian Instruments	T100
Mirror	Thorlabs	PF20-03-P01
IMU	Systron Donner	SDI505
Encoder ring (base)	RLS	MRA7D049AB025E00
Encoder readhead (base)	RLS	MBA7DDH19BC42C00
Linear actuator	Moticont	LMA-051-089-01
Power amplifier	Crown	XLi 2500
Function generator	B&K Precision	4053B
Power distribution unit	Tripp Lite	PDU15NETLX
Embedded microcontroller	Freescale Semiconductor	MPC8270

The custom-built rotary stage is comprised of a rotating aluminum base suspended by a ball bearing joint. The testbed is carefully mounted to the rotary stage such that the LOS rotation axis is well aligned with the base rotation axis. Any misalignment can generate undesirable payload accelerations that would appear as additional torque disturbances in the control system. The base rotation angle is measured by a magnetic encoder that is embedded within the base fixture. The base encoder provides an angular resolution of 12 µrad.

Base motion disturbances are generated by a linear actuator which is attached to the rotating base with a flexible rod. The flexible rod provides radial compliance so that the mechanical linkage is not overconstrained. The attached linear spring keeps the actuator centered near the middle of its stroke. The base rotates counterclockwise/clockwise as the linear actuator extends/retracts. An audio power amplifier supplies the actuator drive current. A programmable function generator generates the desired disturbance waveform.

A tactical grade IMU is mounted to the LOS rotation axis and provides the rate gyro feedback necessary for inertial stabilization. The gyro is based on quartz tuning fork technology which exhibits 1 deg/hr gyro bias stability and 0.02 deg/$\sqrt{\text{hr}}$ angular random walk [25, 26]. The IMU is sampled at 1200 Hz and provides an angular rate resolution of approximately 30 nrad/s. The gyro can operate over a large dynamic range with angular rates up to ±1000 deg/s.

The autocollimator is mounted to the optical table and provides an inertial reference to score pointing performance. The autocollimator operates by projecting a beam of collimated light at the target mirror which is mounted to the LOS rotation axis. The mirror reflects the beam back into

the instrument where the beam is focused and detected by a photodetector. The autocollimator measures the deviation between the emitted beam and the reflected beam, forming an angular measurement. The autocollimator provides an angular resolution of 0.05 µrad and a maximum calibrated measuring range of ±0.33 deg.

Recall from Fig. 1.5 that pointing performance is evaluated in the inertial reference frame. Although the gyro rate can be integrated to form an inertial angle, the angular position will slowly drift over long time scales as a result of accumulated gyro noise. The autocollimator provides an accurate low frequency angular measurement. This measurement is combined with the integrated gyro rate using complementary filters to form an accurate high-bandwidth measurement of the LOS angle.

Figure 2.6 shows the 2-DOF testbed mounted in the inertial test configuration. Note that several tungsten weights are mounted around the circumference of the rotary stage to increase the total moment of inertia of the base. The weights are added to better approximate the inertia of a larger host vehicle and reduce interactions between the testbed and the base.

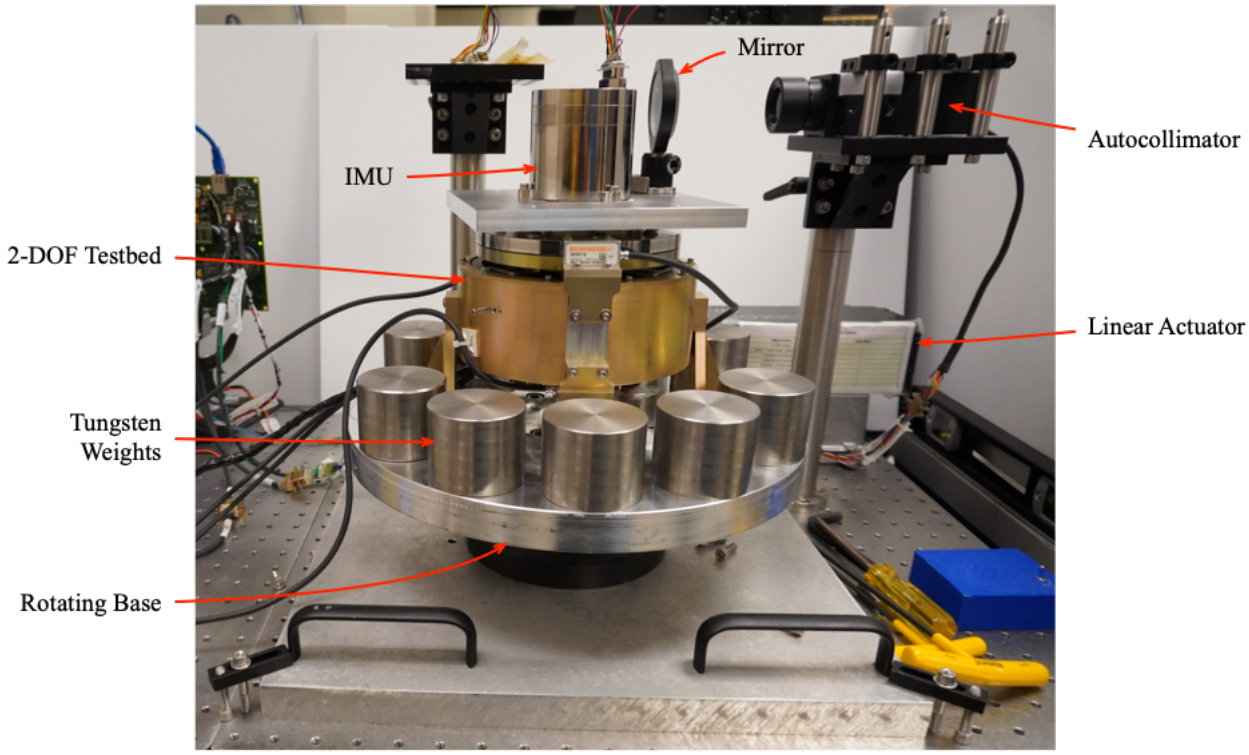

Figure 2.6: 2-DOF testbed in the inertial test configuration

2.4 Control System Implementation

Figure 2.7 depicts the the testbed control system implementation. The experimental testbed is driven by a custom set of control electronics which includes an embedded microcontroller, linear motor amplifiers, and an interface board which provides several channels of general purpose analog and digital I/O. The real-time embedded software runs on a 400 MHz PowerPC-based microprocessor. The optical encoders, magnetic encoder, and IMU are all read via serial peripheral interfaces. The analog output of the autocollimator is digitized by the 16-bit A/D. A variety of other sensor measurements are available for diagnostic purposes, including measured motor voltages, motor currents, and temperatures. VCM and BLDC motor commands are generated by the control algorithms and sent to the motor amplifiers to drive the desired motor currents. The controller algorithms are implemented in the C programming language and execute at a 1200 Hz interrupt rate. Different control algorithms can be developed rapidly through auto-generated C-code using the MATLAB® Coder™ toolset. The embedded code can then be compiled and built into an executable which is automatically loaded by the embedded microcontroller upon boot up.

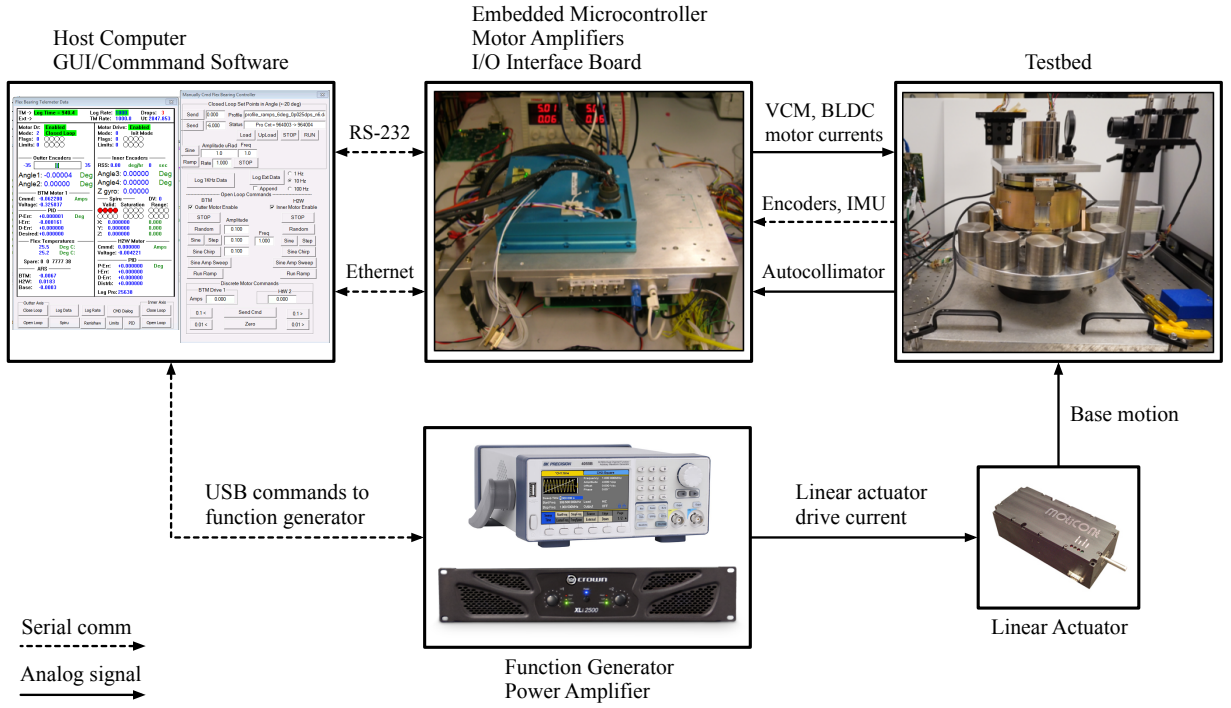

Figure 2.7: Testbed control system implementation

The host computer runs the custom graphical user interface (GUI) and command software. The GUI command software is developed in Visual C. The GUI provides the ability to view testbed status, upload controller parameters, configure different test modes, and log test data. High-rate data is streamed via ethernet from the embedded microcontroller to the host computer. The command software provides automation capabilities for various open-loop and closed-loop tests through custom command profiles and test scripts. The host computer also controls the rotary stage used to inject base disturbances into the testbed. Base motion disturbances are generated by a linear actuator which is attached to the rotating base. An audio power amplifier supplies the actuator drive current. A programmable function generator generates the desired disturbance waveform. The host computer communicates to the function generator through a USB interface. Arbitrary waveforms can be constructed and uploaded to the function generator using the MATLAB® Instrument Control Toolbox™.

Chapter 3

System Modeling

This chapter describes the dynamical model for the hybrid flexure bearing system. A significant challenge associated with the development of precision pointing control systems is the identification and modeling of friction. In particular, dynamic (i.e., presliding) friction is often difficult to accurately model. For systems which undergo small motions with frequent velocity reversals, presliding friction effects dominate the system dynamics and the base motion disturbances and LOS become tightly coupled. An accurate friction model is required for the prediction of performance in simulation, and is crucial in assessing the impact of bearing friction on pointing performance. This chapter presents a data-based dynamic friction model that significantly improves friction model accuracy in both the time and frequency domains. Key friction model features are identified to better match frictional behavior observed in experiments. Simulation results are validated with measured friction data collected from the experimental testbed.

3.1 Linear Plant Model

3.1.1 1-DOF testbed model

The rigid body model for the 1-DOF testbed is depicted in Fig. 3.1. The 1-DOF testbed configuration is the simplest to model as it represents a single gimbal axis comprised of only a motor, ball bearing, and payload moment of inertia. The structure is assumed to be sufficiently rigid so that any flexible modes in the system can be neglected. The equation of motion (EOM) for the 1-DOF testbed configuration is expressed as

$$J\ddot{\theta} = T_m - T_f(\phi, \dot{\phi}) \tag{3.1}$$

where J is the moment of inertia about the rotation axis, θ is the inertial LOS angle, T_m is the applied motor torque, and T_f is the bearing friction torque. The friction torque, $T_f = T_f(\phi, \dot{\phi})$, is expressed as a general nonlinear function of the relative motion between the LOS and the base, where $\phi = \theta - \theta_b$ and $\dot{\phi} = \dot{\theta} - \dot{\theta}_b$. In general, this nonlinear function may also depend implicitly on other internal friction states to capture frictional behaviors such as hysteresis or non-local memory.

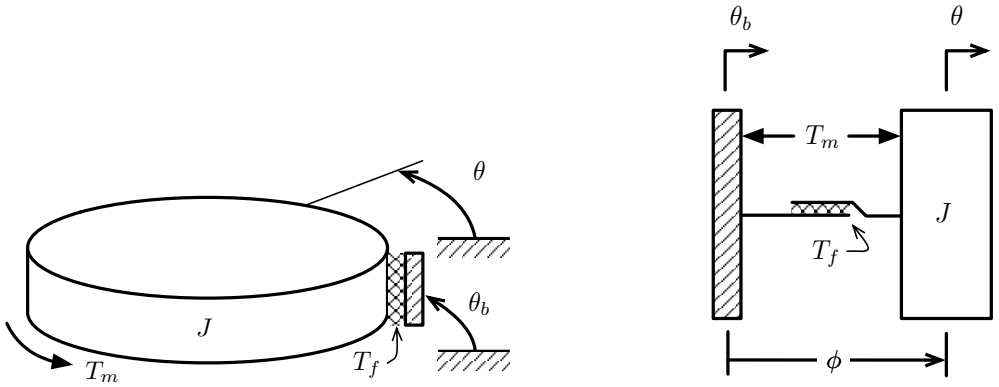

Figure 3.1: 1-DOF testbed model: (a) rotational representation and (b) translational representation

Modeling friction is one of the most challenging aspects in pointing system development [6, 10]. In particular, dynamic presliding friction is often difficult to characterize and model accurately. For systems which undergo small motions with frequent velocity reversals, presliding friction effects dominate the system dynamics and the base motion disturbances and LOS become tightly coupled [11]. An accurate friction model is required for the prediction of performance in simulation, and is crucial in assessing the impact of bearing friction on pointing performance. Section 3.2 discusses dynamic friction models in greater detail and also presents a new data-based approach to friction modeling.

To simplify analysis, a linear model is obtained under the assumption that presliding friction can be approximated by an effective linear stiffness, k_f, and viscous damping term, b_f, as depicted in Fig. 3.2. This approximation is valid under certain steady-state operating conditions (i.e, small amplitude motion about a nominal position). Under these conditions, the friction torque can be

expressed as a linear function of the relative motion between the base and the LOS

$$\begin{aligned} T_f &= T_f(\phi, \dot{\phi}) \\ &= k_f\phi + b_f\dot{\phi} \\ &= k_f(\theta - \theta_b) + b_f(\dot{\theta} - \dot{\theta}_b) \end{aligned} \tag{3.2}$$

where k_f is the effective frictional stiffness and b_f is the viscous damping coefficient. The linearized friction parameter values, k_f and b_f, depend on the particular operating condition or amplitude of motion and can be determined through system identification tests as described in Section 3.3.2. Note that the linearized friction model simplifies to typical viscous damping if the frictional stiffness term is neglected (i.e., $k_f = 0$).

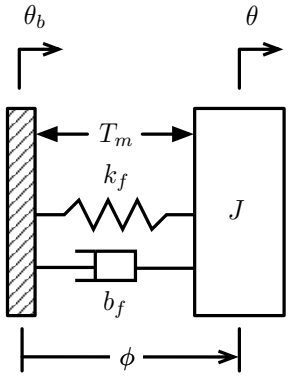

Figure 3.2: 1-DOF testbed model with linearized friction

Combining Eqs. (3.1) and (3.2), the linearized EOM becomes

$$J\ddot{\theta} + b_f\dot{\theta} + k_f\theta = T_m + b_f\dot{\theta}_b + k_f\theta_b \tag{3.3}$$

Taking the Laplace transform of Eq. (3.3), the LOS angular response can be expressed as

$$\theta(s) = \frac{1}{Js^2 + b_f s + k_f} T_m(s) + \frac{b_f s + k_f}{Js^2 + b_f s + k_f}\theta_b(s) \tag{3.4}$$

It is clear from Eq. (3.4) that base motion disturbances are dynamically coupled into LOS motion through the bearing friction. The severity of this coupling depends upon the effective frictional stiffness and damping values for a given operating condition. The derivation of linear state space

models for the 1-DOF testbed can be found in Appendix B.

3.1.2 2-DOF testbed model

The 2-DOF testbed is modeled by the lumped two-mass system shown in Fig. 3.3. The rotational flexure is represented by the spring constant, k, and damping coefficient, b. The BLDC motor applies torque, T_1, to the outer axis across the ball bearing joint. The VCMs apply torque, T_2, between the inner and outer rings of the rotational flexure. The nonlinear ball bearing friction torque, T_f, transmits base motion disturbances, θ_b, through the ball bearing joint.

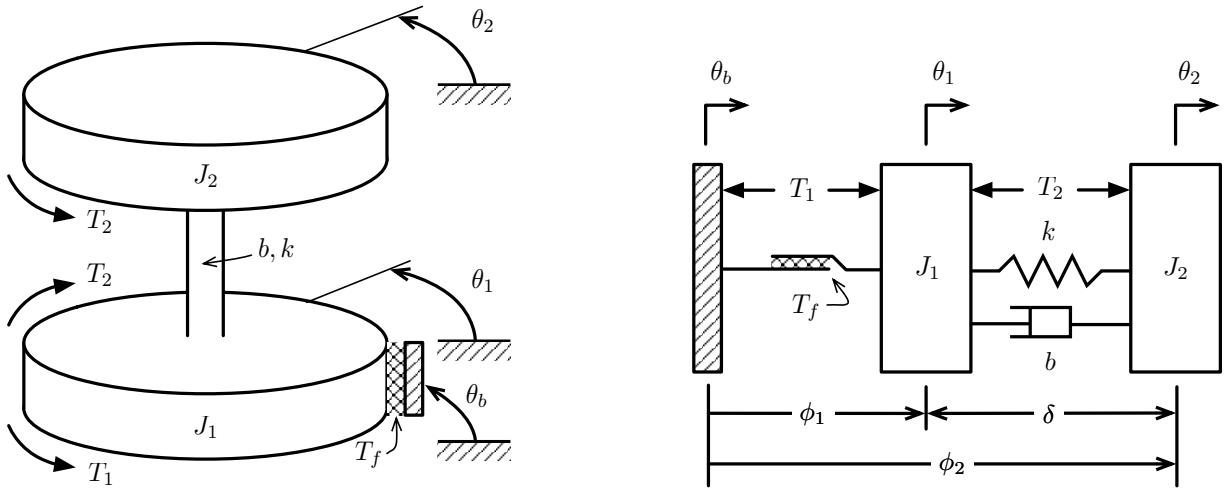

Figure 3.3: 2-DOF testbed model: (a) rotational representation and (b) translational representation

The following relative angles are defined in terms of the available measurements

$$\phi_1 = \theta_1 - \theta_b \tag{3.5}$$

$$\phi_2 = \theta_2 - \theta_b \tag{3.6}$$

$$\delta = \theta_2 - \theta_1 = \phi_2 - \phi_1 \tag{3.7}$$

where ϕ_1 and ϕ_2 are the angles measured by the optical encoders relative to the base, and δ is the relative deflection of the flexure, which is calculated from the difference between the encoder measurements. In the inertial test configuration, the inertial LOS angle, θ_2, is measured by the autocollimator. The inertial LOS angular rate, $\dot{\theta}_2$, is measured by the IMU.

The 2-DOF testbed model EOMs are derived by summing the moments about the outer and inner rotation axes, respectively. The EOMs can be expressed as a system of second-order ordinary differential equations (ODEs)

$$J_1\ddot{\theta}_1 - b(\dot{\theta}_2 - \dot{\theta}_1) - k(\theta_2 - \theta_1) = T_1 - T_2 - T_f(\phi_1, \dot{\phi}_1) \tag{3.8}$$

$$J_2\ddot{\theta}_2 + b(\dot{\theta}_2 - \dot{\theta}_1) + k(\theta_2 - \theta_1) = T_2 \tag{3.9}$$

where J_1 and J_2 are the moments of inertia of the outer and inner axes, k and b are the flexure stiffness and damping coefficient, T_1 and T_2 are the applied motor torques, and T_f is the ball bearing friction torque. The ball bearing friction torque, $T_f = T_f(\phi_1, \dot{\phi}_1)$, is expressed as a general nonlinear function of the relative motion between the outer axis and the base, where $\phi_1 = \theta_1 - \theta_b$ and $\dot{\phi}_1 = \dot{\theta}_1 - \dot{\theta}_b$.

To simplify analysis, a linear model is obtained under the assumption that presliding friction can be approximated by an effective linear stiffness, k_f, and viscous damping term, b_f, as depicted in Fig. 3.4. This approximation is valid under certain steady-state operating conditions (i.e, small amplitude motion about a nominal position). Under these conditions, the friction torque can be expressed as a linear function of the relative motion between the base and the outer axis

$$\begin{aligned} T_f &= T_f(\phi_1, \dot{\phi}_1) \\ &= k_f\phi_1 + b_f\dot{\phi}_1 \\ &= k_f(\theta_1 - \theta_b) + b_f(\dot{\theta}_1 - \dot{\theta}_b) \end{aligned} \tag{3.10}$$

where k_f is the effective frictional stiffness and b_f is the viscous damping coefficient. The linearized friction parameter values, k_f and b_f, depend on the particular operating condition or amplitude of motion and can be determined through system identification tests as described in Section 3.3.2.

Combining Eqs. (3.8), (3.9), and (3.10), the linearized EOMs become

$$J_1\ddot{\theta}_1 + (b + b_f)\dot{\theta}_1 + (k + k_f)\theta_1 - b\dot{\theta}_2 - k\theta_2 = T_1 - T_2 + b_f\dot{\theta}_b + k_f\theta_b \tag{3.11}$$

$$J_2\ddot{\theta}_2 + b\dot{\theta}_2 + k\theta_2 - b\dot{\theta}_1 - k\theta_1 = T_2 \tag{3.12}$$

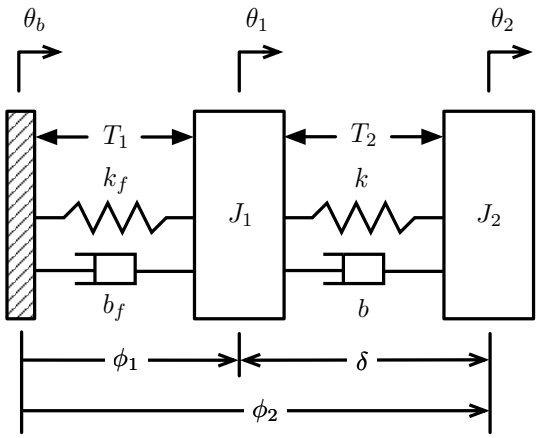

Figure 3.4: 2-DOF testbed model with linearized friction

The Laplace transform of Eqs. (3.11) and (3.12) can be written as

$$\left[J_1 s^2 + (b + b_f)s + (k + k_f)\right] \theta_1(s) - \left[bs + k\right] \theta_2(s) = T_1(s) - T_2(s) + \left[b_f s + k_f\right] \theta_b(s) \tag{3.13}$$

$$\left[J_2 s^2 + bs + k\right] \theta_2(s) - \left[bs + k\right] \theta_1(s) = T_2(s) \tag{3.14}$$

and expressed in matrix form

$$\begin{bmatrix} J_1 s^2 + b_{\text{eff}} s + k_{\text{eff}} & -(bs + k) \\ -(bs + k) & J_2 s^2 + bs + k \end{bmatrix} \begin{bmatrix} \theta_1(s) \\ \theta_2(s) \end{bmatrix} = \begin{bmatrix} T_1(s) - T_2(s) + (b_f s + k_f)\theta_b(s) \\ T_2(s) \end{bmatrix} \tag{3.15}$$

where $k_{\text{eff}} = k + k_f$ and $b_{\text{eff}} = b + b_f$ are the effective stiffness and damping coefficient, respectively. Equation (3.15) can then be solved to obtain an expression for the inertial angles

$$\begin{bmatrix} \theta_1(s) \\ \theta_2(s) \end{bmatrix} = \begin{bmatrix} J_1 s^2 + b_{\text{eff}} s + k_{\text{eff}} & -(bs + k) \\ -(bs + k) & J_2 s^2 + bs + k \end{bmatrix}^{-1} \begin{bmatrix} T_1(s) - T_2(s) + (b_f s + k_f)\theta_b(s) \\ T_2(s) \end{bmatrix} \tag{3.16}$$

Finally, expanding Eq. (3.16) in terms of the applied motor torques and base motion disturbances, the angular responses can be expressed as

$$\theta_1(s) = \frac{\frac{1}{J_1}\left(s^2 + \frac{b}{J_2}s + \frac{k}{J_2}\right)}{s^2\left(s^2 + \frac{b}{J_{\text{eff}}}s + \frac{k}{J_{\text{eff}}}\right) + \left(\frac{b_f}{J_1}s + \frac{k_f}{J_1}\right)\left(s^2 + \frac{b}{J_2}s + \frac{k}{J_2}\right)} T_1(s)$$
$$- \frac{\frac{1}{J_1}s^2}{s^2\left(s^2 + \frac{b}{J_{\text{eff}}}s + \frac{k}{J_{\text{eff}}}\right) + \left(\frac{b_f}{J_1}s + \frac{k_f}{J_1}\right)\left(s^2 + \frac{b}{J_2}s + \frac{k}{J_2}\right)} T_2(s)$$
$$+ \frac{\left(\frac{b_f}{J_1}s + \frac{k_f}{J_1}\right)\left(s^2 + \frac{b}{J_2}s + \frac{k}{J_2}\right)}{s^2\left(s^2 + \frac{b}{J_{\text{eff}}}s + \frac{k}{J_{\text{eff}}}\right) + \left(\frac{b_f}{J_1}s + \frac{k_f}{J_1}\right)\left(s^2 + \frac{b}{J_2}s + \frac{k}{J_2}\right)} \theta_b(s) \quad (3.17)$$

$$\theta_2(s) = \frac{\frac{1}{J_1}\left(\frac{b}{J_2}s + \frac{k}{J_2}\right)}{s^2\left(s^2 + \frac{b}{J_{\text{eff}}}s + \frac{k}{J_{\text{eff}}}\right) + \left(\frac{b_f}{J_1}s + \frac{k_f}{J_1}\right)\left(s^2 + \frac{b}{J_2}s + \frac{k}{J_2}\right)} T_1(s)$$
$$+ \frac{\frac{1}{J_2}\left(s^2 + \frac{b_f}{J_1}s + \frac{k_f}{J_1}\right)}{s^2\left(s^2 + \frac{b}{J_{\text{eff}}}s + \frac{k}{J_{\text{eff}}}\right) + \left(\frac{b_f}{J_1}s + \frac{k_f}{J_1}\right)\left(s^2 + \frac{b}{J_2}s + \frac{k}{J_2}\right)} T_2(s)$$
$$+ \frac{\left(\frac{b_f}{J_1}s + \frac{k_f}{J_1}\right)\left(\frac{b}{J_2}s + \frac{k}{J_2}\right)}{s^2\left(s^2 + \frac{b}{J_{\text{eff}}}s + \frac{k}{J_{\text{eff}}}\right) + \left(\frac{b_f}{J_1}s + \frac{k_f}{J_1}\right)\left(s^2 + \frac{b}{J_2}s + \frac{k}{J_2}\right)} \theta_b(s) \quad (3.18)$$

where $J_{\text{eff}} = \frac{J_1 J_2}{J_1 + J_2}$ is the effective inertia. It is clear from Eq. (3.18) that base motion disturbances are dynamically coupled to the LOS through the bearing friction. The severity of this coupling depends upon the effective frictional stiffness and damping values for a given operating condition. The corresponding linear state space models for the 2-DOF testbed are derived in Appendix B.

Although the linear models derived in this section are useful for understanding overall testbed dynamics and they capture gross frictional behavior under certain steady-state conditions, they have limited utility for assessing general pointing system performance in the presence of nonlinear bearing friction. Section 3.2 introduces a nonlinear friction model that captures important dynamic presliding friction phenomena observed in experiments and can be used in nonlinear simulation to assess pointing performance.

3.2 Friction Model

Friction is a complex nonlinear phenomenon which adversely affects the performance of many precision motion control systems. A significant challenge associated with the development of precision pointing systems is the identification and modeling of friction. An accurate friction model is often required for the prediction of performance in simulation, and may also be used for model-based friction compensation techniques in control [27–30]. In particular, dynamic (presliding) friction is often difficult to accurately model in both the time domain and frequency domain simultaneously [11,31,32]. This section presents a data-based extension to an existing friction model, known as the Dahl dynamic hysteresis model [33,34], which incorporates an empirical friction slope function to provide a more accurate representation of arbitrarily shaped hysteresis curves [35]. This data-based approach avoids the added complexity of identifying or fitting model parameters, and can be implemented with a simple look up table. Simulation results are validated with measured friction data collected from the experimental testbed. We show that the data-based approach significantly improves the friction model accuracy in both the time and frequency domains.

3.2.1 Static friction models

For systems which undergo relatively large amplitude or high-speed motions, a simple static friction model may be sufficient. Static friction models, also commonly known as the classical friction laws, describe the force-velocity characteristics depicted in Fig. 3.5. In the most basic form, static friction is modeled as a function of steady-state velocity

$$F(v) = \underbrace{F_c \operatorname{sgn}(v)}_{\text{Coulomb}} + \underbrace{\sigma_v v}_{\text{Viscous}} + \underbrace{F_s(v)}_{\text{Stribeck}} \tag{3.19}$$

where the Coulomb term is a function of the sign of the velocity, the viscous term is proportional to velocity, and the Stribeck term is a function which describes the velocity-weakening/strengthening characteristic due to lubrication effects at the contact interface. Many other variations on the classical models are widely discussed in the literature [28–30, 36–38]. The classical models work well for describing systems which undergo relatively large steady-state motions.

Although the implementation of static friction models in simulation is simple and straightfor-

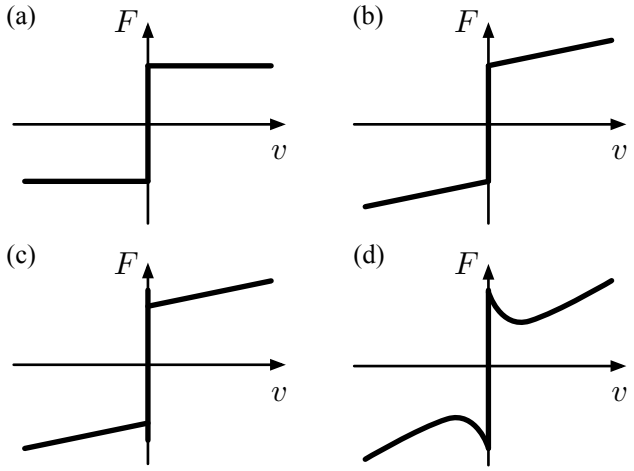

Figure 3.5: Classical friction models: (a) Coulomb friction, (b) Coulomb and viscous friction, (c) Coulomb and viscous friction with stiction, (d) Stribeck effect

ward, problems arise from discontinuities in the model. The use of discontinuous functions often leads to numerical problems in simulation, especially when the velocity is near zero or when the velocity has frequent zero crossings. This can cause unrealistic behaviors such as limit cycling, hunting, or chattering. Ad hoc methods, such as the Karnopp model [39], have been developed to help address these numerical issues. However, these ad hoc workarounds do not address the fundamental shortcoming of static friction models. In reality, friction is not a discontinuous function of time or system state. Moreover, static friction models do not capture important friction phenomena such as position dependence and hysteresis. [27, 30]. For precision pointing systems which undergo small motions with frequent velocity reversals, presliding friction effects dominate and can significantly alter the dynamics of the system [11]. This dynamic friction behavior is described in greater detail in the following section.

3.2.2 Dynamic friction models

Dynamic friction describes the behavior of friction before gross sliding occurs (i.e., presliding) and has been studied extensively in the literature. It is based on the elastic and plastic deformation of asperities at the contact interface, which can be viewed as a series of nonlinear springs or bristles that resist motion, as depicted in Fig. 3.6. The underlying material behavior at the contact interface leads to a somewhat surprising result: dynamic presliding friction can both dissipate

and store energy, thereby creating additional dynamics in the system. The overall effect is that dynamic friction behaves like a nonlinear hysteretic spring which gives rise to so-called "friction microdynamics" within the system [40, 41]. This frictional stiffness has a significant impact on the ability of the control system to accurately point and move the gimbal. Adequately modeling the transition in friction torque that takes place during a velocity reversal is crucial in assessing the impact of bearing friction on pointing performance.[1]

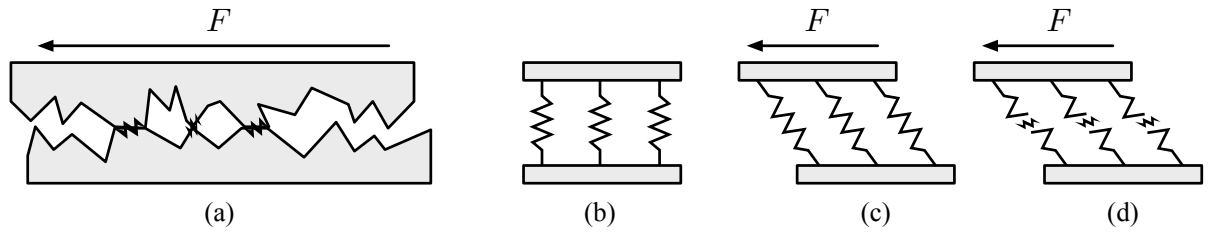

Figure 3.6: Dynamic friction: (a) Contact asperities, (b) springs or bristles represent lumped elastic asperity deformation, (c) force causes springs to deflect, (d) displacement causes springs to break away, transition to true sliding

There are numerous dynamic friction models available with varying degrees of fidelity and complexity. Examples include the Dahl model [45], the LuGre model [46], the elastoplastic model [47], the Leuven model [48], and the generalized Maxwell-slip (GMS) model [49]. An excellent comparison of the various properties for each of the friction models is given in [50]. A significant challenge associated with the modeling of dynamic friction is that it is often difficult to obtain a single model that achieves accurate performance in both the time domain and frequency domain simultaneously [11, 31, 32]. We present a data-based approach which better characterizes the frictional behavior observed in experiments. The approach is based on the Dahl friction model [33, 45], which is well-suited for simulation and real-time implementation. We show that this data-based approach significantly improves the friction model accuracy in both the time and frequency domains. Sections 3.2.3 and 3.2.4 discuss the dynamic friction models used as the basis for the data-based approach.

[1] Although ball bearings greatly reduce friction compared to the simple sliding joint depicted in Fig. 3.6, dynamic friction still plays an important role in ball bearing rolling friction. It is important to note that ball bearings do not exhibit pure rolling contact. Under preload, bearing components deform to create elliptical contact regions between the balls and races. Differential slip occurs within these contact regions [42–44]. Thus, the same concepts depicted in Fig. 3.6 apply to ball bearing joints.

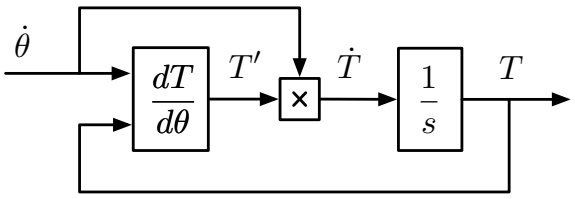

Figure 3.7: Dahl model block diagram

3.2.3 Dahl solid friction model

The Dahl friction model, originally coined as the solid friction model (SFM), was initially developed to describe the hysteretic behavior observed in ball bearing friction [45, 51]. In this work, we use the author's original naming convention to distinguish it from a modification of the model which is described in the following section. According to the Dahl SFM, the time rate of change of the friction torque can be expressed as

$$\frac{dT}{dt} = \frac{dT}{d\theta}\frac{d\theta}{dt} = \frac{dT}{d\theta}\dot{\theta} \tag{3.20}$$

where the friction torque, T, is assumed to be a function of angular displacement, θ. Integrating Eq. (3.20) with respect to time gives an expression for the friction torque

$$T = \int_0^t \frac{dT}{d\theta}\dot{\theta}\ d\tau \tag{3.21}$$

which can be implemented in simulation as depicted in Fig. 3.7.

The derivative of the friction torque with respect to angular displacement, $\frac{dT}{d\theta}$, is referred to as the *friction slope function*. The friction slope function characterizes the slope of the hysteresis curve at any given point. Based on empirical data, it was found that the friction slope function can be expressed in the general form [51]

$$\frac{dT}{d\theta} = \sigma\left(1 - \frac{T}{T_c}\operatorname{sgn}\dot{\theta}\right)^{\alpha} \tag{3.22}$$

where $\sigma > 0$ is the rest stiffness (i.e., stiffness when $T = 0$), $T_c > 0$ is the Coulomb (or running) torque, and $\alpha > 0$ is the shape factor which dictates the overall shape of the hysteresis curve as

depicted in Fig. 3.8. The three model parameters (σ, T_c, α) are typically selected to best fit the measured force-deflection curve for a given system.

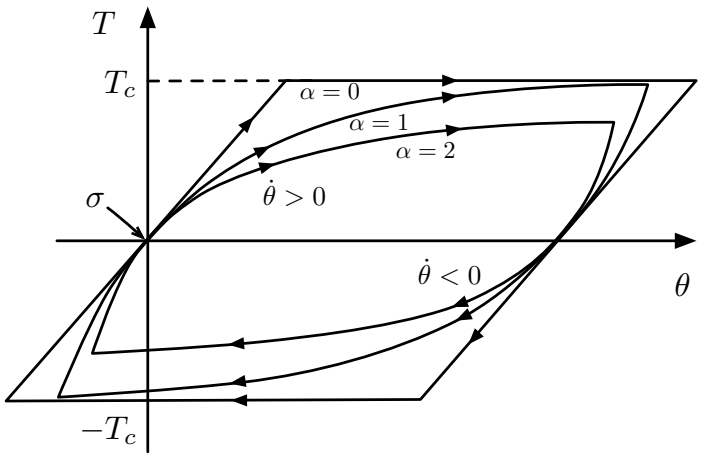

Figure 3.8: Dahl model hysteresis shapes

The friction slope function is always positive, regardless of the velocity direction. The slope immediately following a velocity reversal, known as the *turnaround stiffness*, can be expressed as

$$\left.\frac{dT}{d\theta}\right|_{\theta=\theta_r} = \sigma\left(1 - \frac{T(\theta_r)}{T_c}\operatorname{sgn}\dot{\theta}\right)^{\alpha} \tag{3.23}$$

where θ_r is the reversal point displacement and $T(\theta_r)$ is the friction torque value at turnaround. It is clear from Eq. (3.23) that the turnaround stiffness varies depending on the friction value at the turnaround point. Thus, for general non-symmetric motion, the SFM exhibits variable turnaround stiffness. This particular model behavior is not exhibited in experimental observations of friction [30,40,52]. Another shortcoming of the SFM is that it cannot enforce minor loop closure. Minor loop closure is defined where the minor hysteresis curve ends (i.e., closes) at the same point where it started, and then follows the original hysteresis curve as if it had never happened. Minor loop closure is accomplished through a hysteresis feature known as nonlocal memory. Nonlocal memory is a qualitative property of hysteresis for which the friction depends on both current and previous extremum values [53,54]. Figure 3.9(a) depicts the two primary shortcomings of the SFM. Both of these issues are addressed through the model modifications described in the following section.

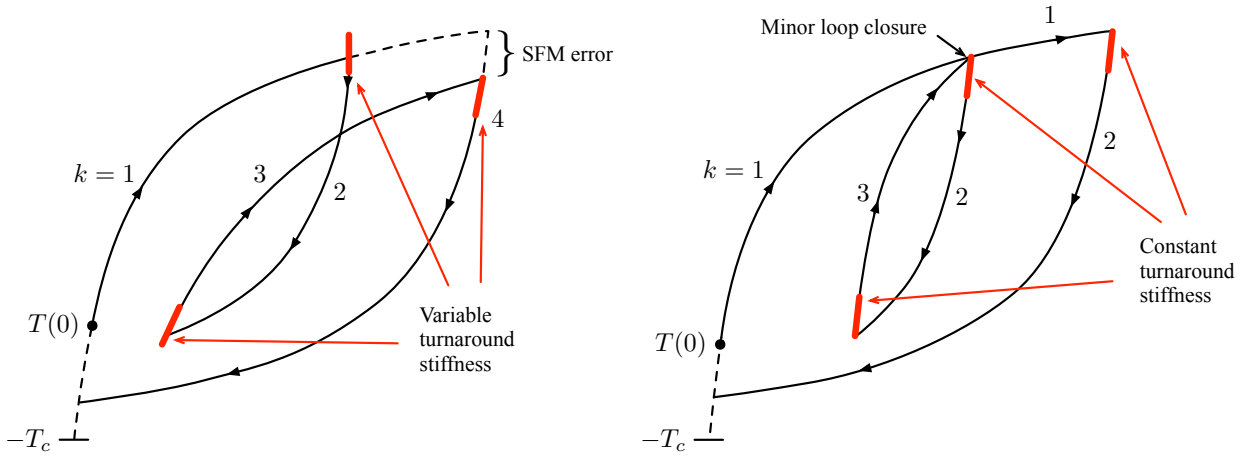

(a) SFM (b) DHM

Figure 3.9: Comparison of SFM and DHM hysteresis curves: (a) SFM behavior, (b) DHM behavior

3.2.4 Dahl dynamic hysteresis model

Although the SFM is widely recognized in the literature, a closely related and improved model called the dynamic hysteresis model (DHM) [33, 34] has not received the same widespread attention. The DHM is an extension of the SFM and corrects several shortcomings of the original model. These shortcomings were first identified in [52] when the SFM was compared to experimental observations of friction in a control moment gyro (CMG) gimbal. The authors found that the SFM poorly matched the behavior of systems with non-symmetric or off-axis minor hysteresis loops and concluded that the model could be improved with the inclusion of Prandtl's laws of hysteresis in materials. Prandtl's laws are stated as follows [52]:

1. Immediately after reversal of the sense of deformation, the slope of the stress-strain diagram has the same value as the beginning of the first loading.

2. The shape of any branch of the stress-strain diagram is uniquely determined by the position of the point where the last reversal of the sense of deformation occurred.

3. If the sense of deformation is not reversed again, any such branch will pass through the point where the last but one reversal of the sense of deformation occurred; thereafter, the stress-strain diagram continues as if the loop had never been formed.

Prandtl's laws provide the basis for the modifications in the DHM. With the inclusion of these

additional laws, the DHM corrects for two primary behaviors not exhibited by the original model. Namely, it ensures that the hysteresis curve exhibits the same slope immediately after every velocity reversal (i.e., constant turnaround stiffness) and also enforces minor loop closure (i.e., nonlocal memory [54]). Figure 3.9(b) depicts the improvements made by the DHM.

To capture the behaviors stated in Laws #1 and #2, the original friction slope function given in Eq. (3.22) is redefined as

$$\frac{dT}{d\theta} = \sigma \left(2 - \frac{T - T(k)}{T_c} \operatorname{sgn} \dot{\theta} \right)^{\alpha} \tag{3.24}$$

where $T(k)$ is the value of the friction torque at the last turnaround point, and k is an index which keeps track of the current branch of the hysteresis curve. Similar to the Leuven model [48], the DHM requires a memory stack to keep track of previous turnaround friction values. At each velocity reversal, k is incremented by 1 and the friction value is stored so that $T(k) = T$. Thus, the slope after each velocity reversal (i.e., turnaround stiffness) is given by

$$\left. \frac{dT}{d\theta} \right|_{\theta=\theta_r} = 2^{\alpha} \sigma \tag{3.25}$$

which is independent of the friction value, thereby satisfying Law #1. Additional logic is required to properly handle minor loop closure as specified by Law #3. As each minor loop is closed, the value of k is decremented by 2 so that all previously closed loops are forgotten. The logic flow of the DHM is depicted in Fig. 3.10.

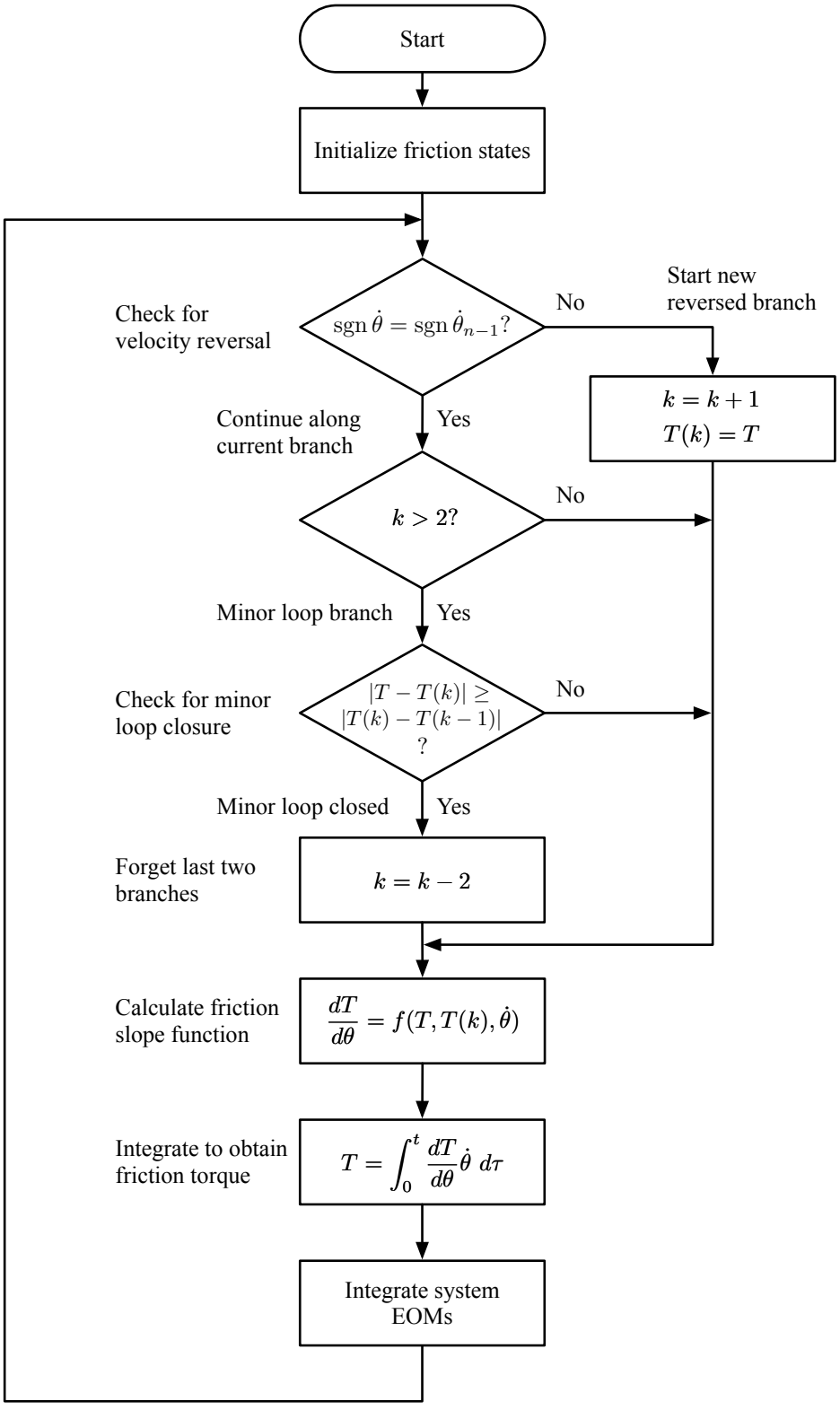

Figure 3.10: Dynamic hysteresis model flow chart

3.2.5 A data-based dynamic friction model

The shapes of the SFM and DHM hysteresis curves are dictated by the analytical friction slope functions defined in Eqs. (3.22) and (3.24). These analytical friction slope functions generate a family of curves with different shapes dictated by α, as depicted in Fig. 3.11. The shape factor, α, is related to the ductility of the materials involved at the friction interface [51]. For a variety of ball bearings tested in [55], measured α values were typically found to lie in the range between 1 and 2. In the literature, a shape factor value of $\alpha = 1$ is most commonly assumed [30].[2]

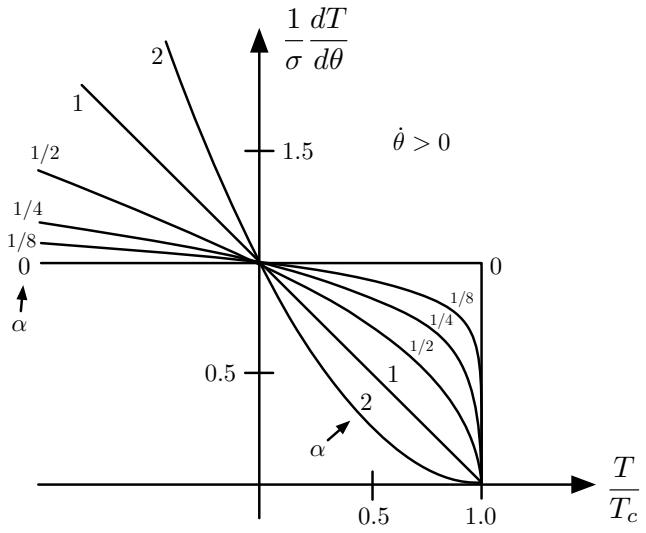

Figure 3.11: Analytical friction slope functions for $\dot{\theta} > 0$ and varying α

Although the shape factor, α, provides the ability to modify the characteristic shape of the hysteresis curve to an extent, it can still be quite difficult to accurately match experimental hysteresis curves, particularly for systems that exhibit two distinct slopes (e.g., a very steep initial slope followed by a shallower slope). This type of characteristic shape was observed in [30, 40, 52] and is also evident in the experimental hysteresis curves obtained during this research effort. Typically, the Dahl model parameters (σ, T_c, α) are chosen to best fit the measured hysteresis curves using a nonlinear least-squares fit, as shown in Fig. 3.12. Although the best-fit model approximates the overall hysteresis shape for large amplitude motions reasonably well, it provides an extremely poor fit for small amplitude motions. Also, the best-fit model significantly underestimates the

[2]This is also the underlying assumption in the derivation of the LuGre model [46].

turnaround stiffness in all cases. Ultimately, the poor fit is due to a lack of adjustable model parameters required to fit arbitrarily shaped hysteresis curves.

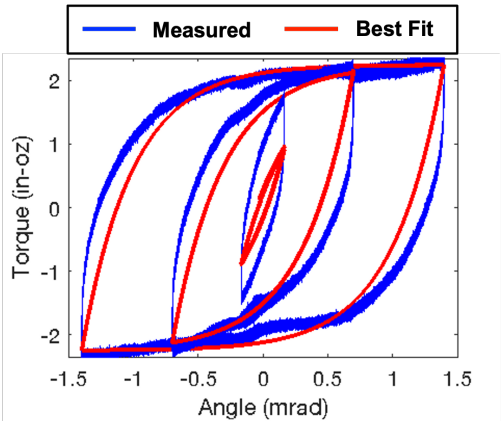

Figure 3.12: Hysteresis curve fitting

There are other approaches available to better approximate arbitrarily shaped hysteresis curves. One approach for achieving better model accuracy is through the use of two or more parallel Dahl models [51,52], as depicted in Fig. 3.13(a). However, the use of n-parallel Dahl models requires the identification of an additional $3n$ model parameters which is not intuitive. Other approaches, such as the Leuven [56] and GMS [49] friction models, use the Maxwell-slip model to approximate the hysteresis function. The Maxwell-slip approach, depicted in Fig. 3.13(b), approximates the hysteresis function through a series of elasto-slide elements. Although the Maxwell-slip implementation avoids potential stack overflow problems, higher accuracy requires a larger number of elasto-slide elements at the cost of additional computational complexity [56]. Moreover, the identification and selection of Maxwell-slip model parameters is nontrivial [57].

As an alternative, we propose a simple modification to the Dahl SFM and DHM. The basic principle behind this approach is to recast the curve fitting problem in terms of the friction slope function instead of the torque-displacement hysteresis curves. This is accomplished by replacing the analytical slope functions defined in Eqs. (3.22) and (3.24) with an empirical slope function, which can be expressed as

$$\frac{dT}{d\theta} = f(x,\dot{\theta}) = \begin{cases} f_+(x) & \text{if } \dot{\theta} \geq 0 \\ f_-(x) & \text{if } \dot{\theta} < 0 \end{cases} \tag{3.26}$$

where f_+ and f_- represent the look up tables (LUTs) for positive and negative velocities, respec-

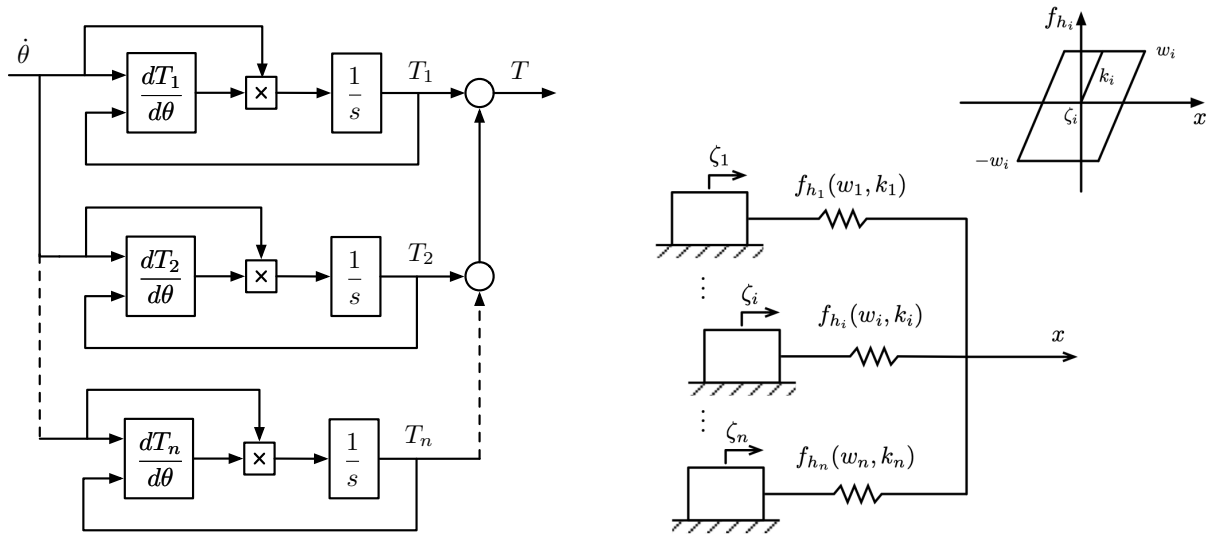

(a) Parallel Dahl models

(b) Maxwell-slip model

Figure 3.13: Approaches for the approximation of hysteresis shapes

tively. Two separate LUTs are required because of the slope function's dependence on the sign of the velocity. For the SFM, the input is the current friction torque value, $x = T$. For the DHM, the input is the difference between the current friction torque and friction torque at the last turnaround point, $x = T - T(k)$. The LUT breakpoints can be arbitrarily assigned to best fit experimental data.

The measured friction slope curves for the experimental testbed are shown in Fig. 3.14. The LUT breakpoints were selected to approximate the slope function for positive velocities only. Since the measured slope function is symmetric for both positive and negative velocities, only one set of breakpoints is required. The breakpoints for the negative direction are obtained by mirroring the positive velocity breakpoints about the vertical axis. In simulation, the LUT output values are calculated by linearly interpolating between each breakpoint.

One of the primary advantages of the data-based approach is that the hysteresis shapes are no longer constrained to the analytical form of Eqs. (3.22) and (3.24). As a result, the approach does not require the selection of model parameters (σ, T_c, α) to best fit the data. Also, since the overall hysteresis shape is built into a single LUT, the approach is much simpler to implement than the Maxwell-slip or parallel Dahl models. The data-based modifications of the two Dahl friction models are referred to as the data-based SFM (DB-SFM) and data-based DHM (DB-DHM).

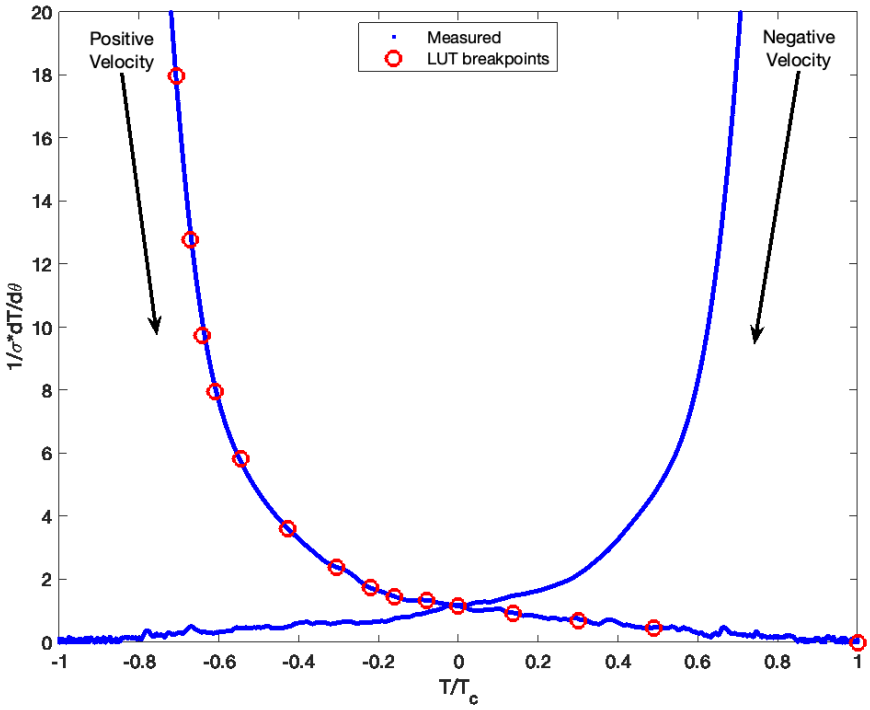

Figure 3.14: Measured friction slope function. LUT breakpoints (circles) are shown for $\dot{\theta} > 0$.

3.3 Friction Model Validation

A valid friction model should accurately represent frictional behavior in both the time and frequency domains. The four different friction models discussed in Section 3.2 (SFM, DHM, DB-SFM, DB-DHM) are compared by evaluating their performance in both the time and frequency domains. Simulation results are compared with measurements collected on the experimental testbed. The friction models are implemented in Simulink and can be found in Appendix C. The model parameters used for simulation of the SFM and DHM are listed in Table 3.1. Figure 3.14 shows the friction slope function LUT used for simulation of the DB-SFM and DB-DHM models.

Table 3.1: Friction model parameters

Parameter	**Symbol**	**Value**	**Units**
Rest stiffness	σ	5.73	in-oz/mrad
Coulomb (running) torque	T_c	2.25	in-oz
Shape factor	α	1	–

3.3.1 Time-domain validation

The experimental hysteresis curves for several different friction tests are shown in Fig. 3.15. The data was collected on the experimental testbed using various amplitude triangular wave motion profiles to achieve a constant velocity of 0.001 deg/s in each direction. The friction torque is estimated from the commanded motor torque and the angle is measured by the optical encoder. As shown in the top plot of Fig. 3.15, highly repeatable torque ripple, due to bearing and/or motor irregularities, was observed in the measured data. The torque ripple was removed in post-processing using spectral decomposition to simplify hysteresis curve fitting (see bottom plot of Fig. 3.15).

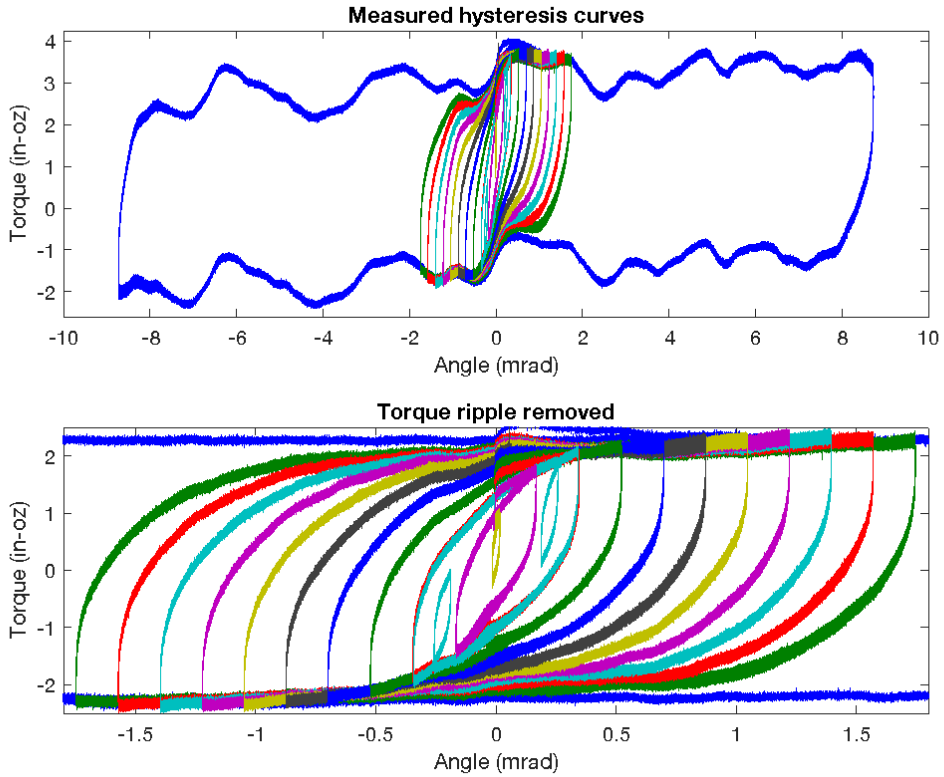

Figure 3.15: Measured hysteresis curves with torque ripple (top) and with torque ripple removed (bottom)

The four friction models were implemented in simulation and subjected to the same motion profiles used to collect the experimental data. Figure 3.16 compares the measured and simulated hysteresis curves for the four different friction models. The SFM and DHM perform similarly for large amplitude motions without minor loops. Both models underestimate the turnaround stiffness

since their friction slope functions are constrained to the form given by Eqs. (3.22) and (3.24). The DHM performs better than the SFM for smaller motions with minor loops since it properly accounts for nonlocal memory effects. The DB-SFM provides an improvement over the SFM since it more accurately matches the overall shape of the measured hysteresis curves. However, it still fails to properly handle minor loop closure due to the lack of nonlocal memory. The DB-DHM has the closest match to the experimental data as it achieves the proper hysteresis shape, exhibits minor loop closure, and accurately captures the stiffness at each turnaround point.

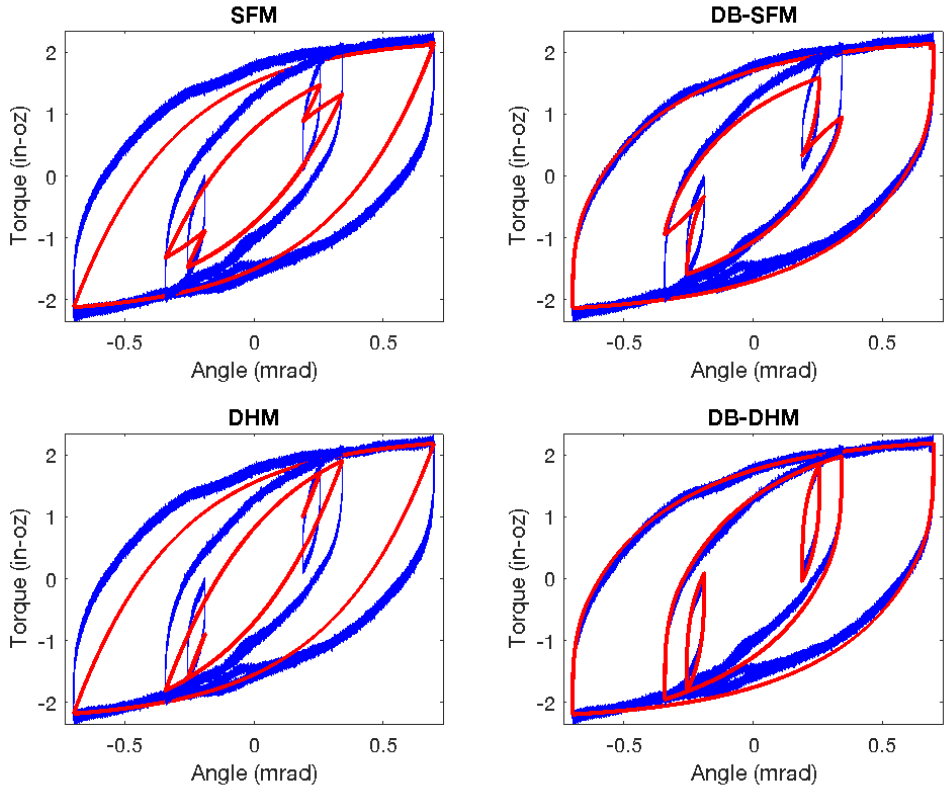

Figure 3.16: Comparison of measured (blue) and simulated (red) hysteresis curves: SFM (top left), DB-SFM (top right), DHM (bottom left), DB-DHM (bottom right)

3.3.2 Frequency-domain validation

The measured frequency response functions (FRFs), shown in Fig. 3.17(a), were obtained by applying various amplitude, open-loop random excitations to the 1-DOF testbed. By applying various excitation levels, the nonlinear behavior induced by dynamic friction can be more easily identified. This is closely related to the describing function method for approximating nonlinearities [58–60]. For small inputs, the system operates primarily in the presliding regime and dynamic friction dominates the system dynamics. In this regime, the system exhibits a linear second-order response characteristic. This behavior can be described by the linearized model developed in Section 3.1.1. Rearranging Eq. (3.4), the transfer function from applied motor torque to angular motion can be expressed as

$$\frac{\theta(s)}{T_m(s)} = \frac{1}{Js^2 + b_f s + k_f} \tag{3.27}$$

where k_f and b_f are the effective (Dahl) frictional stiffness and damping coefficient, respectively. The natural frequency, $\omega_n = \sqrt{\frac{k_f}{J}}$, is known as the "Dahl resonance". For small motions, friction behaves like a very stiff spring (i.e., $k_f \gg 0$) and the corresponding Dahl resonance is high frequency. As the excitation level is increased, the effective stiffness decreases and the Dahl resonance shifts down in frequency. For large motions, the system operates primarily in the sliding regime and the effective stiffness becomes negligible (i.e., $k_f \to 0$). Under this operating condition, the Dahl resonance disappears and the system behaves like a damped inertial system.

To further characterize this behavior, the standard second-order transfer function given in Eq. (3.27) was fit to each of the measured FRFs in Fig. 3.17(a). Figure. 3.17(b) shows the resulting frequency response for each linearized model. Note that the linear models accurately capture the experimentally observed behavior for each of the various excitation levels. The best-fit linearized model parameters, k_f and b_f, are plotted as a function of RMS motion amplitude in Fig. 3.18. Note that the effective Dahl stiffness grows extremely large for motions less than about 1 µrad RMS.

The four friction models discussed in Section 3.2 (SFM, DHM, DB-SFM, DB-DHM) were implemented in simulation and subjected to the same system identification profiles used to collect the experimental data. Since dynamic friction primarily affects the response at lower frequencies, the high frequency flexible modes of the experimental testbed were not modeled. The FRFs were

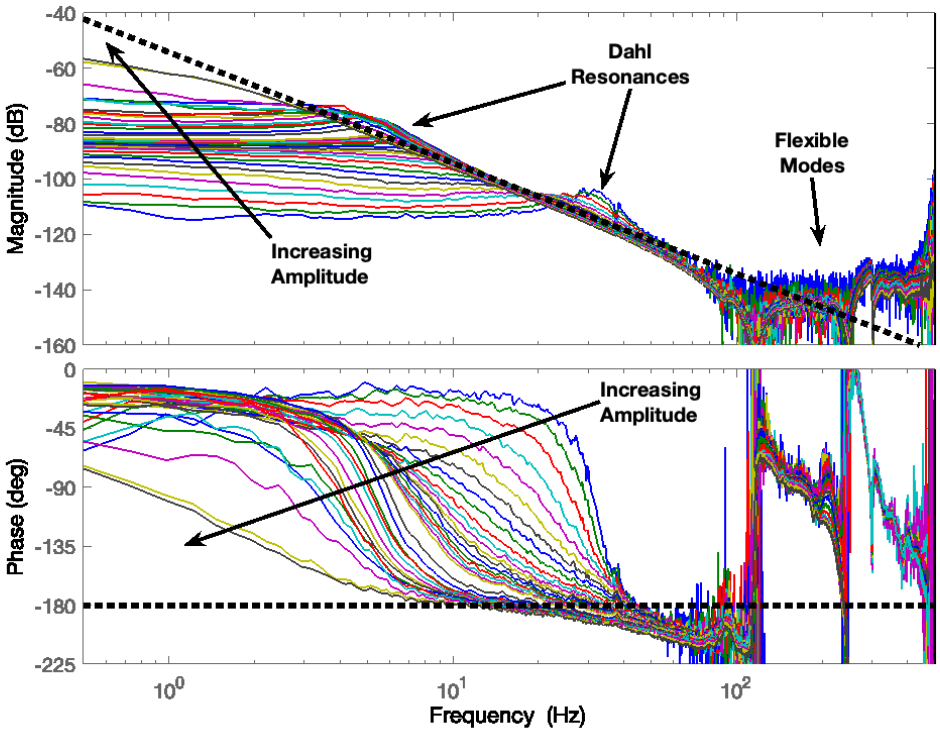

(a) Measured FRFs

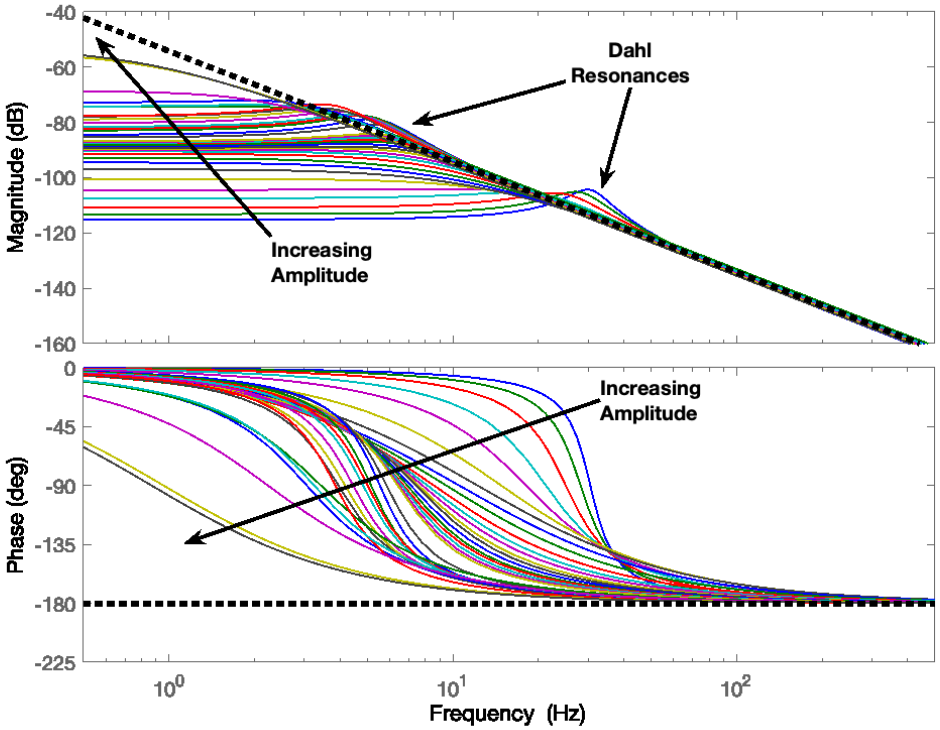

(b) Linearized friction models

Figure 3.17: Frequency responses for various input excitation levels. The ideal rigid body $\left(\frac{1}{Js^2}\right)$ response is indicated by the dotted line.

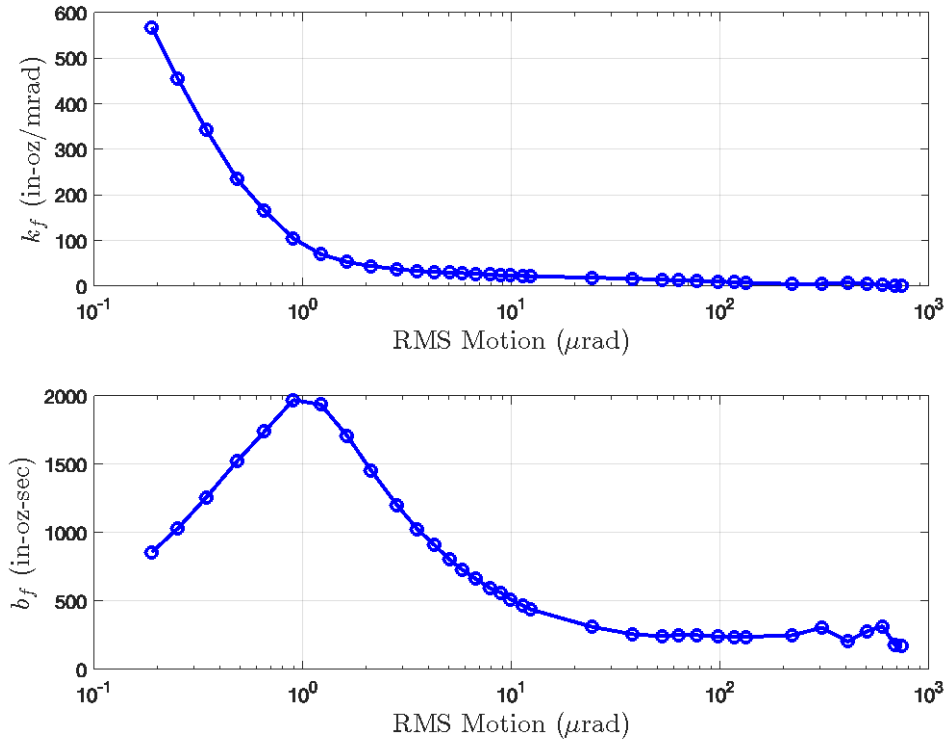

Figure 3.18: Effective Dahl stiffness and damping vs RMS motion amplitude

obtained by applying various amplitude, open-loop random excitations to the motor. In order to evaluate the nonlinear behavior of the four friction models, comparisons are shown for two different (small and large) excitation levels.

Figure 3.19(a) compares the experimental and simulated FRFs for the small input excitation level. For this particular operating condition, the SFM, DB-SFM, and DHM significantly underestimate the effective stiffness as indicated by the low frequency Dahl resonance. The DB-DHM, on the other hand, shows excellent agreement with the experimental data. Figure 3.19(b) compares the experimental and simulated FRFs for the large input excitation level. Although the four different friction models perform similarly in this case, the DB-DHM still provides a better match to the experimental data at low frequency.

Overall, the DB-DHM yields the best accuracy in both the time and frequency domains. The improvement in accuracy is attributed to the DB-DHM's ability to properly model nonlocal memory and turnaround stiffness, as well as the incorporation of the empirical slope function which results in a larger overall effective stiffness. The DB-DHM is used for nonlinear simulation studies of the hybrid flexure bearing.

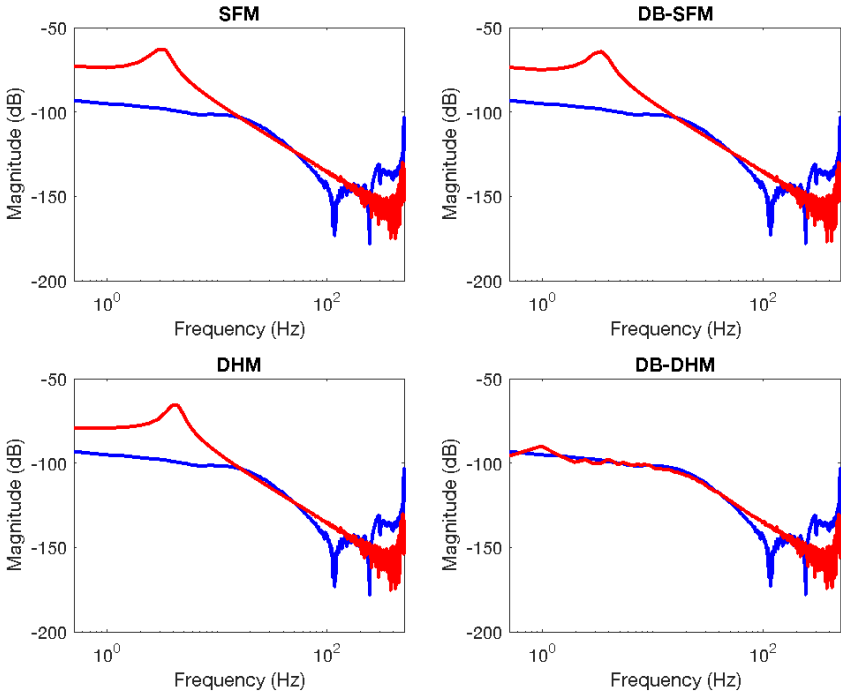

(a)

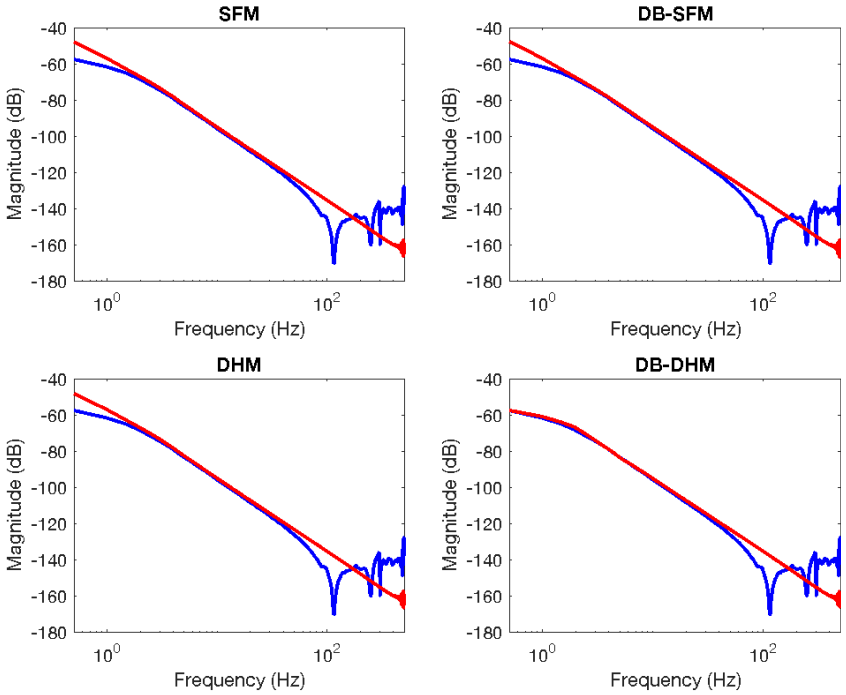

(b)

Figure 3.19: Comparison of measured (blue) and simulated (red) FRFs: (a) small input amplitude (0.02 A), and (b) large input amplitude (1 A)

3.4 Nonlinear Simulation

Figure 3.20 depicts the nonlinear simulation framework developed in this research effort. The simulation is implemented in Simulink and includes models for both the 1-DOF and 2-DOF testbed configurations. The simulation incorporates the nonlinear dynamic friction models discussed in Section 3.2. Various electronics interfaces, such as anti-aliasing filters, A/D converters, D/A converters, and sensor noise models, are included. Relevant sensor and actuator dynamics, including quantization, saturation, and delay, are also modeled. The controller algorithms run at a sample rate of 1200 Hz. System identification routines are implemented in the controller to facilitate model validation. Reference commands and base motion disturbances can be prescribed or played back from recorded experimental data.

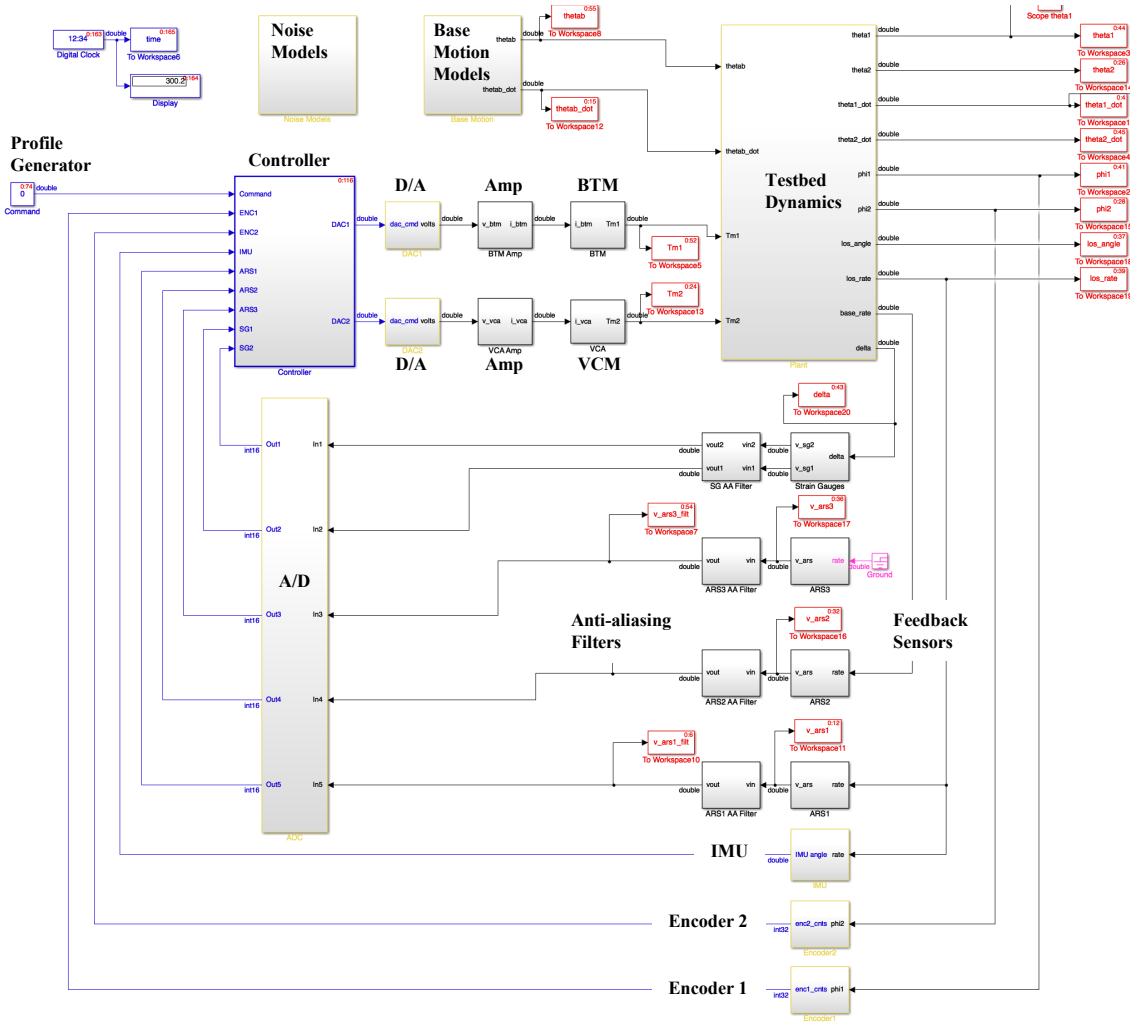

Figure 3.20: Testbed Simulink model

The nonlinear simulation is validated with experimental test data using frequency domain system identification techniques [61, 62]. The experimental FRFs, shown in Fig. 3.21(a), were obtained by applying various amplitude, open-loop random excitations to the 2-DOF testbed. The same open-loop excitations were applied in the nonlinear simulation to generate the FRFs shown in Fig. 3.21(b). Note the good agreement between the experimental and simulated FRFs. Additional system identification results for other input/output pairs are given in Appendix A. Closed-loop simulation results are further validated with experimental data in Chapter 6.

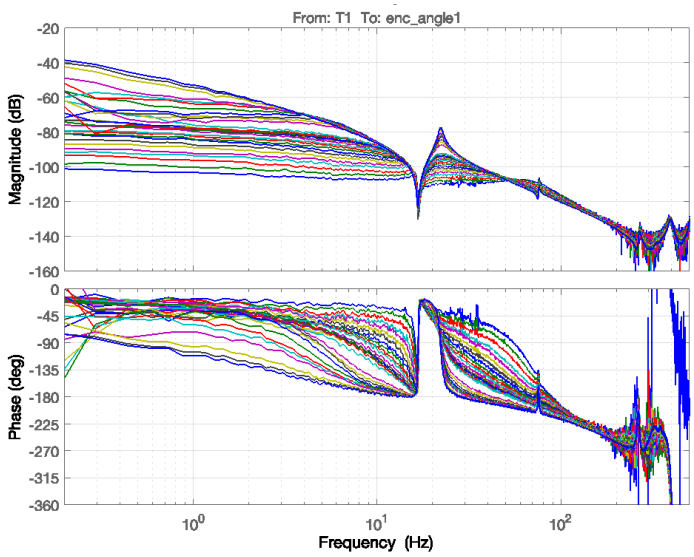

(a) Experimental FRFs

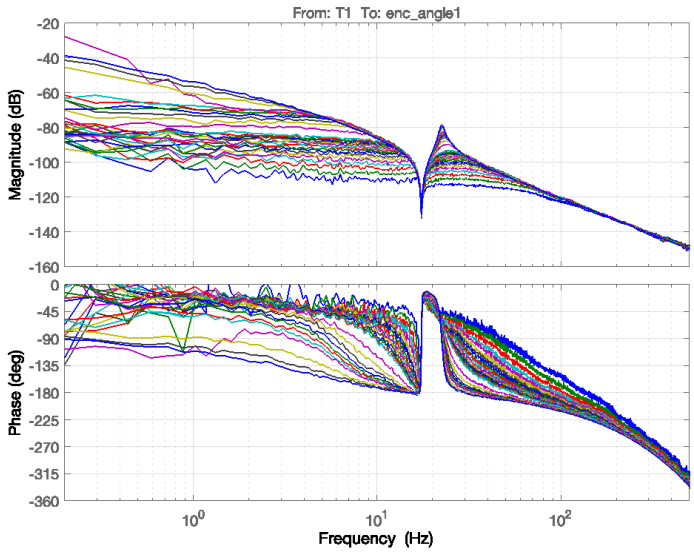

(b) Simulated FRFs

Figure 3.21: Experimental and simulated FRFs for various input excitation levels

3.5 Chapter Summary

This chapter describes the development of linear and nonlinear dynamical models for the hybrid flexure bearing system. A significant challenge associated with the development of precision motion control systems is the identification and modeling of friction. In particular, dynamic presliding friction is often difficult to accurately model in both the time and frequency domains. For systems which undergo small motions with frequent velocity reversals, presliding friction effects dominate the system dynamics and the base motion disturbances and LOS become tightly coupled. An accurate friction model is crucial for assessing the impact of bearing friction on pointing performance.

This chapter presents a data-based dynamic friction model which incorporates an empirical friction slope function to provide a more accurate representation of arbitrarily shaped hysteresis curves. Key friction model features are identified to better match frictional behavior observed in experiments. This data-based approach avoids the added complexity of identifying or fitting model parameters, and can be implemented with a simple look up table. Simulation results are validated with measured friction data collected from the experimental testbed. We show that the data-based approach significantly improves the friction model accuracy in both the time and frequency domains. Model-based friction compensation strategies which utilize the data-based approach to improve pointing performance are discussed in Chapter 6.

Finally, we describe the development of a nonlinear simulation framework which is used for control algorithm development and system trade studies. The nonlinear simulation is experimentally validated using frequency domain system identification techniques. Closed-loop simulation results are further validated with experimental data in Chapter 6.

Chapter 4

TISO System Limitations

Two-input single-output (TISO) feedback systems are found in a wide variety of practical applications which involve two actuators that act together in parallel to produce a desired output. These are commonly referred to as dual-stage or coarse/fine control systems.[1] Examples include nano-positioning systems for scanning probe microscopy (SPM) [67–69] and wafer manufacturing [70], data storage systems such as dual-stage tape drives [71] and hard disk drive (HDD) servos [24,72–80], optical instruments such as interferometers [81–85] and fast steering mirrors [86,87], and automotive applications such as engine throttle control [88] and vehicle steering control [89].

Due to the unique structure of two-input single-output (TISO) feedback systems, several closed-loop properties can be characterized using the concepts of plant and controller "directions" and "alignment" [90]. Poor plant/controller alignment indicates significant limitations in terms of closed-loop performance. In general, it is desirable to design a controller that is well aligned with the plant in order to minimize the size of the closed-loop sensitivity functions and closed-loop interactions at the plant input.

The remainder of this chapter is organized as follows. Section 4.1 describes the TISO feedback system configuration and the relevant transfer functions that dictate closed-loop performance. Section 4.2 introduces the concept of plant/controller alignment and describes its relationship to various closed-loop properties of the TISO feedback configuration. A summary of the chapter is provided in Section 4.3.

[1] The concept of controlling a single variable using two or more inputs is not new and is also known as dual-range control [63], mid-range control [64], input resetting control [65], and main/vernier control [66].

4.1 TISO Feedback Systems

The TISO unity feedback configuration is depicted in Fig. 4.1, where $G(s) \in \mathbb{C}^{1\times 2}$ and $C(s) \in \mathbb{C}^{2\times 1}$ are the plant and controller transfer matrices, respectively, $r \in \mathbb{R}$ is the reference input, $y \in \mathbb{R}$ is the system output, $e \in \mathbb{R}$ is the measured error signal, $u_1 \in \mathbb{R}$ and $u_2 \in \mathbb{R}$ are the control inputs, $n \in \mathbb{R}$ is the measurement noise, $d_{i1} \in \mathbb{R}$ and $d_{i2} \in \mathbb{R}$ are the input disturbances, and $d_o \in \mathbb{R}$ is the output disturbance. The plant and controller can be written as

$$G(s) = \begin{bmatrix} g_1(s) & g_2(s) \end{bmatrix} \quad \text{and} \quad C(s) = \begin{bmatrix} c_1(s) \\ c_2(s) \end{bmatrix} \tag{4.1}$$

where $g_1(s) \in \mathbb{C}$ and $g_2(s) \in \mathbb{C}$ are the elements of the TISO plant, and $c_1(s) \in \mathbb{C}$ and $c_2(s) \in \mathbb{C}$ are the elements of the single-input two-output (SITO) controller.

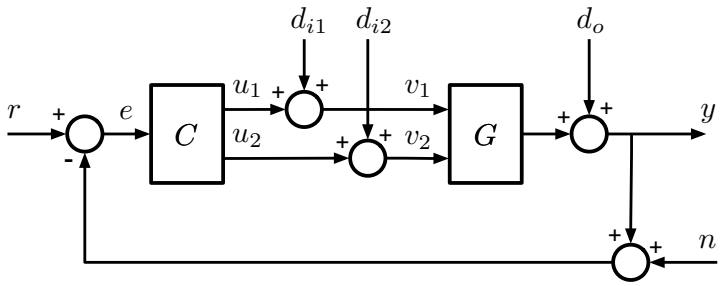

Figure 4.1: TISO feedback system

Omitting the dependence on the frequency variable $s = j\omega$ to simplify notation, it is convenient to define the input and output loop transfer functions as

$$L_I \coloneqq CG \quad \text{and} \quad L_O \coloneqq GC \tag{4.2}$$

where $L_I \in \mathbb{C}^{2\times 2}$ is obtained from breaking the loop at the input of the plant and $L_O \in \mathbb{C}$ is obtained from breaking the loop at the output of the plant. The input sensitivity and complementary sensitivity functions are then defined as

$$S_I \coloneqq (I + L_I)^{-1} \quad \text{and} \quad T_I \coloneqq L_I(I + L_I)^{-1} \tag{4.3}$$

where $S_I \in \mathbb{C}^{2\times 2}$ and $T_I \in \mathbb{C}^{2\times 2}$ must satisfy the identity $S_I + T_I = I$. Similarly, the output sensitivity and complementary sensitivity functions are defined as

$$S_O \coloneqq (1 + L_O)^{-1} \quad \text{and} \quad T_O \coloneqq L_O(1 + L_O)^{-1} \tag{4.4}$$

where $S_O \in \mathbb{C}$ and $T_O \in \mathbb{C}$ must satisfy the identity $S_O + T_O = 1$.

We assume that the closed-loop system is internally stable and write the closed-loop response of the system to exogenous inputs as

$$Y = T_O\,(R - N) + S_O D_O + S_O G D_I \tag{4.5}$$
$$E = S_O\,(R - D_O - N) - S_O G D_I \tag{4.6}$$
$$U = S_I C\,(R - D_O - N) - T_I D_I \tag{4.7}$$
$$V = S_I C\,(R - D_O - N) + S_I D_I \tag{4.8}$$

For the TISO feedback configuration, the output sensitivity and complementary sensitivity functions are scalar valued. As is the case for single-input single-output (SISO) feedback, it follows from Eq. (4.4) that the use of high gain feedback such that $|L_O| \to \infty$ will force $|T_O| \to 1$ and $|S_O| \to 0$. Thus, at frequencies where high gain can be employed, it follows from Eqs. (4.5) and (4.6) that good reference tracking and disturbance rejection can be achieved at the plant output.

On the other hand, the high gain properties at the plant input are not as simple. In general, $S_I \neq S_O$ unless G and C commute (e.g., as in the SISO case). For the TISO feedback configuration, S_I and S_O do not even have the same dimensions. Hence, "small" S_O does not necessarily imply "small" S_I; in other words, good performance at the plant output does not necessarily indicate good performance at the plant input [91]. Indeed, even for systems that achieve reasonable performance at the plant output, very poor performance at the plant input may result from an inappropriate choice of C.

In this chapter, we primarily focus on the input properties of the TISO feedback configuration which are dictated by Eqs. (4.7) and (4.8) through the input sensitivity functions S_I, T_I, and $S_I C$. We adopt the framework presented in [90] which introduces the concepts of plant and controller directions and alignment. These concepts are used to describe the relationship between the open and closed-loop properties of the TISO feedback configuration. The relevant concepts and associated

properties of TISO feedback systems are summarized in Section 4.2.

4.2 TISO Feedback Properties

4.2.1 Plant/controller directions and alignment

The plant and controller transfer matrices given in Eq. (4.1) can be viewed as complex row and column vectors, respectively. Thus, it is useful to define the *plant direction* at frequency ω as the row space of the plant, $\mathcal{R}_{\text{row}}(G(j\omega))$. Likewise, define the *controller direction* at frequency ω as the column space of the controller, $\mathcal{R}(C(j\omega))$.[2] The *alignment angle* between the plant and controller at frequency ω is then defined as [90]

$$\phi(j\omega) \coloneqq \arccos\left(\frac{|G(j\omega)C(j\omega)|}{\|G(j\omega)\|\|C(j\omega)\|}\right) \tag{4.9}$$

where $\|\cdot\|$ denotes the standard vector 2-norm.[3] The argument to the $\arccos(\cdot)$ in Eq. (4.9) is always positive, thus $\phi(j\omega) \in [0°, 90°]$ by definition. We say that the controller and plant are *perfectly aligned* if $\phi(j\omega) = 0°$ and *completely misaligned* if $\phi(j\omega) = 90°$. Furthermore, we say that the plant and controller are *well aligned* if $\phi(j\omega) \approx 0°$ and *poorly aligned* if $\phi(j\omega) \approx 90°$. The varying degrees of alignment between the plant and controller are notionally depicted in Fig. 4.2.

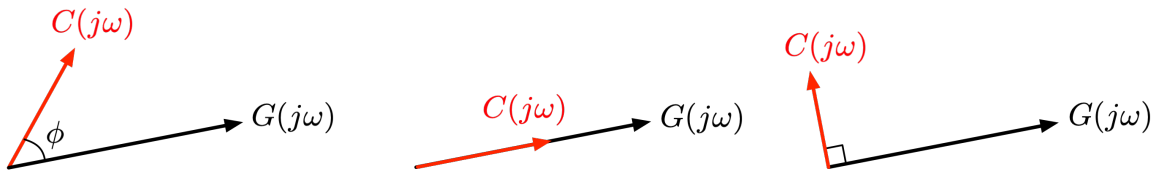

Figure 4.2: Degrees of alignment between complex vectors (notional depiction): (a) The angle between the plant and controller at frequency ω is defined as the plant/controller alignment angle, $\phi(j\omega)$. The plant and controller are considered (b) well aligned if $\phi(j\omega) \approx 0°$, and (c) poorly aligned if $\phi(j\omega) \approx 90°$.

[2] As shown in [90], if G or C has a pole at the frequency of interest, then the direction may be defined from a coprime factorization. That is, let $G = D_G^{-1}N_G$ denote a left coprime polynomial factorization of the plant and $C = N_C D_C^{-1}$ denote a right coprime polynomial factorization of the controller. If $s = j\omega$ is a pole of the plant or controller, then redefine the direction of the plant as $\mathcal{R}_{\text{row}}(N_G(j\omega))$ and the direction of the controller as $\mathcal{R}(N_C(j\omega))$.

[3] This particular definition of the angle between two complex vectors is also known as the Hermitian angle or "first pseudo-angle" [92]. It is geometrically equivalent to the angle between vectors defined in a real vector space, albeit much more difficult to visualize.

4.2.2 Alignment and input response

For the TISO feedback configuration, the size of the input sensitivity and complementary sensitivity is determined by the plant/controller alignment. Omitting the dependence on the frequency variable, $s = j\omega$, bounds on the size of the input sensitivity and complementary sensitivity can be expressed as [90]

$$\|S_I\| \leq \sqrt{1 + |T_O|^2 \tan^2 \phi} + |S_O| \tag{4.10}$$

$$\|S_I\| \leq \max\{1, |S_O|\} + |T_O| \tan \phi \tag{4.11}$$

$$\|S_I\| \geq \max\{\sqrt{1 + |T_O|^2 \tan^2 \phi}, |S_O|\} \tag{4.12}$$

$$\|T_I\| = \frac{|T_O|}{\cos \phi} \tag{4.13}$$

$$\|S_I C\| = \frac{|T_O|}{\|G\| \cos \phi} \tag{4.14}$$

where $\|\cdot\|$ denotes the induced matrix norm (i.e., maximum singular value) in Eqs. (4.10)–(4.13) and the standard vector 2-norm is used in Eq. (4.14).[4] Using high gain feedback such that $|L_O| \to \infty$, $|S_O| \to 0$, and $|T_O| \to 1$, it follows from Eqs. (4.10), (4.12), (4.13), and (4.14) that

$$\|S_I\| \to \frac{1}{\cos \phi} \tag{4.15}$$

$$\|T_I\| \to \frac{1}{\cos \phi} \tag{4.16}$$

$$\|S_I C\| \to \frac{1}{\|G\| \cos \phi} \tag{4.17}$$

Eqs. (4.15)–(4.17) imply that the use of high gain at frequencies where alignment is poor (i.e., as $\phi \to 90°$) forces $\|S_I\|$, $\|T_I\|$, and potentially $\|S_I C\|$ to be very large. In practice, this means that if the size of $\|S_I\|$, $\|T_I\|$, or $\|S_I C\|$ is unacceptable, it will be necessary to use lower gain and/or achieve better plant/controller alignment. This presents a tradeoff between output performance (which requires high gain so that $|S_O|$ is small) and input performance (which requires lower gain and/or better alignment so that $\|S_I\|$ or $\|T_I\|$ is not too large).

[4] To simplify notation, the dependence on the frequency variable $s = j\omega$ is omitted. However, it should be understood that the relationships hold at a fixed frequency, ω.

4.2.3 Alignment and closed-loop interactions

For the TISO feedback configuration, the closed-loop interactions at the plant input are dictated by the plant/controller alignment angle. The input complementary sensitivity function can be expressed in matrix form as

$$T_I = \begin{bmatrix} T_{I11} & T_{I12} \\ T_{I21} & T_{I22} \end{bmatrix} \tag{4.18}$$

The off-diagonal elements of T_I must satisfy the bounds [90]

$$|T_{I12}| + |T_{I21}| \geq |T_O| \tan\phi \tag{4.19}$$

$$|T_{Iij}| \leq \frac{|T_O|}{\cos\phi} \left(1 + \left| \frac{g_i}{g_j} \right|^2 \right)^{-1/2} \quad \text{for } i \neq j \tag{4.20}$$

where g_i and g_j are the elements of the plant transfer matrix given in Eq. (4.1).

Eq. (4.19) implies that the use of high gain at frequencies where alignment is poor (i.e., as $\phi \to 90°$) forces one or both of the off-diagonal elements of T_I to be very large. Likewise, the corresponding off-diagonal elements of S_I will also be very large according to the identity $S_I + T_I = I$. Thus, the closed-loop response will necessarily exhibit strong interactions at the plant input. In practice, this means that a disturbance at the first input to the plant, d_{i1}, will potentially result in a very large response at the second output of the controller, u_2 (and vice versa). This can be problematic, especially if the secondary actuator saturates at a relatively low level.[5] If this is undesirable, it will be necessary to use lower gain and/or achieve better plant/controller alignment.

It is important to note that good alignment cannot necessarily reduce the closed-loop interactions to zero. This is due to the fact that the off-diagonal elements of T_I must also satisfy [90]

$$\max\{|T_{I12}|, |T_{I21}|\} \geq |T_O| \frac{|g_1||g_2|}{|g_1|^2 + |g_2|^2} \tag{4.21}$$

Since this lower bound is independent of the alignment angle, ϕ, it follows that good plant/controller alignment cannot in general reduce the level of interactions to zero. Thus, the fundamental limitation on the minimum level of interactions is imposed by the plant.

[5] For dual-stage feedback systems, it is often the case that the secondary (fine) actuator saturates at a much lower level than the primary (coarse) actuator.

4.2.4 Perfect alignment

We now show that perfectly aligned controllers have special properties. Consider the case where the controller is perfectly aligned with the plant (i.e., $\phi = 0°$). It follows from Eqs. (4.11)–(4.14) that perfect alignment minimizes the sizes of the input sensitivity functions, yielding

$$\|S_I\| = \max\{1, |S_O|\} \tag{4.22}$$

$$\|T_I\| = |T_O| \tag{4.23}$$

$$\|S_I C\| = \frac{|T_O|}{\|G\|} \tag{4.24}$$

Similarly, it follows from Eqs. (4.19) and (4.20) that perfect alignment minimizes the closed-loop interactions at the plant input. Note, however, that perfect alignment does not necessarily reduce the level of interactions to zero, but to the minimum possible level dictated by the plant. With perfect alignment, the minimum level of interactions is given by [90]

$$|T_{I12}| = |T_{I21}| = |T_O| \frac{|g_1||g_2|}{|g_1|^2 + |g_2|^2} \tag{4.25}$$

where g_1 and g_2 are the elements of the plant transfer matrix given in Eq. (4.1). It is straightforward to show that the maximum possible level of closed-loop interactions associated with a perfectly aligned controller is given by

$$|T_{I12}| = |T_{I21}| \leq \frac{1}{2}|T_O| \tag{4.26}$$

where the upper bound is attained when $\left|\frac{g_1}{g_2}\right| = 1$.

Although the above results indicate that the controller should be well aligned with the plant at all frequencies, this interpretation must be viewed with caution. Requiring perfect alignment at all frequencies will necessarily introduce one or more non-minimum phase (NMP) zeros into the open loop transfer function if the plant direction varies with frequency. These unstable zeros can limit the achievable closed-loop bandwidth of the system. These issues are discussed in greater detail in the following sections.

4.2.5 Conditions for perfect alignment

Define the *plant ratio* as $P \coloneqq \frac{g_1}{g_2}$ and the *controller ratio* as $Q \coloneqq \frac{c_1}{c_2}$. We refer to $|P| = \left|\frac{g_1}{g_2}\right|$ as the *plant gain ratio* and $\angle P = \angle\left(\frac{g_1}{g_2}\right)$ as the *plant phase ratio*. Similarly, we refer to $|Q| = \left|\frac{c_1}{c_2}\right|$ as the *controller gain ratio* and $\angle Q = \angle\left(\frac{c_1}{c_2}\right)$ as the *controller phase ratio*. We start with the definition of the plant/controller alignment angle given by Eq. (4.9) and expand in terms of the plant and controller ratios

$$\begin{aligned}\cos\phi &= \frac{|GC|}{\|G\|\|C\|} \\ &= \frac{|g_1c_1 + g_2c_2|}{\sqrt{|g_1|^2 + |g_2|^2}\sqrt{|c_1|^2 + |c_2|^2}} \\ &= \frac{|1 + PQ|}{\sqrt{1 + |P|^2 + |Q|^2 + |PQ|^2}}\end{aligned} \tag{4.27}$$

Assuming perfect alignment (i.e., $\phi = 0°$) in Eq. (4.27), we can write

$$|1 + PQ|^2 = 1 + |P|^2 + |Q|^2 + |PQ|^2 \tag{4.28}$$

To satisfy Eq. (4.28), perfect alignment requires that the controller gain and phase ratios satisfy the following conditions

$$|Q| = |P| \tag{4.29}$$

$$\angle Q = -\angle P \tag{4.30}$$

The two conditions in Eqs. (4.29) and (4.30) are equivalent to requiring that

$$Q(s) = P(-s) \tag{4.31}$$

The following section shows that imposing these conditions on the controller over all frequencies is problematic because it implies that L_O will necessarily be non-minimum phase (NMP).

4.2.6 Issues in requiring perfect alignment

Consider the extreme case for which the controller is required to be perfectly aligned with the plant at all frequencies. Hence, the controller ratio must satisfy the condition in Eq.(4.31). It is well-known that the Bode gain-phase integrals constrain the relationship between gain and phase of a stable minimum phase rational transfer function [93]. Thus, it is not surprising that these conditions may be difficult to satisfy. Indeed, it can be shown that if the direction of the plant varies with frequency, then requiring the alignment conditions to hold implies that L_O will necessarily be non-minimum phase (NMP). Proof of this limitation is given in [93, 94] for the SITO feedback case. In a similar manner, we show the same limitation for the TISO feedback case which is dual to the SITO case.

Factor the plant and controller as

$$G = D_G^{-1} N_G = D_G^{-1} \begin{bmatrix} n_{g1} & n_{g2} \end{bmatrix} \tag{4.32}$$

$$C = N_C D_C^{-1} = \begin{bmatrix} n_{c1} \\ n_{c2} \end{bmatrix} D_C^{-1} \tag{4.33}$$

where (n_{g1}, n_{g2}) and (n_{c1}, n_{c2}) are pairs of coprime polynomials, and D_G^{-1} and D_C^{-1} are rational transfer functions. Based on the results of Section 4.2.5, the plant and controller are perfectly aligned if the controller has the form

$$C(s) = D_C^{-1}(s) \begin{bmatrix} n_{g1}(-s) \\ n_{g2}(-s) \end{bmatrix} \tag{4.34}$$

The output open loop transfer function can then be expressed as

$$\begin{aligned} L_O(s) &= G(s)C(s) \\ &= D_G^{-1}(s) \begin{bmatrix} n_{g1}(s) & n_{g2}(s) \end{bmatrix} D_C^{-1}(s) \begin{bmatrix} n_{g1}(-s) \\ n_{g2}(-s) \end{bmatrix} \\ &= D_G^{-1}(s) D_C^{-1}(s) \left[n_{g1}(s) n_{g1}(-s) + n_{g2}(s) n_{g2}(-s) \right] \end{aligned} \tag{4.35}$$

Similar to the SITO case discussed in [93], unless the plant direction is constant over frequency, Eq. (4.35) shows that L_O must have zeros that are distributed symmetrically about the $j\omega$-axis. The assumption that n_{g1} and n_{g2} are coprime implies that there are no zeros on the $j\omega$-axis. It follows that L_O must have at least one zero in the open right half plane (ORHP). This is problematic since NMP zeros of L_O will impose design limitations on S_O. That is, if $|S_O| \ll 1$ at lower frequencies, then $|S_O| \gg 1$ at higher frequencies. Consequently, this tradeoff limits the achievable closed-loop bandwidth [95–97]. Fortunately, perfect alignment is not necessary to achieve satisfactory performance.

So then, how much misalignment is acceptable? It is shown in [90] that closed-loop performance is relatively insensitive to moderate deviations from $\phi = 0°$, and that the closed-loop response is insensitive to alignment at frequencies for which the gain is sufficiently small (i.e., outside the closed-loop bandwidth). Using Eq. (4.13) to demonstrate this insensitivity, we have

$$\begin{aligned} \phi = 25° \quad &\Longrightarrow \quad \|T_I\| = 1.1\,|T_O| \\ \phi = 45° \quad &\Longrightarrow \quad \|T_I\| = 1.4\,|T_O| \\ \phi = 60° \quad &\Longrightarrow \quad \|T_I\| = 2.0\,|T_O| \end{aligned}$$

Thus, perfect alignment is not necessary to achieve reasonable performance. The alignment angle is a more useful indicator of poor performance when alignment is poor. Ultimately, it is important to avoid poor alignment, but it is not necessary to demand perfect alignment over all frequencies.

4.3 Chapter Summary

This chapter described the TISO feedback system configuration and the relevant transfer functions that dictate closed-loop performance. We introduced the concept of plant/controller alignment and described its relationship to various closed-loop properties of the TISO feedback configuration. In general, it is desirable to design a controller that is well aligned with the plant in order to minimize the size of the closed-loop sensitivity functions and closed-loop interactions at the plant input. Although the concept of alignment can be a useful analysis tool for a given plant/controller pair, it is

not obvious how a controller should be designed to achieve good alignment. In Chapter 5, we present a new controller design approach, based on the PQ method [24], which explicitly incorporates knowledge of alignment into the design process.

Chapter 5

TISO Control Design

In Chapter 4, it was shown that several closed-loop properties of TISO feedback systems can be characterized using the concepts of plant and controller directions and alignment. Poor plant/controller alignment indicates significant limitations in terms of closed-loop performance. In general, it is desirable to design a controller that is well aligned with the plant in order to minimize the size of the closed-loop sensitivity functions and closed-loop interactions at the plant input. Although the concept of alignment can be a useful analysis tool for a given plant/controller pair (e.g., see [98,99]), it is not obvious how a controller should be designed to achieve good alignment with a particular plant over frequency. In this chapter, we present a new controller design approach, based on the PQ method [24], which explicitly incorporates knowledge of alignment into the design process [100, 101]. This is accomplished by providing graphical information about the alignment angle on the Bode plot of the PQ frequency response.

The remainder of the chapter is organized as follows. Section 5.1 summarizes some of the common TISO control design approaches. Section 5.2 summarizes TISO controller design using the PQ method and introduces a new graphical approach that explicitly accounts for plant/controller alignment. A brief chapter summary is given in Section 5.3.

5.1 TISO Control Design Approaches

Much of the prior work in TISO control system design stems from the development of dual-stage HDD servos in the early 1990s through the late 2000s. These approaches can be largely classified into two main categories: those based on classical SISO design methods, and those based on optimal and robust multiple-input multiple-output (MIMO) design techniques [78]. Some of the common approaches and different control architectures are depicted in Fig. 5.1.

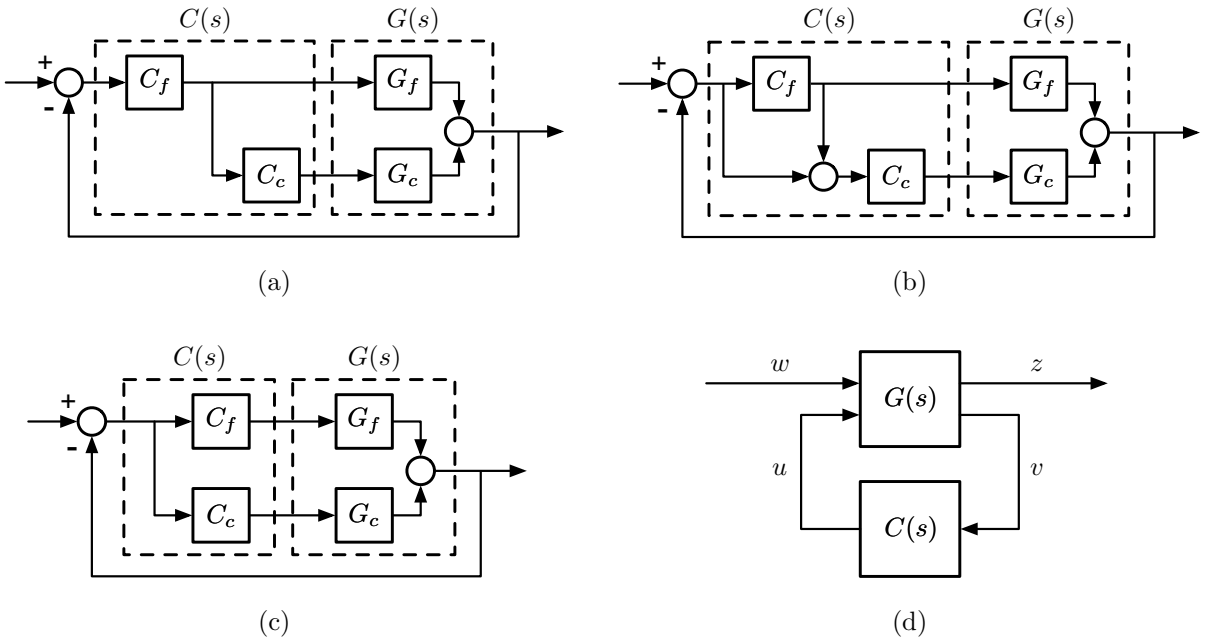

Figure 5.1: TISO control design approaches: (a) Master-slave design, (b) decoupled master-slave design, (c) direct parallel design, and (d) general MIMO design

The SISO design methods take advantage of the structure of TISO feedback systems which is much simpler than the structure of general MIMO systems. Most of the SISO methodologies for dual-stage servo design treat the problem as a sequence of SISO designs [78]. Examples include the master-slave method [73], decoupled master-slave method [72] (also known as the sensitivity decoupling method), and direct parallel design method [76]. Detailed comparisons of some of the common dual-stage loop configurations are given in [75, 76, 79]. The underlying assumption for most of these approaches is that there is very little interaction or dynamic coupling between the coarse and fine stages. Although this can be a reasonable assumption if the mass of the fine stage is negligible compared to the coarse stage, it is not a valid assumption in general. Thus, there is usually more interaction than the approximation warrants and the performance of the closed-loop system degrades [24, 102]. In practice, the use of decoupling controllers are often problematic because they use an internal model of the system, thus the overall performance can be quite sensitive to model uncertainty [65, 103, 104]. An alternative approach, known as the PQ method [24], also treats the TISO control problem as a sequence of SISO designs. However, it is quite different than the other approaches and does not rely on the assumption that there is little interaction between the SISO loops.

Given that TISO systems are considered a subset of MIMO systems, general MIMO control design techniques can still be applied. MIMO methods are based on modern optimal control techniques and have been successfully applied to various TISO control problems. Examples include LQG/LTR methods [102,105,106], $\mathcal{H}_\infty$ and μ-synthesis methods [105,107–109], and mixed $\mathcal{H}_2/\mathcal{H}_\infty$ optimization methods [110–113]. The design process then mostly involves the selection of appropriate weighting functions to achieve desired performance specifications. Disadvantages of these methods are that they are usually best applied to continuous-time linear models, and typically generate high-order compensators which can be difficult to implement in practice [24, 77, 79, 114, 115].

None of the aforementioned control design techniques explicitly take into account the concept of plant/controller alignment. Although, there have been some efforts to incorporate alignment into the design of controllers for two-input two-output (TITO) systems. A decentralized control design procedure which exploits alignment is developed in [116], however, the approach is only applicable to ill-conditioned TITO systems. In [98] and [99], a multivariable controller is designed for a TITO system using sequential loop closure. An intermediate SITO subsystem is formed by closing the first loop, and the first portion of the controller is designed to achieve good alignment. Then, the second loop is closed and the remaining portion of the controller is designed. In both cases, static controller gains are used to improve alignment at a single frequency (i.e., at DC) only. It is not clear how to select dynamic compensators to improve alignment over frequency using these methods.

Section 5.2 presents a new approach which incorporates knowledge of the alignment explicitly into the controller design process for TISO feedback systems. We use the well-known PQ method [24] as the basis of this approach as it is particularly well suited to fit within the alignment framework described in Chapter 4.

5.2 TISO Control Design Exploiting Plant/Controller Alignment

In Section 4.2, we showed how plant/controller alignment relates to various closed-loop properties of the TISO feedback configuration. In general, it is desirable to design a well-aligned controller to minimize the size of the input sensitivity functions and closed-loop interactions at the plant input. Although it is straightforward to evaluate the alignment angle over frequency using Eq. (4.9) for a

given plant/controller pair, it is not entirely clear how a controller should be designed to achieve good alignment with a particular plant. Thus, it would be beneficial to include knowledge of alignment in the controller design process itself. In this section, we introduce a new approach which incorporates knowledge of the alignment explicitly into the controller design process. We use the well-known PQ method [24] as the basis of this approach as it is well suited to fit within the framework discussed in Section 4.2. The PQ design procedure is briefly summarized below.

5.2.1 PQ method

The PQ method [24] is a straightforward controller design technique which transforms the TISO feedback problem into two individual SISO design problems as depicted in Fig. 5.2. This is accomplished by splitting the controller into pre- and post-compensation parts such that

$$C(s) \coloneqq c_0(s) \begin{bmatrix} c_1'(s) \\ c_2'(s) \end{bmatrix} \tag{5.1}$$

where $c_1'(s)$ and $c_2'(s)$ are the pre-compensator elements, and $c_0(s)$ is the post-compensator. The PQ method consists of two primary steps. The first step involves the construction of the G_{SISO} subsystem shown in Fig. 5.2(b), also known as "squaring down" the plant [117]. The second step designs a feedback controller, $c_0(s)$, for the G_{SISO} subsystem which satisfies stability and performance requirements. The pre-compensators, $c_1'(s)$ and $c_2'(s)$, are simultaneously selected to obtain G_{SISO} such that the following conditions are satisfied:

1. Ensure G_{SISO} is minimum phase to avoid inherent bandwidth limitations. The parallel combination G_{SISO} can become non-minimum phase even when $c_1'(s)g_1(s)$ and $c_2'(s)g_2(s)$ are both individually minimum phase [118].

2. Ensure the relative output contribution of each path is appropriately allocated over frequency. Often, parallel actuators are selected to perform better in different frequency ranges.

3. Minimize destructive interference due to relative phase lag between paths. Interference occurs when two actuators effectively cancel each other to yield a net output near zero.

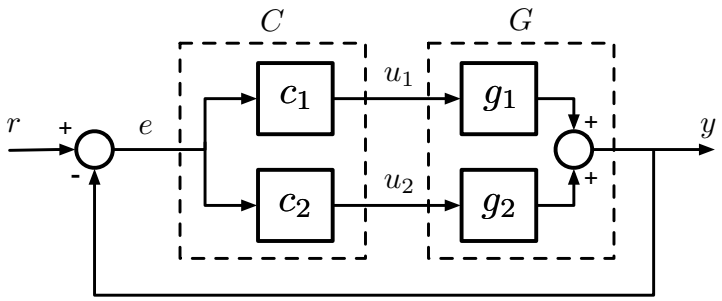

(a) TISO feedback system

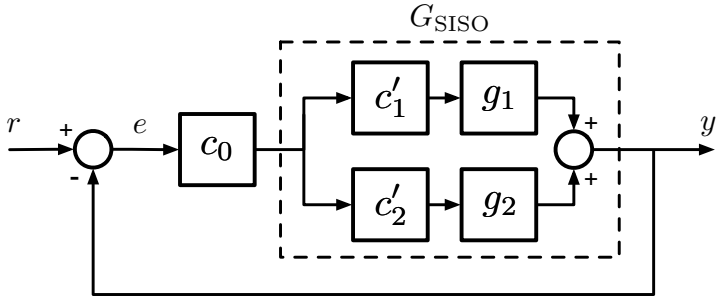

(b) SISO equivalent system

Figure 5.2: PQ equivalent representation

To assist with the selection of $c_1'(s)$ and $c_2'(s)$ which satisfy the above conditions, a fictitious "PQ" feedback system is constructed as follows. The zeros of G_{SISO} can be expressed as the solution to the equation

$$G_{\text{SISO}}(s) = c_1'(s)g_1(s) + c_2'(s)g_2(s) = 0 \tag{5.2}$$

The *plant ratio* and *controller ratio* are defined as

$$P(s) \coloneqq \frac{g_1(s)}{g_2(s)} \quad \text{and} \quad Q(s) \coloneqq \frac{c_1(s)}{c_2(s)} = \frac{c_1'(s)}{c_2'(s)}, \tag{5.3}$$

respectively. Rearranging Eq. (5.2), we can write

$$1 + \frac{g_1(s)c_1'(s)}{g_2(s)c_2'(s)} = 1 + P(s)Q(s) = 0 \tag{5.4}$$

Equation (5.4) represents the characteristic equation of the PQ feedback system depicted in Fig. 5.3. The closed-loop poles of the PQ feedback system are the zeros of G_{SISO}. Thus, selecting Q to stabilize the PQ feedback system ensures that G_{SISO} will have stable (i.e., minimum phase)

zeros, thereby satisfying condition #1. The magnitude of PQ determines the relative contributions of the parallel paths as a function of frequency. The 0 dB crossover of $|PQ|$ is the *hand-off frequency* at which the parallel paths contribute equally, and can be selected via proper tuning of Q to satisfy condition #2. The phase of PQ determines the relative stability of the zeros of G_{SISO} and also dictates the amount of destructive interference which occurs between the parallel subsystems. Destructive interference can be avoided by selecting the phase margin to be greater than 60 degrees [24], thus satisfying condition #3. Frequency domain techniques are well suited for the design of Q, which effectively transforms the selection of pre-compensators c_1' and c_2' into a PQ loop shaping exercise as depicted in Fig. 5.4.

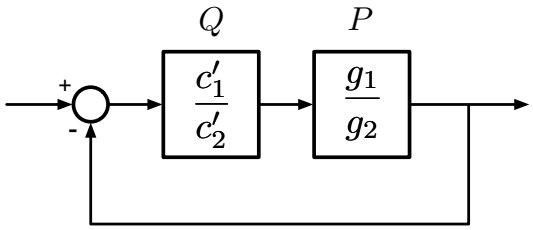

Figure 5.3: PQ feedback system

Unlike MIMO control design techniques, a significant disadvantage of the PQ method is that it does not explicitly take into account closed-loop performance at the plant input. This is a direct result of treating the TISO feedback problem as two separate SISO problems. In fact, the input response of the TISO feedback system becomes completely masked in the formation of G_{SISO} as shown in Fig. 5.2(b). Furthermore, the PQ method provides no insight into system performance limitations with respect to plant/controller alignment as described in Section 4.2. Clearly, the selection of Q (and hence c_1' and c_2') will directly influence plant/controller alignment. However, the relationship between alignment and the PQ loop shape is nonintuitive. In the following section, we describe a new approach that augments the PQ design procedure with additional information regarding plant/controller alignment so that the designer can make well-informed choices (from the perspective of input response) when shaping the PQ feedback loop.

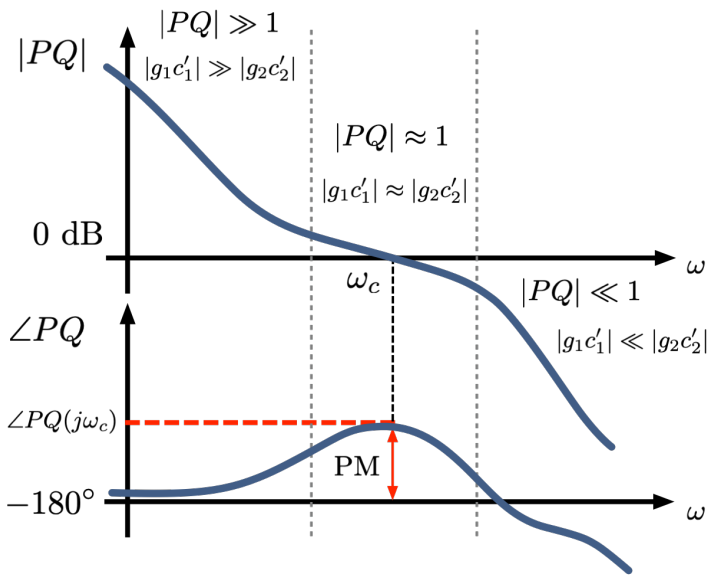

Figure 5.4: PQ Bode plot

5.2.2 Alignment contours

To incorporate alignment into the PQ loop shaping process, we modify the conventional Bode plot by adding magnitude and phase contours which represent specific values of the plant/controller alignment angle over frequency. The intersection of the PQ magnitude and phase responses with these contours indicate frequencies at which the alignment angle reaches a particular value. This allows the designer to easily determine the alignment over frequency for a given PQ loop shape. More importantly, the contours provide additional guidelines in the loop shaping process. This is similar to the Bode sensitivity and robustness contours developed in [119–122]. However, in the context of plant/controller alignment, the contours are used on the Bode plot of the PQ loop shape instead of the open loop transfer function.

To derive the magnitude and phase contours, we start with the definition of the plant/controller alignment angle given by Eq. (4.9) and expand in terms of the plant and controller ratios

$$\begin{aligned}\cos\phi &= \frac{|GC|}{\|G\|\|C\|} \\ &= \frac{|g_1c_1 + g_2c_2|}{\sqrt{|g_1|^2 + |g_2|^2}\sqrt{|c_1|^2 + |c_2|^2}} \\ &= \frac{|1 + PQ|}{\sqrt{1 + |P|^2 + |Q|^2 + |PQ|^2}}\end{aligned} \tag{5.5}$$

where P and Q are the plant and controller ratios defined by Eq. (5.3). Squaring both sides of Eq. (5.5) and expanding, we can write

$$\begin{aligned}\left(1+|P|^2+|Q|^2+|PQ|^2\right)\cos^2\phi &= |1+PQ|^2 \\ &= (1+PQ)\left(1+\overline{PQ}\right) \\ &= 1+|PQ|\left(e^{j(\angle P+\angle Q)}+e^{-j(\angle P+\angle Q)}\right)+|PQ|^2 \\ &= 1+2\cos\left(\angle P+\angle Q\right)|PQ|+|PQ|^2 \\ &= 1+2\cos\left(\angle PQ\right)|PQ|+|PQ|^2 \end{aligned} \tag{5.6}$$

Rearranging Eq. (5.6), we obtain a quadratic equation in terms of $|PQ|$

$$\left(\frac{\cos^2\phi}{|P|^2}+\cos^2\phi-1\right)|PQ|^2-2\cos\left(\angle PQ\right)|PQ|+\left(|P|^2\cos^2\phi+\cos^2\phi-1\right)=0 \tag{5.7}$$

The solutions to this quadratic equation relate the magnitude and phase of the plant and controller ratios required to achieve a given alignment angle. Note that the values of $|PQ|$ and $\angle PQ$ at a particular frequency can be taken directly from the PQ Bode plot.

Derivation of magnitude contours

Using the quadratic formula, we can solve Eq. (5.7) for the magnitude contour in terms of the phase of the plant and controller ratios and the alignment angle. The magnitude contour is then defined as

$$\begin{aligned}M_a(j\omega,\phi) \coloneqq \frac{1}{|P|^{-2}\cos^2\phi+\cos^2\phi-1}\Bigg[\cos\left(\angle PQ\right)\pm\Big\{\cos^2(\angle PQ)-\left(|P|^{-2}\cos^2\phi+\cos^2\phi-1\right) \\ \times\left(|P|^2\cos^2\phi+\cos^2\phi-1\right)\Big\}^{\frac{1}{2}}\Bigg]\end{aligned} \tag{5.8}$$

The solutions given by Eq. (5.8) are only valid for non-negative real values. Thus, any negative real or complex solutions are discarded. It is useful to plot contours for several different values of the alignment angle in fixed intervals between 0° and 90°, $\phi_k=(k-1)\,\Delta\phi$ for $k=1,2,\ldots,n$; where $\Delta\phi=90^\circ/(n-1)$ and n is the number of contour levels. The intersections between $|P(j\omega)Q(j\omega)|$

and $M_a(j\omega, \phi_k)$ on the Bode magnitude plot are the frequencies for which $\phi = \phi_k$. Note that $M_a(j\omega, \phi_k)$ does not depend on $|PQ|$, thus shifting the magnitude of PQ with a constant gain does not affect the magnitude contours. As a result, it is easy to see how changing the PQ loop gain will affect the alignment angle over frequency.

Derivation of phase contours

In a similar manner, the phase contour can be determined by solving Eq. (5.7) for phase in terms of the magnitudes of the plant and controller ratios and the alignment angle. The phase contour is then defined as

$$\Phi_a(j\omega, \phi) \coloneqq \arccos\left[\frac{1}{2|PQ|}\left\{\left(\frac{\cos^2\phi}{|P|^2} + \cos^2\phi - 1\right)|PQ|^2 + |P|^2\cos^2\phi + \cos^2\phi - 1\right\}\right] \tag{5.9}$$

where Φ_a is only valid when the solution to Eq. (5.9) is real-valued. The intersections between $\angle P(j\omega)Q(j\omega)$ and $\Phi_a(j\omega, \phi_k)$ on the Bode phase plot are the frequencies for which $\phi = \phi_k$. In the following chapter, we present a design example which shows the utility of the magnitude and phase contours on the PQ Bode plot.

5.2.3 Relationship between PQ and TISO sensitivities

Consider again the PQ feedback system depicted in Fig. 5.3. The sensitivity and complementary sensitivity functions of the PQ feedback system can be written as

$$L_{PQ} = PQ = \frac{g_1}{g_2}\frac{c_1}{c_2} = \frac{g_1}{g_2}\frac{c_1'}{c_2'} \tag{5.10}$$

$$T_{PQ} = \frac{L_{PQ}}{1 + L_{PQ}} = \frac{g_1c_1}{g_1c_1 + g_2c_2} = \frac{g_1c_1}{L_O} = \frac{g_1c_1'}{G_{\text{SISO}}} \tag{5.11}$$

$$S_{PQ} = \frac{1}{1 + L_{PQ}} = \frac{g_2c_2}{g_1c_1 + g_2c_2} = \frac{g_2c_2}{L_O} = \frac{g_2c_2'}{G_{\text{SISO}}} \tag{5.12}$$

where T_{PQ} represents the contribution of the primary (coarse) actuator over frequency, and S_{PQ} represents the contribution of the secondary (fine) actuator over frequency.

Expanding Eq. (4.4), the scalar-valued output sensitivity and complementary sensitivity of the

TISO feedback system can be expressed as

$$L_O = GC = g_1c_1 + g_2c_2 \tag{5.13}$$

$$T_O = \frac{L_O}{1 + L_O} = \frac{g_1c_1 + g_2c_2}{1 + g_1c_1 + g_2c_2} \tag{5.14}$$

$$S_O = 1 - T_O = \frac{1}{1 + g_1c_1 + g_2c_2} \tag{5.15}$$

Using Eq. (4.3), the input sensitivity and complementary sensitivity of the TISO feedback system can be expanded as

$$L_I = CG = \begin{bmatrix} g_1c_1 & g_2c_1 \\ g_1c_2 & g_2c_2 \end{bmatrix} \tag{5.16}$$

$$T_I = L_I(I + L_I)^{-1} = \begin{bmatrix} \dfrac{g_1c_1}{1 + g_1c_1 + g_2c_2} & \dfrac{g_2}{g_1}\left(\dfrac{g_1c_1}{1 + g_1c_1 + g_2c_2}\right) \\ \dfrac{g_1}{g_2}\left(\dfrac{g_2c_2}{1 + g_1c_1 + g_2c_2}\right) & \dfrac{g_2c_2}{1 + g_1c_1 + g_2c_2} \end{bmatrix} \tag{5.17}$$

$$S_I = (I + L_I)^{-1} = \begin{bmatrix} 1 - \dfrac{g_1c_1}{1 + g_1c_1 + g_2c_2} & -\dfrac{g_2}{g_1}\left(\dfrac{g_1c_1}{1 + g_1c_1 + g_2c_2}\right) \\ -\dfrac{g_1}{g_2}\left(\dfrac{g_2c_2}{1 + g_1c_1 + g_2c_2}\right) & 1 - \dfrac{g_2c_2}{1 + g_1c_1 + g_2c_2} \end{bmatrix} \tag{5.18}$$

Now, combining all of the above relationships, the TISO input sensitivity functions can be rewritten in terms of the TISO output sensitivities and the PQ sensitivities

$$T_I = T_O \begin{bmatrix} T_{PQ} & P^{-1}T_{PQ} \\ PS_{PQ} & S_{PQ} \end{bmatrix} \tag{5.19}$$

$$S_I = \begin{bmatrix} S_O + T_OS_{PQ} & -P^{-1}T_OT_{PQ} \\ -PT_OS_{PQ} & S_O + T_OT_{PQ} \end{bmatrix} \tag{5.20}$$

It is clear from Eqs. (5.19) and (5.20) how the individual elements of the input sensitivity functions, S_I and T_I, are determined by the PQ design. The first step of the PQ method effectively sets S_{PQ} and T_{PQ} by the appropriate shaping of L_{PQ}. The second step of the PQ method sets S_O and T_O

through the appropriate shaping of L_O via feedback compensator c_0. Note that the plant ratio, P, affects the size of the off-diagonal terms of both S_I and T_I, hence plays a role in the level of closed-loop interactions as discussed in Section 4.2.3.

Starting with Eq. (4.9), it is also possible to rewrite the expression for alignment angle in terms of the PQ sensitivities

$$\begin{aligned}\cos\phi &= \frac{|GC|}{\|C\|\|G\|} \\ &= \frac{|1+PQ|}{\sqrt{1+|P|^2+|Q|^2+|PQ|^2}} \\ &= \frac{1}{\sqrt{(1+|P|^2)\,|S_{PQ}|^2+(1+|P^{-1}|^2)\,|T_{PQ}|^2}}\end{aligned} \tag{5.21}$$

First, consider the case when the coarse actuator dominates such that $|L_{PQ}| \to \infty$, $|S_{PQ}| \to 0$, and $|T_{PQ}| \to 1$. In this case, the alignment angle is dictated by

$$\phi = \arccos\left[\left(1+|P^{-1}|^2\right)^{-\frac{1}{2}}\right] = \arccos\left[\left(1+\left|\frac{g_2}{g_1}\right|^2\right)^{-\frac{1}{2}}\right] \tag{5.22}$$

Thus, alignment will be good (i.e., $\phi \approx 0^\circ$) if $|g_1| \gg |g_2|$. Conversely, alignment will be poor (i.e., $\phi \approx 90^\circ$) if $|g_1| \ll |g_2|$. This is indicated by the blue curve in Fig. 5.5.

Similarly, consider the case when the fine actuator dominates such that $|L_{PQ}| \to 0$, $|S_{PQ}| \to 1$, and $|T_{PQ}| \to 0$. In this case, the alignment angle is dictated by

$$\phi = \arccos\left[\left(1+|P|^2\right)^{-\frac{1}{2}}\right] = \arccos\left[\left(1+\left|\frac{g_1}{g_2}\right|^2\right)^{-\frac{1}{2}}\right] \tag{5.23}$$

Here, we see that alignment will be good (i.e., $\phi \approx 0^\circ$) if $|g_2| \gg |g_1|$. Conversely, alignment will be poor (i.e., $\phi \approx 90^\circ$) if $|g_2| \ll |g_1|$. This is depicted by the green curve in Fig. 5.5.

Finally, consider the case when both coarse/fine actuators are contributing equally near handoff for which $|L_{PQ}| \approx 1$ such that $|S_{PQ}| \approx |T_{PQ}| \approx \frac{0.5}{\cos(0.5\angle L_{PQ})}$. In this case, the alignment angle is

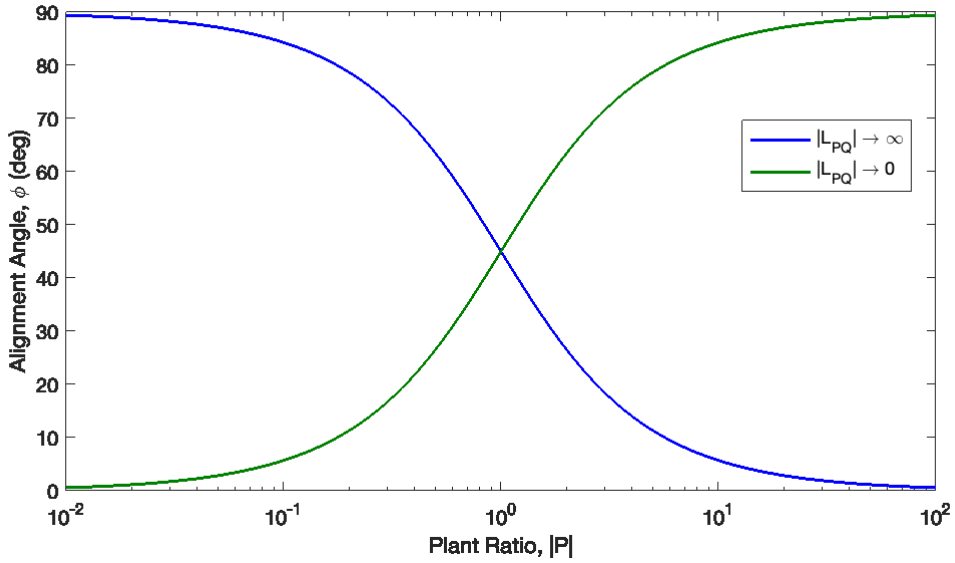

Figure 5.5: Alignment versus plant ratio for large and small $|L_{PQ}|$

dictated by

$$\phi = \arccos\left[\left(\left(2 + |P|^2 + |P^{-1}|^2\right)\left(\frac{0.5}{\cos(0.5\angle L_{PQ})}\right)^2\right)^{-\frac{1}{2}}\right] \tag{5.24}$$

The plot of Eq. (5.24) is shown in Fig. 5.6 for varying values of $\angle L_{PQ}$. Note that the alignment angle is minimized when $|P| = \left|\frac{g_1}{g_2}\right| = 1$. This indicates that the nominal crossover of $|L_{PQ}| = 1$ should roughly coincide with the natural crossover of $|P| = 1$, and that significant deviations will cause poor alignment at the handoff frequency.

5.3 Chapter Summary

This chapter presented a new controller design approach, based on the PQ method [24], which explicitly incorporates knowledge of alignment into the design process. This is accomplished by providing graphical information about the alignment angle on the Bode plot of the PQ frequency response. Because the approach is based on the PQ method, it shares many of the same advantages. The PQ method is a straightforward, intuitive approach for the design of compensators for TISO systems. It simplifies the TISO control design into two individual SISO design problems and provides a systematic way to balance relative contribution of coarse/fine actuators over frequency,

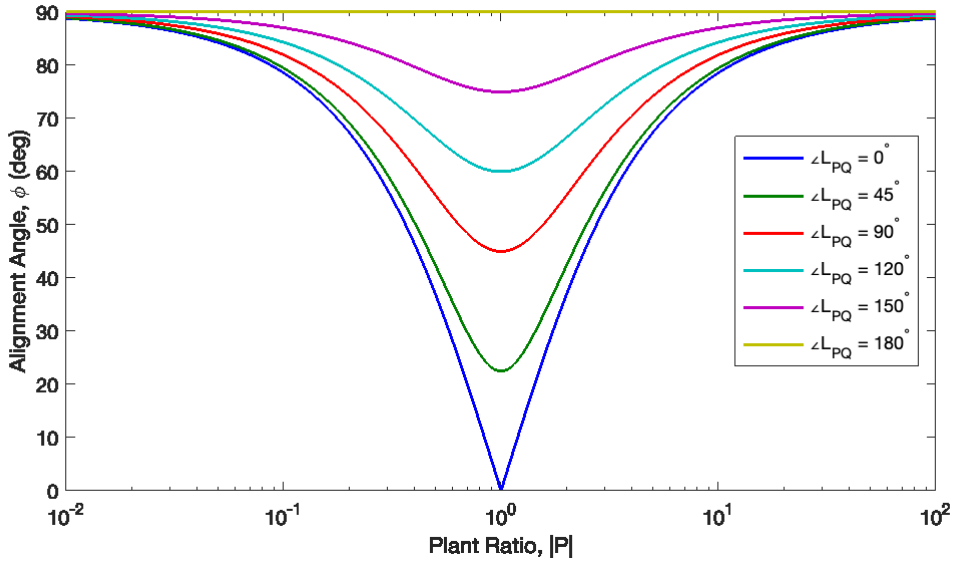

Figure 5.6: Alignment versus plant ratio at handoff, $|L_{PQ}| = 1$

and explicitly accounts for stability of zeros and destructive interference.

Unlike MIMO control design techniques, a disadvantage of the PQ method is that it does not explicitly take into account closed-loop performance at the plant input. This is a direct result of treating the TISO feedback problem as two separate SISO problems. Moreover, the PQ method provides no insight into system performance limitations with respect to plant/controller alignment. Although the selection of Q directly influences plant/controller alignment, the relationship between alignment and the PQ loop shape is nonintuitive.

To incorporate alignment into the PQ loop shaping process, a modification is made to the conventional Bode plot by adding magnitude and phase contours which represent specific values of the plant/controller alignment angle over frequency. The intersection of the PQ magnitude and phase responses with these contours indicate frequencies at which the alignment angle reaches a particular value. This allows the designer to easily determine the alignment over frequency for a given PQ loop shape. More importantly, the contours provide additional guidelines in the loop shaping process. The utility of this approach is highlighted through its application to the hybrid flexure bearing in the following chapter.

Chapter 6

Case Studies

This chapter presents two different case studies using the concepts built from previous chapters. The first case study, presented in Section 6.1, applies the concepts of plant/controller alignment to the control design of the hybrid flexure bearing using relative position feedback. A design example shows the utility of the graphical control design approach using alignment contours developed in Chapter 5. Two different control designs are compared: a controller that is poorly aligned with the plant, and a controller that is well aligned with the plant. The relative tracking performance of both designs are evaluated and experimentally validated. The second case study, presented in Section 6.2, applies the concepts of plant/controller alignment to the control design of the hybrid flexure bearing using inertial rate feedback for LOS stabilization applications. Two controller designs with different degrees of alignment are developed and applied to the inertial stabilization feedback configuration. Model-based friction compensation techniques are investigated using the data-based dynamic friction model developed in Chapter 3. The pointing performance of each controller design is evaluated in simulation and validated with the experimental testbed under a variety of base motion disturbances. A summary of the chapter is given in Section 6.3.

6.1 Case Study 1: Relative Position Feedback

This section applies the concepts of plant/controller alignment to the control design of the hybrid flexure bearing using relative position feedback. Figure 2.4 depicts the relative test configuration used in this case study. The relative test configuration was described in greater detail in Section 2.3.1.

6.1.1 System model

Neglecting nonlinearities due to bearing friction, the hybrid flexure bearing can be modeled by the simplified two-mass system shown in Fig. 6.1, where u_1 and u_2 represent the coarse and fine motor torque inputs, y is the LOS angle measured by the encoder, J_1 is the inertia of the outer axis, J_2 is the inertia of the inner axis, b_f is the viscous bearing friction, and k and b are the flexure stiffness and damping, respectively.

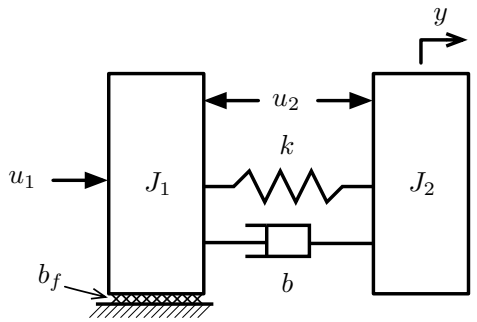

Figure 6.1: Simplified 2-DOF model

Starting with the transfer function derived in Eq. (3.18), the TISO plant model can be expressed as $G(s) = \begin{bmatrix} g_1(s) & g_2(s) \end{bmatrix}$ with

$$\begin{aligned} g_1(s) = \frac{Y(s)}{U_1(s)} &= \frac{\frac{b}{J_1 J_2}\left(s + \frac{k}{b}\right)}{s^2\left(s^2 + \frac{b}{J_{\text{eff}}}s + \frac{k}{J_{\text{eff}}}\right) + \frac{b_f}{J_1}s\left(s^2 + \frac{b}{J_2}s + \frac{k}{J_2}\right)} \\ &= \frac{K_1(s + z_1)}{s\left(s + p\right)\left(s^2 + 2\zeta_p\omega_p s + \omega_p^2\right)} \end{aligned} \tag{6.1}$$

$$\begin{aligned} g_2(s) = \frac{Y(s)}{U_2(s)} &= \frac{\frac{1}{J_2}s\left(s + \frac{b_f}{J_1}\right)}{s^2\left(s^2 + \frac{b}{J_{\text{eff}}}s + \frac{k}{J_{\text{eff}}}\right) + \frac{b_f}{J_1}s\left(s^2 + \frac{b}{J_2}s + \frac{k}{J_2}\right)} \\ &= \frac{K_2\left(s + z_2\right)}{\left(s + p\right)\left(s^2 + 2\zeta_p\omega_p s + \omega_p^2\right)} \end{aligned} \tag{6.2}$$

where $J_{\text{eff}} = \frac{J_1 J_2}{J_1 + J_2}$. Using the nominal model parameter values given in Table 6.1, the transfer

function gains, zero/pole locations, natural frequencies, and damping ratios are calculated as

$$K_1 = 3.234, \quad K_2 = 1.412,$$

$$z_1 = 2\pi(3.46 \times 10^3), \quad z_2 = 2\pi(6.03),$$

$$p = 2\pi(2.58), \quad \omega_p = 2\pi(46.8), \quad \zeta_p = 0.0435$$

Table 6.1: Model parameters for the relative test configuration

Parameter	**Symbol**	**Value**	**Units**
Flexure stiffness	k	26300	in-oz/rad
Flexure damping coefficient	b	1.21	in-oz-s/rad
Viscous bearing friction	b_f	20	in-oz-s/rad
Outer axis moment of inertia	J_1	0.528	in-oz-s^2
Inner axis moment of inertia	J_2	0.708	in-oz-s^2

The plant transfer functions are compared to measured frequency response data in Fig. 6.2. Overall, the plant model agrees well with the experimental results. Model discrepancies for $g_1(s)$ at higher frequencies (i.e, above 200 Hz) are due to unmodeled flexible dynamics in the system. These flexible modes can be neglected because they are far outside the bandwidth of the system.

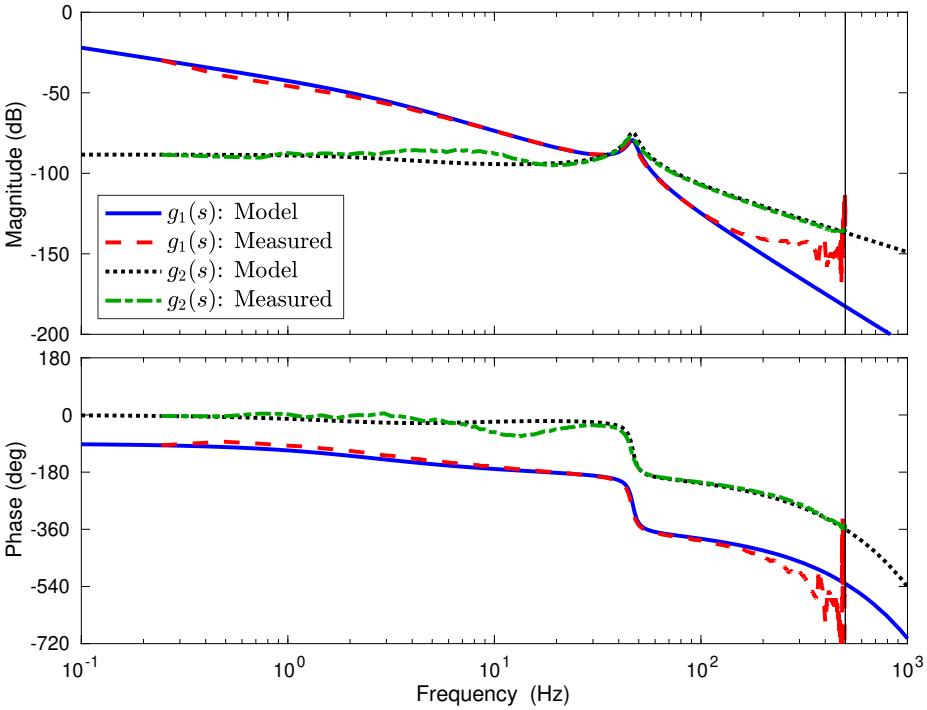

Figure 6.2: Plant frequency responses

6.1.2 Pre-compensator design: Actuator allocation using alignment contours

As outlined in Section 5.2.1, the first step of the PQ method involves the selection of the pre-compensators, $c_1'(s)$ and $c_2'(s)$, to appropriately allocate the primary (coarse) and secondary (fine) actuators over frequency by shaping the PQ frequency response. We now show how the alignment contours can be used to assist with this step. For the TISO plant model defined by Eqs. (6.1) and (6.2), the plant ratio can be expressed as

$$P(s) = \frac{g_1(s)}{g_2(s)} = \frac{K(s+z_1)}{s\,(s+z_2)} \tag{6.3}$$

where $K = K_1/K_2$. We can observe the plant's alignment to a unity controller, $C(s) = \begin{bmatrix} 1 & 1 \end{bmatrix}^T$, by selecting $Q(s) = \frac{c_1(s)}{c_2(s)} = 1$. Figure 6.3 shows the Bode plot of PQ with alignment contours drawn for $\phi \in [0°, 90°]$ in $10°$ intervals. The intersections of the magnitude and phase curves with each contour indicate the value of the plant/controller alignment angle at a particular frequency. This can be easily verified with the plot of alignment angle over frequency, using Eq. (4.9), on the bottom of Fig. 6.3. Note that the unity controller is not well aligned with the plant at any frequency ($\phi \geq 45° \; \forall \; \omega$), and is very poorly aligned ($\phi \approx 90°$) near 35 Hz.

The alignment contours represent the level sets of a three-dimensional surface which are viewed from above on the modified PQ Bode plot. The use of color mapped contour regions makes it is easier to distinguish the "peaks" and "valleys" of the surfaces which correspond to large and small alignment angles, respectively. These regions can be used as guidelines for shaping the PQ frequency response to achieve better alignment. As indicated in Fig. 6.3, it is desirable to target the darker regions where alignment is good ($\phi \approx 0°$) and avoid the lighter regions where alignment is poor ($\phi \approx 90°$). The graphical alignment contours provide valuable insight into the relationship between the PQ loop shape and the plant/controller alignment.

To illustrate the utility of the alignment contours, consider the two different PQ loop shapes shown in Figs. 6.4 and 6.5, both of which satisfy the requirements outlined in Sec. 5.2.1, but have significantly different degrees of plant/controller alignment over frequency. For the sake of comparison, the first design, shown in Fig. 6.4, is intentionally shaped to yield poor alignment over a wide frequency range. This is accomplished by using a double lead compensator centered

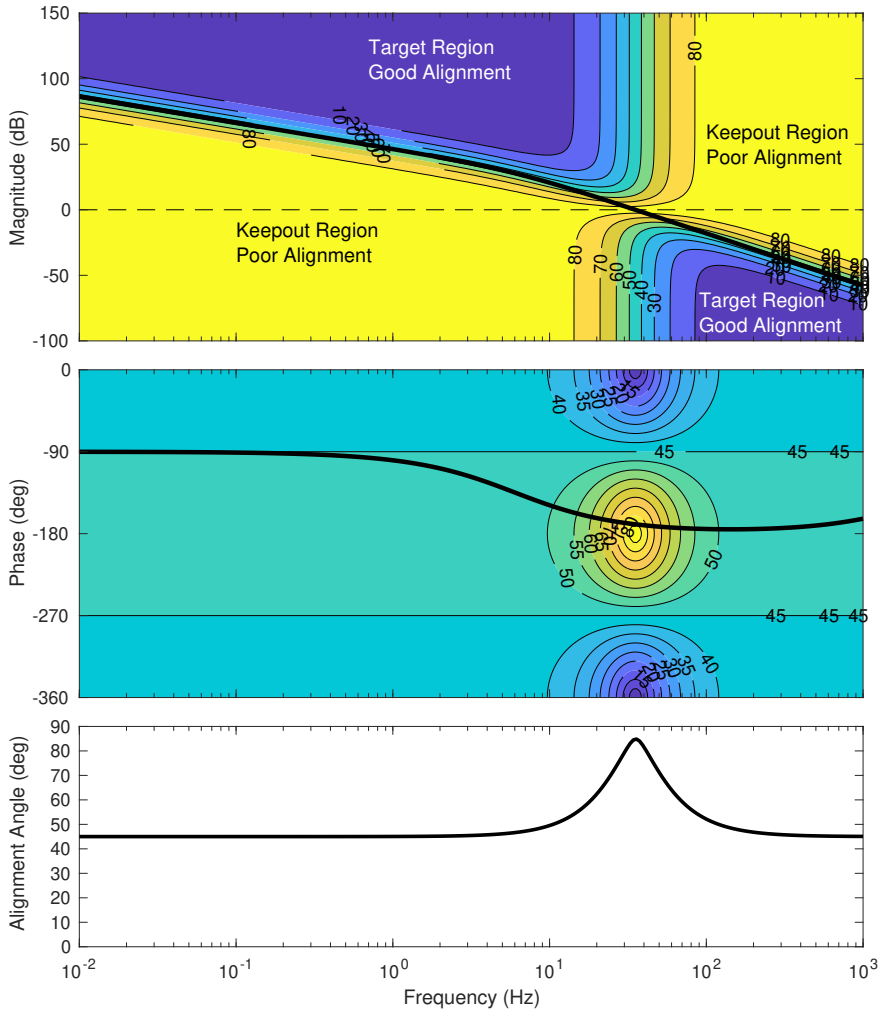

Figure 6.3: PQ Bode plot with alignment contours for $Q = 1$

about 35 Hz. Although alignment is improved near 35 Hz due to the additional phase lead, the corresponding shift in gain causes the magnitude and phase responses to enter the lighter keepout regions. We can see from the magnitude contours that this is due to inadequate low frequency gain and excessive high frequency gain, resulting in very poor alignment over a large frequency range. According to the results of Sec. 4.2, we expect large input sensitivities and closed-loop interactions for Design #1.

The second design example, shown in Fig. 6.5, is shaped to improve the overall plant/controller alignment. This is accomplished with simple compensation techniques to shape the PQ frequency response using the graphical alignment contours as guidelines. An integrator + zero is used to boost the low frequency gain while avoiding additional phase lag at higher frequencies. The integral action

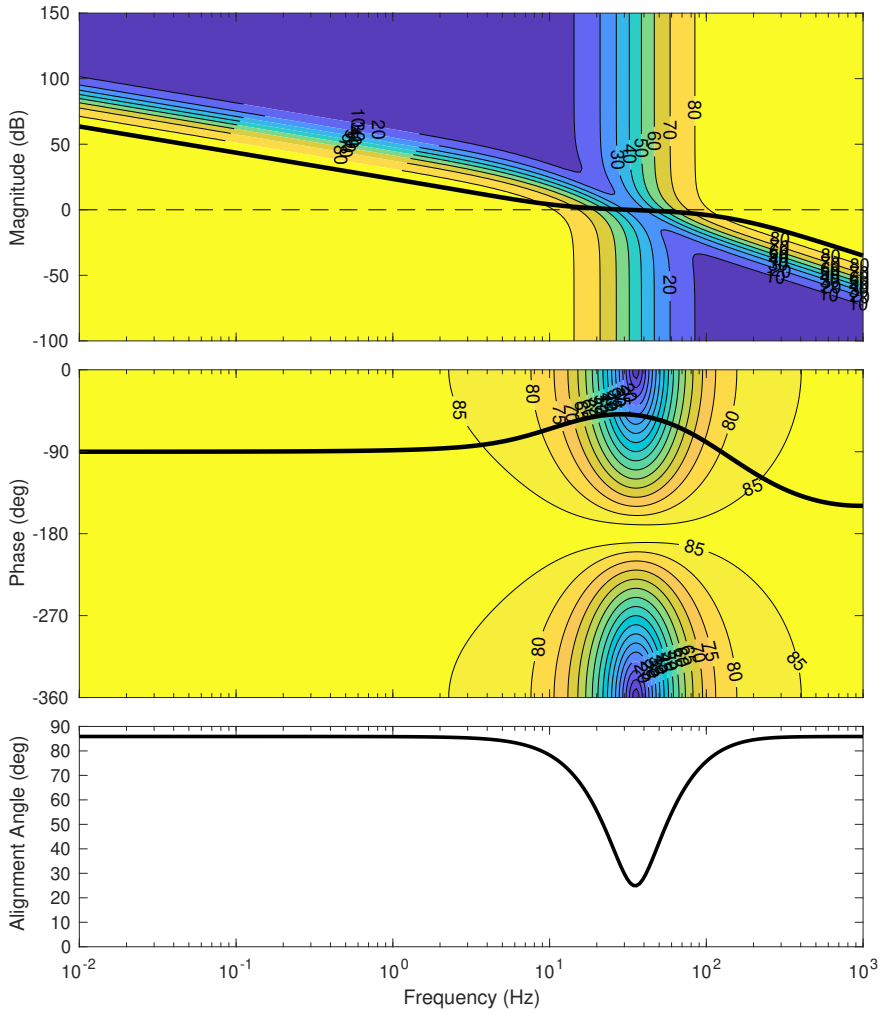

Figure 6.4: PQ Bode plot for Design #1

bends the magnitude response upward into the darker target region which significantly improves the alignment angle at lower frequencies. A low pass filter provides high frequency roll-off to steer the magnitude response downward into the lower target region which improves alignment at higher frequencies. To satisfy the conditions given in Sec. 5.2.1, lead compensation is used near the crossover to achieve a phase margin of 60°. Although Design #2 is well aligned at both low and high frequencies, it is not possible to maintain such good alignment over the entire frequency range. This is due to the inherent tradeoff between the alignment angle and phase margin at hand-off. As indicated by the magnitude contours, alignment can be improved with a steeper magnitude response near the crossover. However, due to the Bode gain-phase relationship [123], this comes at the expense of reduced phase margin. Since adequate phase margin is required to avoid destructive

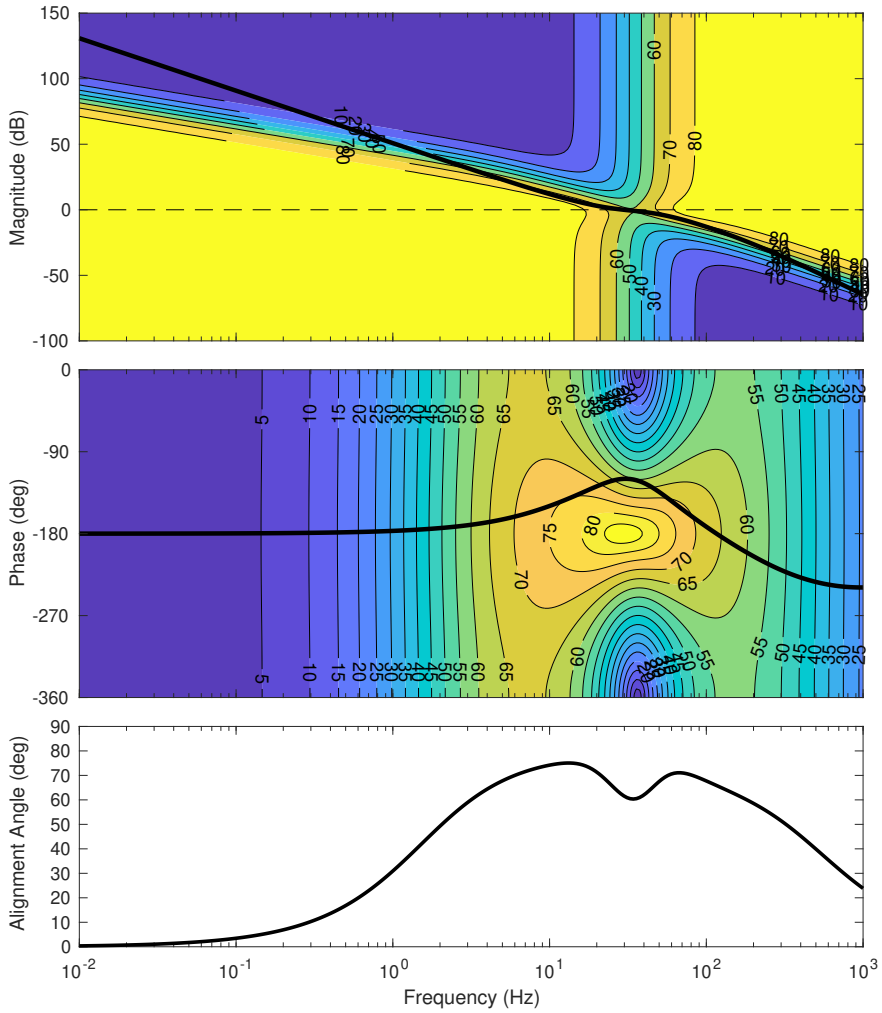

Figure 6.5: PQ Bode plot for Design #2

interference and NMP zeros, the alignment angle must necessarily increase in the hand-off region. The alignment contours make these tradeoffs clear.

The controller ratios that achieve the PQ loop shapes for the two different designs shown in Figs. 6.4 and 6.5 are

$$Q_1(s) = \frac{13.928\,(s+60.27)^2}{(s+839.5)^2} \tag{6.4}$$

$$Q_2(s) = \frac{2834.4\,(s+94.25)\,(s+39.88)\left(s^2+237.1s+2.87\times10^4\right)}{s\,(s+1283)\,(s+314.2)\left(s^2+377.2s+7.26\times10^4\right)} \tag{6.5}$$

After shaping Q as described above, it is straightforward to select the pre-compensators c_1' and c_2' through the relationship defined in Eq. (5.3). Since Q is realizable, a reasonable choice is

to select $c_1' = Q$ and $c_2' = 1$. Figure 6.6 shows the Bode plot of $G_{\text{SISO}} = c_1' g_1 + c_2' g_2$ for the two designs.

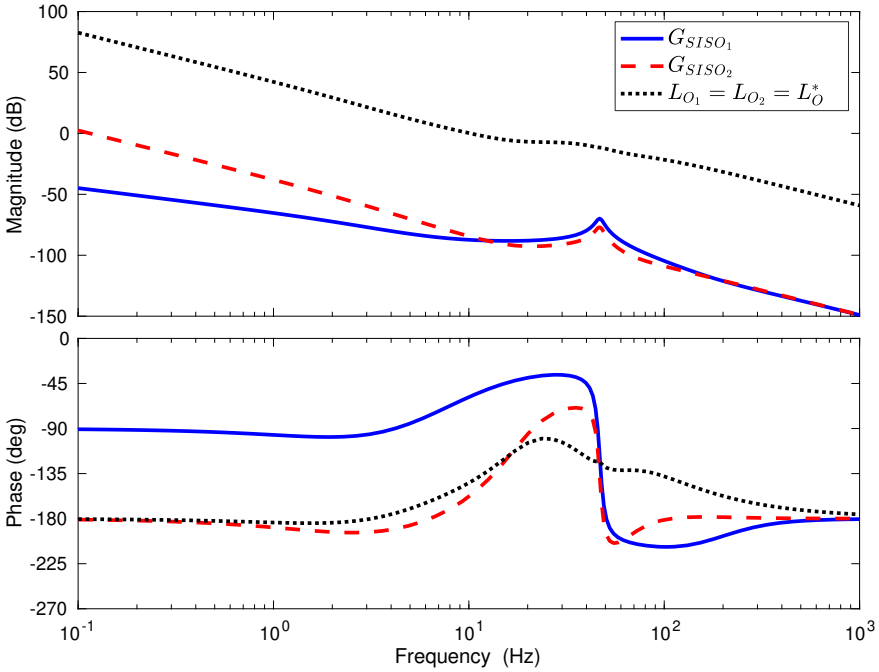

Figure 6.6: Bode plot of G_{SISO} and L_O

6.1.3 Post-compensator design: Output equivalent controllers

The second step of the PQ method involves the selection of the post-compensator, $c_0(s)$, to satisfy stability and performance requirements. In order to make fair comparisons of closed-loop performance, we must choose the post-compensators for the two designs such that they achieve identical output responses. This ensures that any differences in closed-loop performance at the plant input can be solely attributed to differences in plant/controller alignment.

Because the TISO plant G, defined in Eq. (4.1), has a non-trivial right nullspace, it follows that there are many choices of the controller C that yield the same fixed set of output transfer functions [90], denoted as L_O^*, S_O^*, and T_O^*. This set of controllers is defined as

$$\mathcal{C}(L_O^*(j\omega)) \coloneqq \{C(j\omega) : G(j\omega)C(j\omega) = L_O^*(j\omega)\} \tag{6.6}$$

where any $C(j\omega) \in \mathcal{C}(L_O^*(j\omega))$ is called an *output equivalent controller* [90].

Let C_1 and C_2 be the controllers for Design #1 and Design #2, respectively. To obtain output equivalent controllers such that $C_1, C_2 \in \mathcal{C}(L_O^*)$, we first select the post-compensator for Design #2 to achieve a crossover frequency of 10 Hz with a phase margin of 35° and a gain margin of at least 6 dB. This is achieved with a cascaded lead compensator and notch filter given by

$$c_{0_2} = \frac{30801\,(s+36.28)\left(s^2+25.92s+8.61\times10^4\right)}{(s+108.8)\,(s^2+410.8s+8.61\times10^4)} \tag{6.7}$$

Figure 6.6 shows the Bode plot of $L_{O_2} = GC_2 = c_{0_2}G_{\mathrm{SISO}_2}$. To ensure that $C_1 \in \mathcal{C}(L_O^*)$ such that $GC_1 = GC_2 = L_O^*$, the post-compensator for Design #1 must satisfy

$$c_{0_1} = \frac{L_O^*}{G_{\mathrm{SISO}_1}} \tag{6.8}$$

6.1.4 Analysis and simulated results

Figure 6.7 compares $\|T_I\|$ and $\|S_IC\|$ for the two designs obtained in the previous section. The plots of $|T_O|$ and $|T_O|/\|G\|$ are also included, which represent the minimum possible value of $\|T_I\|$ and $\|S_IC\|$ in the case of perfect alignment according to Eqs. (4.23) and (4.24), respectively. Note that $|T_O|$ and $|T_O|/\|G\|$ are identical for both designs through the use of output equivalent controllers.

Figure 6.7(a) shows the plot of $\|T_I\|$ for Design #1. We see that $\|T_I\|$ has a large DC gain, which is due to the poor plant/controller alignment at low frequency. This will ultimately result in a large closed-loop response to input disturbances. On the other hand, we see that $\|T_I\|$ has a unity DC gain for Design #2 shown in Fig. 6.7(b). This is a direct result of the nearly perfect alignment achieved at low frequencies in Design #2. To illustrate the effect of alignment on the closed-loop interactions at the plant input, we compare the DC gain matrix, $T_I(0)$, for each design:

$$\text{Design \#1:}\quad T_I(0) = \begin{bmatrix} 1 & 0 \\ 13.9 & 0 \end{bmatrix}$$

$$\text{Design \#2:}\quad T_I(0) = \begin{bmatrix} 1 & 0 \\ 0 & 0 \end{bmatrix}$$

Due to poor low frequency alignment, Design #1 produces a large off-diagonal term creating a significant one-way interaction between $d_{i1} \to u_2$ at the plant input. On the other hand, Design #2

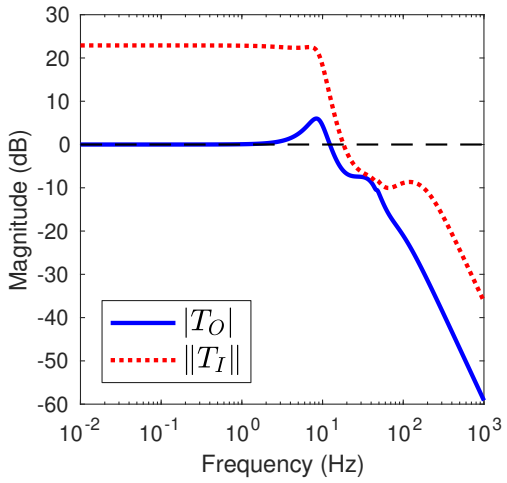

(a) $\|T_I\|$ for Design #1

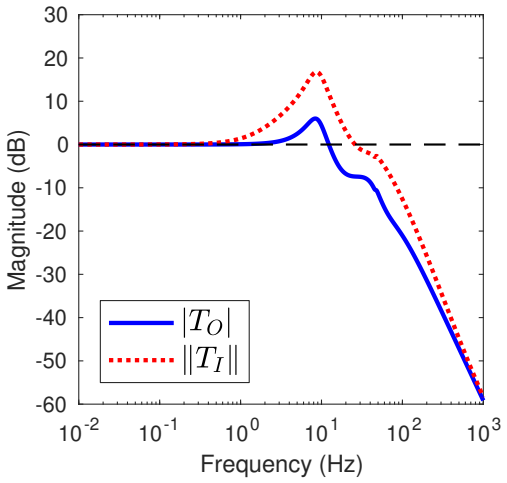

(b) $\|T_I\|$ for Design #2

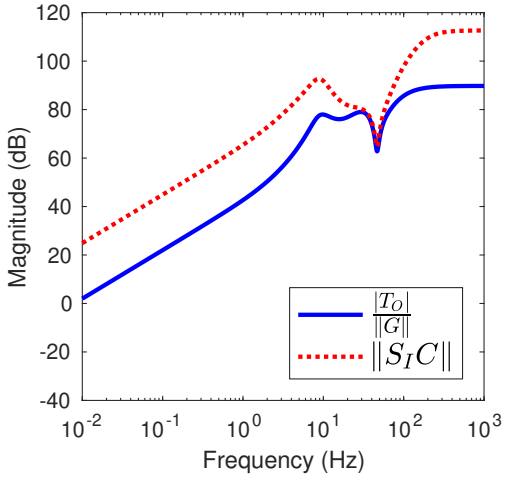

(c) $\|S_I C\|$ for Design #1

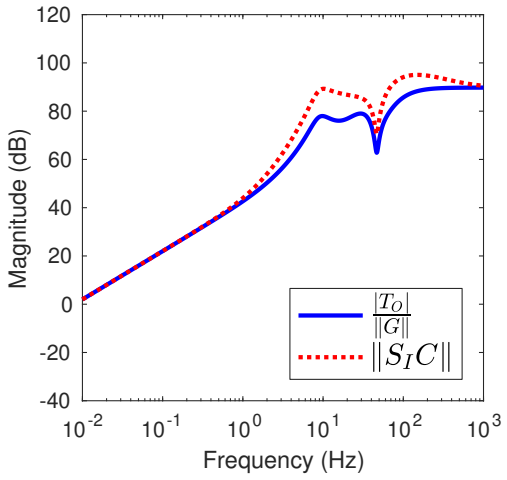

(d) $\|S_I C\|$ for Design #2

Figure 6.7: Comparison of input sensitivities

produces no interactions due to perfect alignment at $\omega = 0$.

The simulated closed-loop responses to a step input disturbance, $D_I = \begin{bmatrix} 5 & 0 \end{bmatrix}^T$, are compared in Fig. 6.8. Note that the output response, y, for each design is identical due to the use of output equivalent controllers. However, the input responses, u_1 and u_2, are drastically different. As shown in Fig. 6.8(a), Design #1 produces a large control response on the second controller output, u_2. This is undesirable in practice since the saturation limits of the secondary actuator are typically much smaller than the primary actuator. Indeed, Design #1 exceeds the saturation limits of the VCMs, which only provide a maximum torque capability of 16.1 in-oz. As shown in Fig. 6.8(b), Design #2 produces a well-behaved control response which avoids actuator saturation. This is due

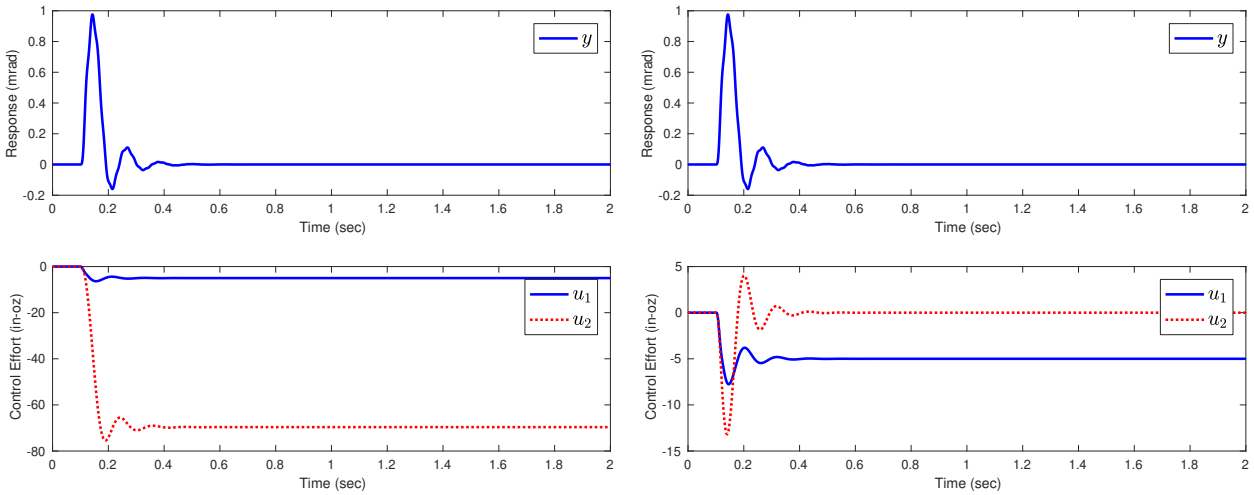

(a) Input disturbance response for Design #1

(b) Input disturbance response for Design #2

Figure 6.8: Comparison of input disturbance responses

to the improved alignment at low frequency, hence smaller $\|T_I\|$ and reduced interactions.

Similarly, the effects of alignment on $\|S_I C\|$ for the two different designs are shown in Figs. 6.7(c) and 6.7(d). We see that elevated values of $\|S_I C\|$ occur at frequencies where alignment is poor. Design #1 produces large $\|S_I C\|$ over a wide frequency range where alignment is poor. Design #2 overall reduces $\|S_I C\|$ where alignment is improved. The simulated closed-loop responses to reference step commands are compared in Fig. 6.9. Although the output response, y, for each design is identical, the input responses, u_1 and u_2, are again quite different. As shown in Fig. 6.9(a), Design #1 exhibits a very large transient response on the primary actuator. In this case, u_1 exceeds the BLDC motor's maximum torque capability of 81.3 in-oz. This large transient is due to poor alignment at high frequency which forces $\|S_I C\|$ to be large. As shown in Fig. 6.9(b), Design #2 reduces the control transients and avoids actuator saturation as a result of the improved alignment at high frequency.

6.1.5 Experimental validation

The two controller designs were discretized using the bilinear (Tustin) approximation and implemented on the experimental testbed shown in Fig. 2.4. Figure 6.10 compares the experimental step responses for the two designs. Due to friction, the measured responses are more highly damped than the ideal linear responses depicted in Fig. 6.9. Thus, the measured responses are compared

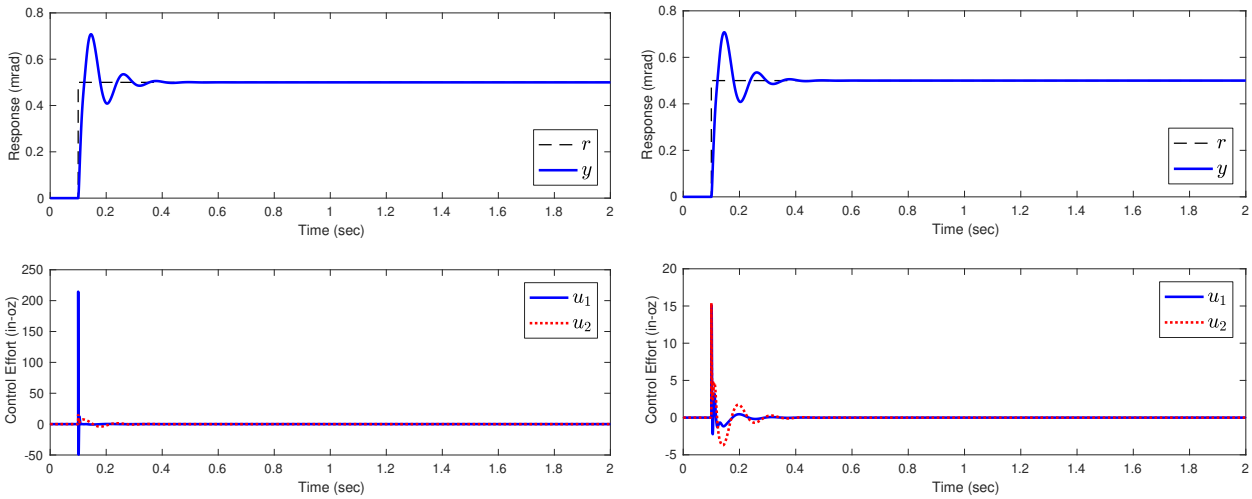

(a) Step response for Design #1

(b) Step response for Design #2

Figure 6.9: Comparison of step responses

with results obtained from the higher fidelity nonlinear model discussed in Chapter 3, which includes actuator saturation and dynamic friction. The simulated responses are in good agreement with the experimental results. As shown in Fig. 6.10(a), the poor alignment of Design #1 causes a large transient response on the primary actuator and causes it to saturate. The improved alignment of Design #2 reduces the transient response so that neither actuator saturates, as shown in Fig. 6.10(b).

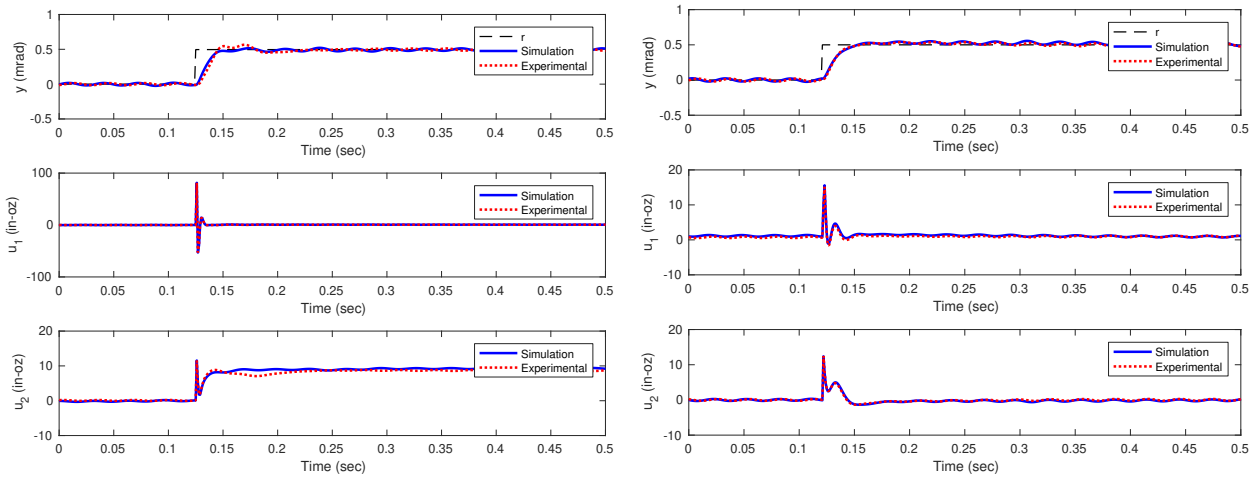

(a) Experimental step response for Design #1

(b) Experimental step response for Design #2

Figure 6.10: Comparison of simulated and experimental step responses

6.2 Case Study 2: Inertial Stabilization

This section applies the concepts of plant/controller alignment to the control design of the hybrid flexure bearing using inertial rate feedback for LOS stabilization. Section 2.3.2 describes the inertial test configuration and Fig. 2.5 depicts the testbed hardware developed for this effort. The inertial stabilization system, depicted in Fig. 6.11, utilizes a cascade feedback control architecture. A high-bandwidth inner rate feedback loop is used to inertially stabilize the LOS and reject base disturbances. A lower bandwidth outer position loop is used for pointing control. The controller design is broken up into two steps by using successive loop closure. First, the inner rate loop controller is designed using the TISO control design approach described in Chapter 5. Then, the inner loop is closed and the outer loop controller is designed to achieve the desired closed-loop performance specifications. In the previous case study, the sensor dynamics were ignored since the encoders are high-bandwidth devices with extremely low latency. In this case study, a model of the gyro must be included in the feedback loop as its dynamics (and delay) significantly impact the achievable bandwidth in the system.

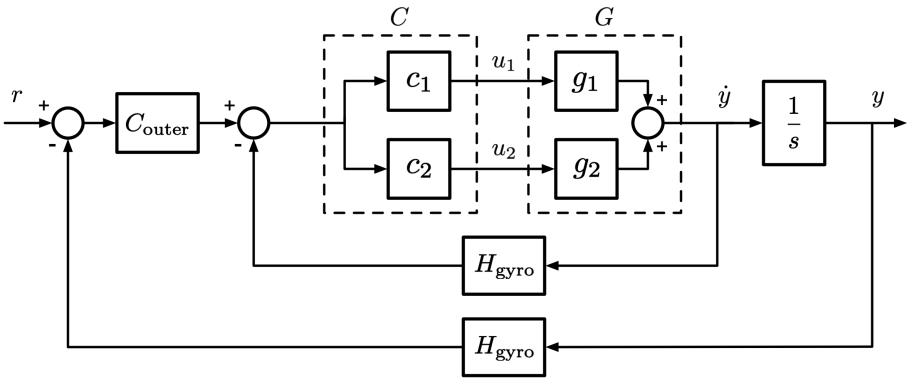

Figure 6.11: Inertial stabilization feedback configuration

6.2.1 System model

Neglecting nonlinearities due to bearing friction, the hybrid flexure bearing can be modeled by the simplified two-mass system depicted in Fig. 6.1, where u_1 and u_2 represent the coarse and fine motor torque inputs, $\dot{y}$ is the LOS rate, y is the LOS angle, J_1 is the inertia of the outer axis, J_2 is the inertia of the inner axis, b_f is the viscous bearing friction, and k and b are the flexure stiffness

and damping, respectively. The TISO plant model for the inertial configuration is similar to the plant model defined by Eqs. (6.1) and (6.2), but differs by a single integrator since the output is the angular rate instead of angular position. The plant can be expressed as $G(s) = \begin{bmatrix} g_1(s) & g_2(s) \end{bmatrix}$ with

$$\begin{aligned} g_1(s) = \frac{\dot{Y}(s)}{U_1(s)} &= \frac{\frac{b}{J_1 J_2}\left(s + \frac{k}{b}\right)}{s\left(s^2 + \frac{b}{J_{\text{eff}}}s + \frac{k}{J_{\text{eff}}}\right) + \frac{b_f}{J_1}\left(s^2 + \frac{b}{J_2}s + \frac{k}{J_2}\right)} \\ &= \frac{K_1(s + z_1)}{(s+p)\left(s^2 + 2\zeta_p\omega_p s + \omega_p^2\right)} \end{aligned} \tag{6.9}$$

$$\begin{aligned} g_2(s) = \frac{\dot{Y}(s)}{U_2(s)} &= \frac{\frac{1}{J_2}s\left(s + \frac{b_f}{J_1}\right)}{s\left(s^2 + \frac{b}{J_{\text{eff}}}s + \frac{k}{J_{\text{eff}}}\right) + \frac{b_f}{J_1}\left(s^2 + \frac{b}{J_2}s + \frac{k}{J_2}\right)} \\ &= \frac{K_2 s\,(s + z_2)}{(s+p)\left(s^2 + 2\zeta_p\omega_p s + \omega_p^2\right)} \end{aligned} \tag{6.10}$$

where $J_{\text{eff}} = \frac{J_1 J_2}{J_1 + J_2}$. Note that some of the model parameters for the inertial test configuration are different from those used for the relative test configuration in Section 6.1. The changes in inertia values reflect the additional mass of the IMU and mirror which are mounted to the LOS axis. To offset the change in inertia on the inner axis, additional inertia was also added to the outer axis to achieve a reasonable natural handoff frequency. Additionally, the flexure stiffness value decreased slightly as a result of internal heating caused by the IMU. Using the updated model parameter values listed in Table 6.2, the transfer function gains, zero/pole locations, natural frequencies, and damping ratios are calculated as

$$K_1 = 0.248, \quad K_2 = 0.559,$$

$$z_1 = 2\pi(2.81 \times 10^3), \quad z_2 = 2\pi(1.17),$$

$$p = 2\pi(0.705), \quad \omega_p = 2\pi(22.4), \quad \zeta_p = 0.0143$$

The gyro model can be expressed as a second-order transfer function with a pure time delay

$$H_{\text{gyro}}(s) = \frac{\omega_g^2}{s^2 + 2\zeta_g\omega_g s + \omega_g^2}\, e^{-sT_d} \tag{6.11}$$

where ω_g is the gyro bandwidth, ζ_g is the gyro damping ratio, and T_d is the gyro delay. It

is important to include the gyro delay in the model as it fundamentally limits the achievable bandwidth of the inner rate loop. The gyro model parameter values are listed in Table 6.2.

The plant transfer functions (including gyro dynamics) are compared to measured frequency response data in Fig. 6.12. Overall, the plant model agrees well with the experimental results. Model discrepancies at higher frequencies (i.e, above 150 Hz) are due to unmodeled flexible dynamics in the system. These flexible modes can be neglected because they are far outside the bandwidth of the system.

Table 6.2: Model parameters for the inertial test configuration

Parameter	**Symbol**	**Value**	**Units**
Flexure stiffness	k	21370	in-oz/rad
Flexure damping coefficient	b	1.21	in-oz-s/rad
Viscous bearing friction	b_f	20	in-oz-s/rad
Outer axis moment of inertia	J_1	2.73	in-oz-s^2
Inner axis moment of inertia	J_2	1.79	in-oz-s^2
Gyro bandwidth	ω_g	$2\pi(150)$	rad/s
Gyro damping ratio	ζ_g	0.7	—
Gyro delay	T_d	2.6	ms

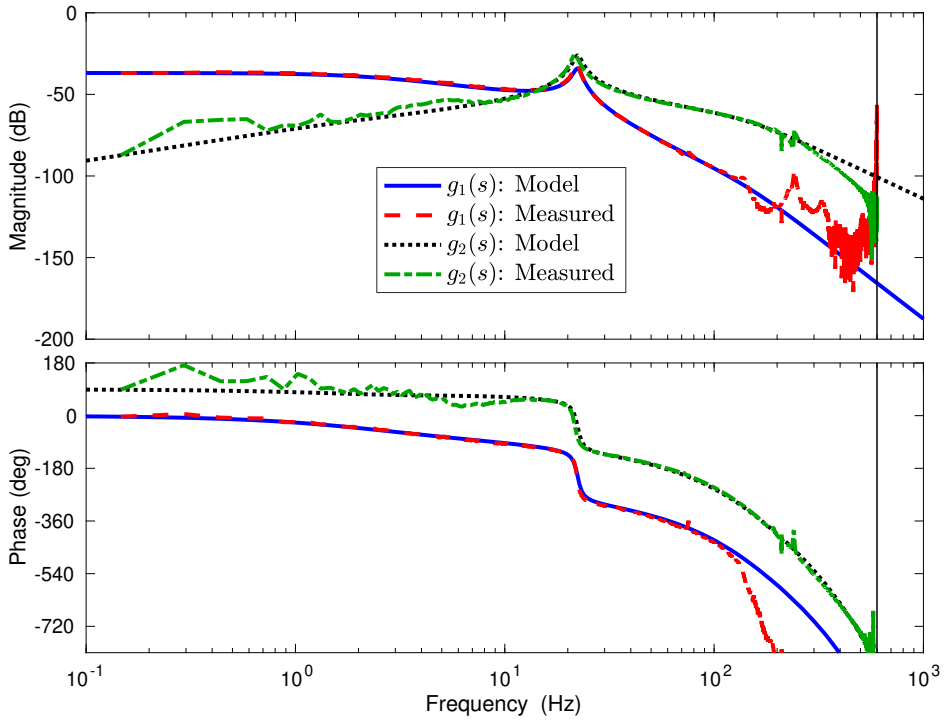

Figure 6.12: Plant frequency responses for the inertial test configuration

6.2.2 Control design

Pre-compensator design: Actuator allocation using alignment contours

As outlined in Section 5.2.1, the first step of the PQ method involves the selection of the pre-compensators, $c_1'(s)$ and $c_2'(s)$, to appropriately allocate the primary (coarse) and secondary (fine) actuators over frequency by shaping the PQ frequency response. We now show how the alignment contours can be used to assist with this step. For the TISO plant model defined by Eqs. (6.9) and (6.10), the plant ratio can be expressed as

$$P(s) = \frac{g_1(s)}{g_2(s)} = \frac{K(s+z_1)}{s\,(s+z_2)} \tag{6.12}$$

where $K = K_1/K_2$. We can observe the plant's alignment to a unity controller, $C(s) = \begin{bmatrix} 1 & 1 \end{bmatrix}^T$, by selecting $Q(s) = \frac{c_1(s)}{c_2(s)} = 1$. Figure 6.13 shows the Bode plot of PQ with alignment contours drawn for $\phi \in [0°, 90°]$ in $10°$ intervals. The intersections of the magnitude and phase curves with each contour indicate the value of the plant/controller alignment angle at a particular frequency. This can be easily verified with the plot of alignment angle over frequency, using Eq. (4.9), on the bottom of Fig. 6.13. Note that the unity controller is not well aligned with the plant at any frequency ($\phi \geq 45° \; \forall \; \omega$), and is very poorly aligned ($\phi \approx 90°$) near 14 Hz. The alignment contours represent the level sets of a three-dimensional surface which are viewed from above on the modified PQ Bode plot. The use of color mapped contour regions makes it is easier to distinguish the "peaks" and "valleys" of the surfaces which correspond to large and small alignment angles, respectively. These regions can be used as guidelines for shaping the PQ frequency response to achieve better alignment. As indicated in Fig. 6.13, it is desirable to target the darker regions where alignment is good ($\phi \approx 0°$) and avoid the lighter regions where alignment is poor ($\phi \approx 90°$). The graphical alignment contours provide valuable insight into the relationship between the PQ loop shape and the plant/controller alignment.

To illustrate the utility of the alignment contours, consider the two different PQ loop shapes shown in Figs. 6.14 and 6.15, both of which satisfy the requirements outlined in Sec. 5.2.1, but have significantly different degrees of plant/controller alignment over frequency. For the sake of comparison, the first design, shown in Fig. 6.14, is intentionally shaped to yield poor alignment

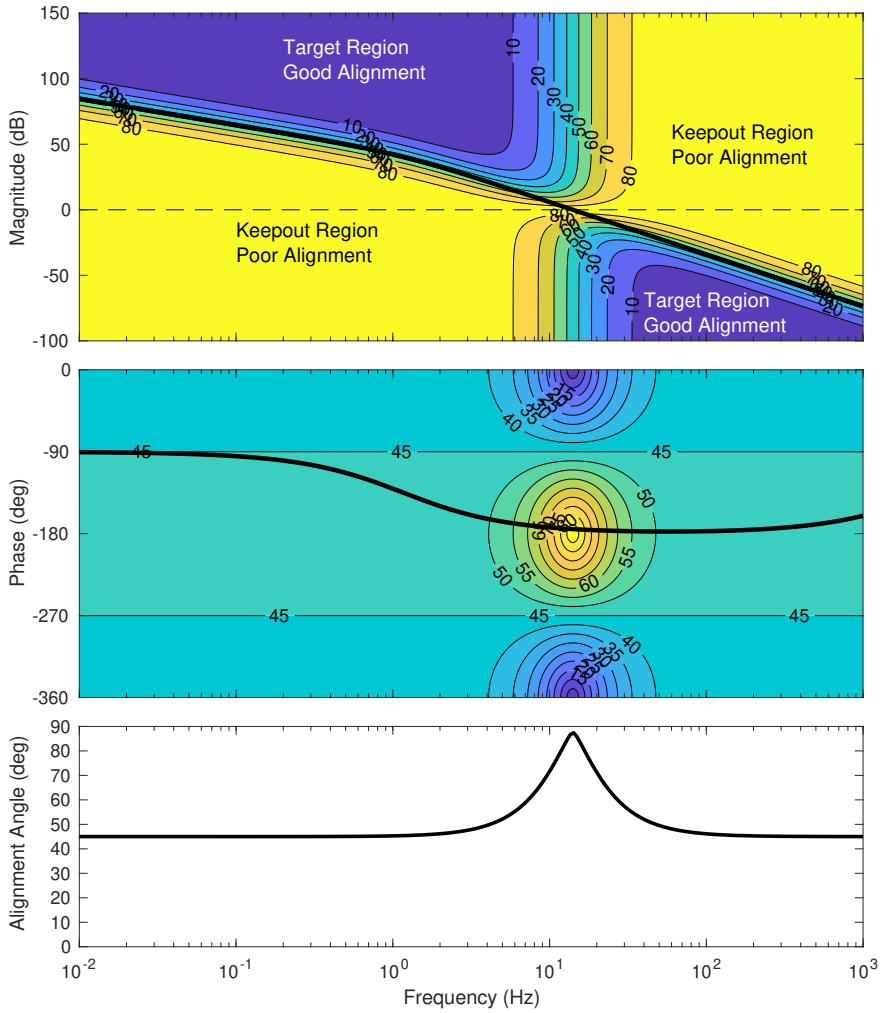

Figure 6.13: PQ Bode plot with alignment contours for $Q = 1$

over a wide frequency range. This is accomplished by using a double lead compensator centered about 10 Hz. Although alignment is improved near 14 Hz due to the additional phase lead, the corresponding shift in gain causes the magnitude and phase responses to enter the lighter keepout regions. We can see from the magnitude contours that this is due to inadequate low frequency gain and excessive high frequency gain, resulting in very poor alignment over a large frequency range. According to the results of Sec. 4.2, we expect large input sensitivities and closed-loop interactions for Design #1.

The second design example, shown in Fig. 6.15, is shaped to improve the overall plant/controller alignment. This is accomplished with simple compensation techniques to shape the PQ frequency response using the graphical alignment contours as guidelines. An integrator + zero is used to boost

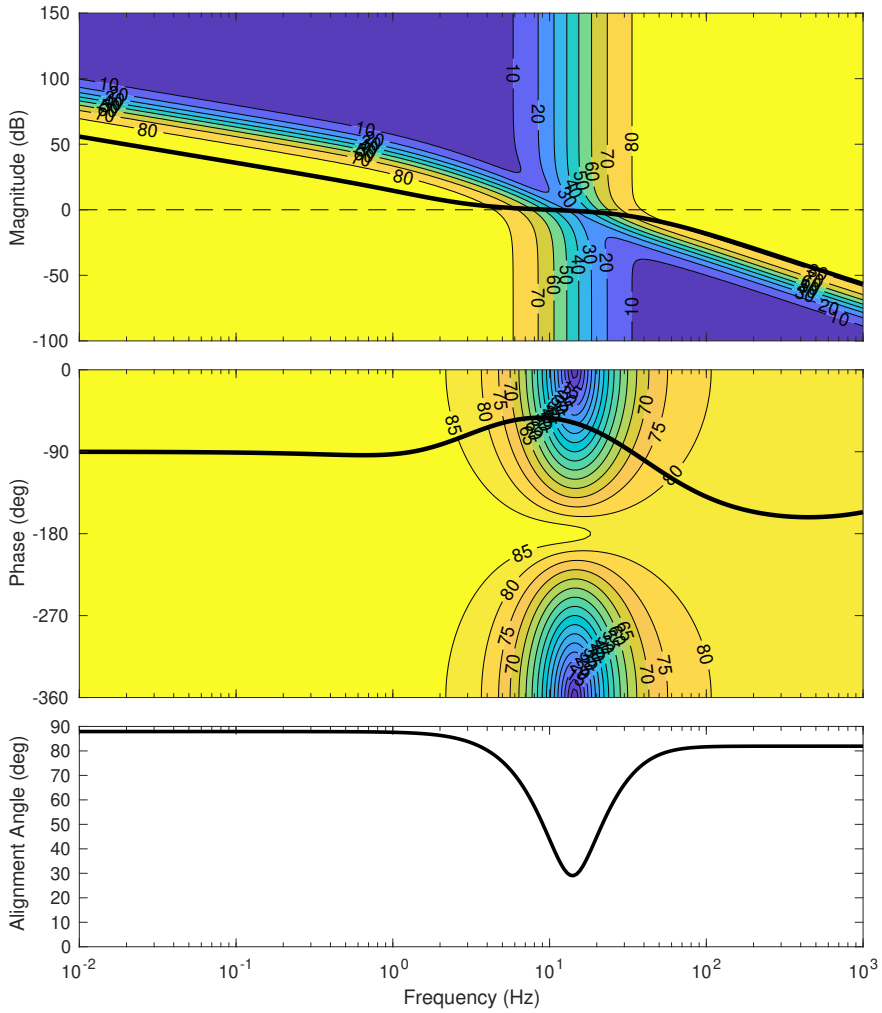

Figure 6.14: PQ Bode plot for Design #1

the low frequency gain while avoiding additional phase lag at higher frequencies. The integral action bends the magnitude response upward into the darker target region which significantly improves the alignment angle at lower frequencies. A low pass filter provides high frequency roll-off to steer the magnitude response downward into the lower target region which improves alignment at higher frequencies. To satisfy the conditions given in Sec. 5.2.1, lead compensation is used near the crossover to achieve a phase margin of 60°. Although Design #2 is well aligned at both low and high frequencies, it is not possible to maintain such good alignment over the entire frequency range. This is due to the inherent tradeoff between the alignment angle and phase margin at hand-off. As indicated by the magnitude contours, alignment can be improved with a steeper magnitude response near the crossover. However, due to the Bode gain-phase relationship [123], this comes at

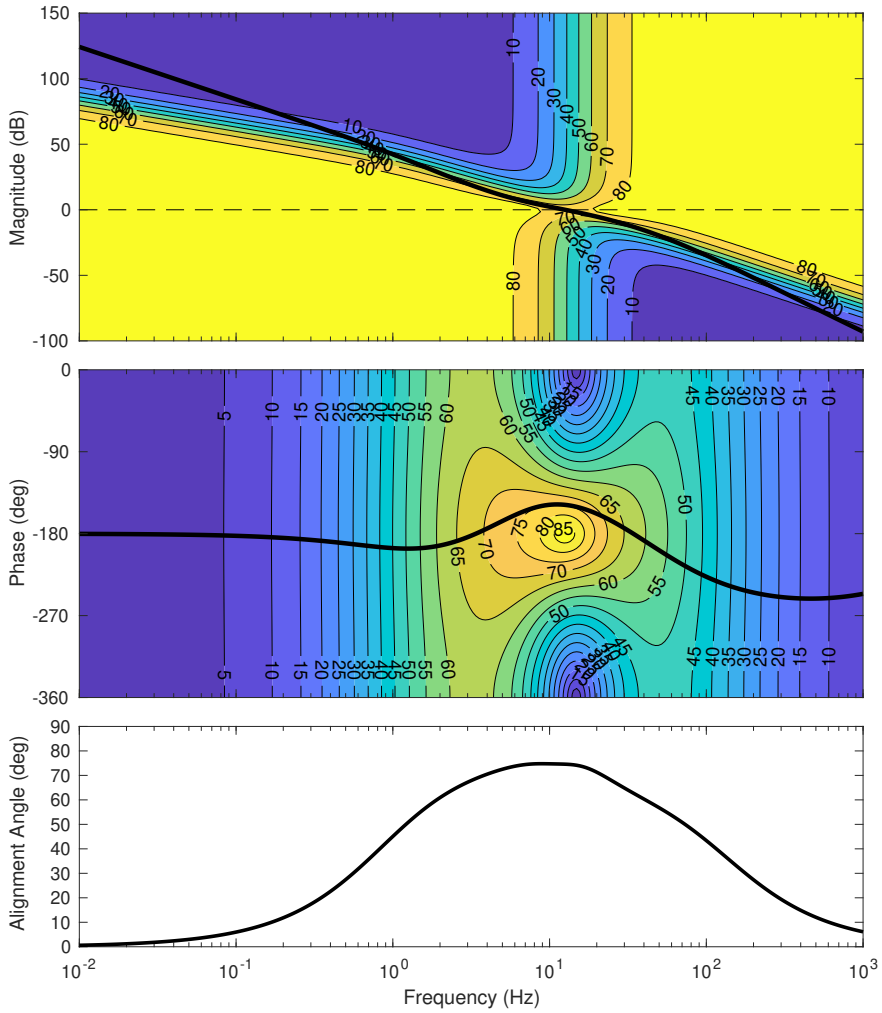

Figure 6.15: PQ Bode plot for Design #2

the expense of reduced phase margin. Since adequate phase margin is required to avoid destructive interference and NMP zeros, the alignment angle must necessarily increase in the hand-off region. The alignment contours make these tradeoffs clear.

The controller ratios that achieve the PQ loop shapes for the two different designs shown in Figs. 6.14 and 6.15 are

$$Q_1(s) = \frac{7.062\,(s+16.84)^2}{(s+234.5)^2} \tag{6.13}$$

$$Q_2(s) = \frac{674.3\,(s+50.27)\,(s+21.02)\left(s^2+85.53s+2258\right)}{s\,(s+314.2)\,(s+187.8)\,(s^2+121.1s+4529)} \tag{6.14}$$

After shaping Q as described above, it is straightforward to select the pre-compensators c_1'

and c_2' through the relationship defined in Eq. (5.3). Since Q is realizable, a reasonable choice is to select $c_1' = Q$ and $c_2' = 1$. Figure 6.16 shows the Bode plot of $G_{\text{SISO}} = c_1' g_1 + c_2' g_2$ for the two designs.

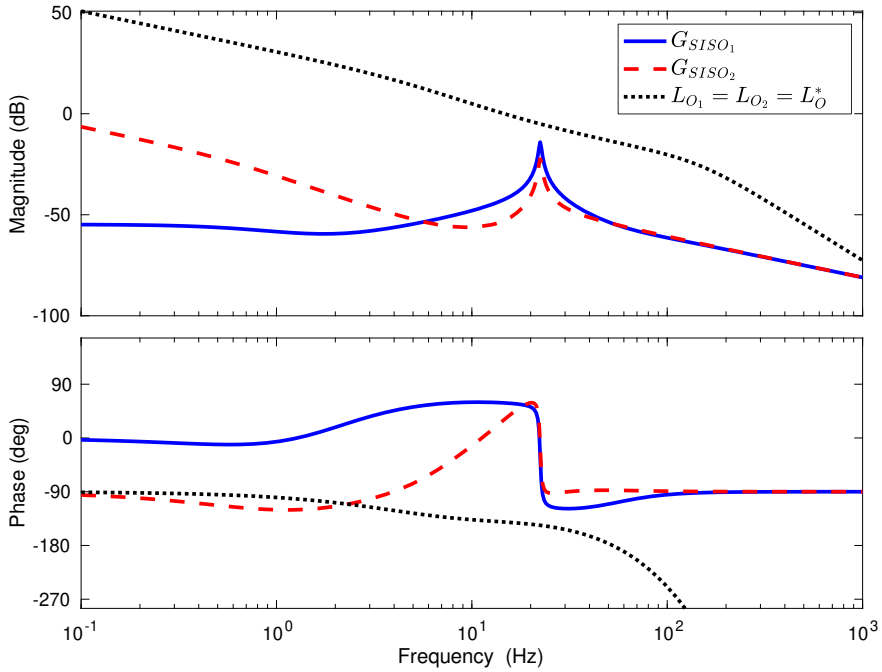

Figure 6.16: Bode plot of G_{SISO} and L_O

Post-compensator design: Output equivalent controllers

The second step of the PQ method involves the selection of the post-compensator, $c_0(s)$, to satisfy stability and performance requirements. In order to make fair comparisons of closed-loop performance, we must choose the post-compensators for the two designs such that they achieve identical output responses. This ensures that any differences in closed-loop performance at the plant input can be solely attributed to differences in plant/controller alignment.

Because the TISO plant G, defined in Eq. (4.1), has a non-trivial right nullspace, it follows that there are many choices of the controller C that yield the same fixed set of output transfer functions [90], denoted as L_O^*, S_O^*, and T_O^*. This set of controllers is defined as

$$\mathcal{C}(L_O^*(j\omega)) \coloneqq \{C(j\omega) : G(j\omega)C(j\omega) = L_O^*(j\omega)\} \tag{6.15}$$

where any $C(j\omega) \in \mathcal{C}(L_O^*(j\omega))$ is called an *output equivalent controller* [90].

Let C_1 and C_2 be the controllers for Design #1 and Design #2, respectively. To obtain output equivalent controllers such that $C_1, C_2 \in \mathcal{C}(L_O^*)$, we first select the post-compensator for Design #1 to achieve a crossover frequency of 15 Hz with a phase margin of 40° and a gain margin of at least 10 dB. This is achieved with the compensator

$$c_{0_1} = \frac{117.14\,(s+100)\,(s+234.5)^2\,(s+15.62)\left(s^2+11.15s+1.96\times10^4\right)}{s\,(s+30.25)\,(s+23.38)\,(s+6.18)\,(s^2+468.2s+1.08\times10^5)} \tag{6.16}$$

Figure 6.16 shows the Bode plot of $L_{O_1} = GC_1 = c_{0_1}G_{\mathrm{SISO}_1}$. To ensure that $C_2 \in \mathcal{C}(L_O^*)$ such that $GC_2 = GC_1 = L_O^*$, the post-compensator for Design #2 must satisfy

$$c_{0_2} = \frac{L_O^*}{G_{\mathrm{SISO}_2}} \tag{6.17}$$

Linear analysis

Figure 6.17 compares $\|T_I\|$ and $\|S_IC\|$ for the two designs obtained in the previous section. The plots of $|T_O|$ and $|T_O|/\|G\|$ are also included, which represent the minimum possible value of $\|T_I\|$ and $\|S_IC\|$ in the case of perfect alignment according to Eqs. (4.23) and (4.24), respectively. Note that $|T_O|$ and $|T_O|/\|G\|$ are identical for both designs through the use of output equivalent controllers. Thus, the theoretical (linear) performance at the plant output is identical for the two designs. However, as previously discussed in Section 6.1, we expect very different performance at the plant input.

Figure 6.17(a) shows the plot of $\|T_I\|$ for Design #1. We see that $\|T_I\|$ has a large DC gain, which is due to the poor plant/controller alignment at low frequency. This will ultimately result in a large closed-loop response to input disturbances. On the other hand, we see that $\|T_I\|$ has a unity DC gain for Design #2 shown in Fig. 6.17(b). This is a direct result of the nearly perfect alignment achieved at low frequencies in Design #2. To illustrate the effect of alignment on the

closed-loop interactions at the plant input, we compare the DC gain matrix, $T_I(0)$, for each design:

$$\text{Design \#1:} \quad T_I(0) = \begin{bmatrix} 1 & 0 \\ 27.5 & 0 \end{bmatrix}$$

$$\text{Design \#2:} \quad T_I(0) = \begin{bmatrix} 1 & 0 \\ 0 & 0 \end{bmatrix}$$

Due to poor low frequency alignment, Design #1 produces a large off-diagonal term creating a significant one-way interaction between $d_{i1} \rightarrow u_2$ at the plant input. On the other hand, Design #2 produces no interactions due to perfect alignment at $\omega = 0$.

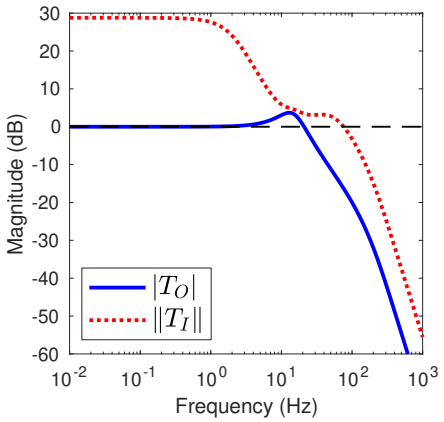

(a) $\|T_I\|$ for Design #1

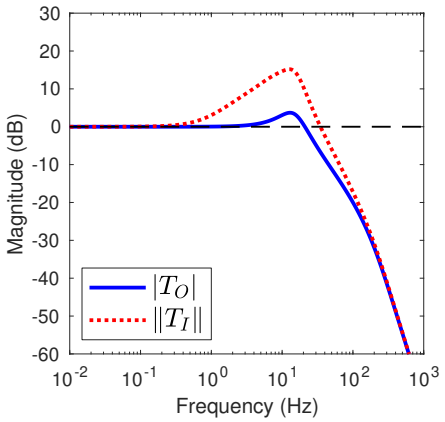

(b) $\|T_I\|$ for Design #2

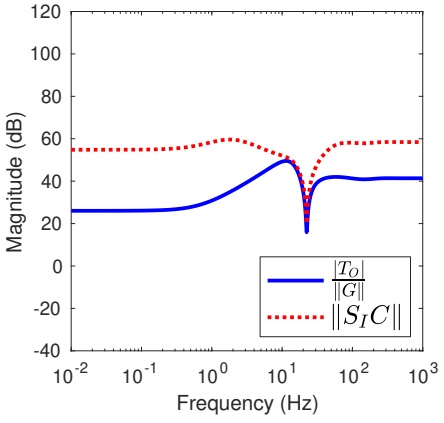

(c) $\|S_I C\|$ for Design #1

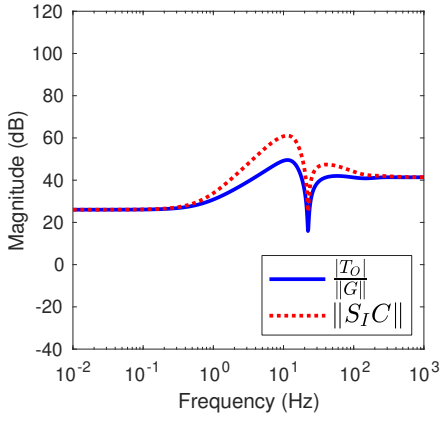

(d) $\|S_I C\|$ for Design #2

Figure 6.17: Comparison of input sensitivities

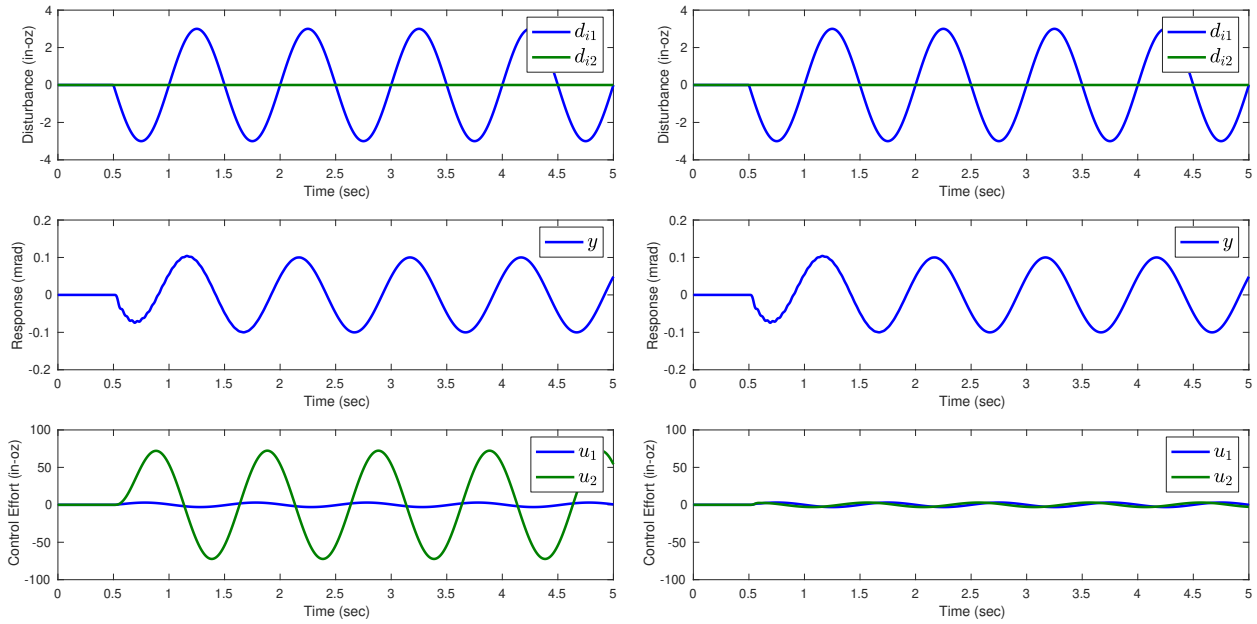

(a) Input disturbance response for Design #1

(b) Input disturbance response for Design #2

Figure 6.18: Comparison of input disturbance responses

The simulated linear closed-loop responses to a sinusoidal input disturbance, $d_{i1} = 3\sin(2\pi t)$, are compared in Fig. 6.18. Note that the output response, y, for each design is identical due to the use of output equivalent controllers. However, the input responses, u_1 and u_2, are drastically different. As shown in Fig. 6.18(a), Design #1 produces a large control response on the second controller output, u_2. This is undesirable in practice since the saturation limits of the secondary actuator are typically much smaller than the primary actuator. Indeed, Design #1 exceeds the saturation limits of the VCMs, which only provide a maximum torque capability of 16.1 in-oz. As shown in Fig. 6.18(b), Design #2 produces a well-behaved control response which avoids actuator saturation. This is due to the improved alignment at low frequency, hence smaller $\|T_I\|$ and reduced interactions.

Outer loop control design

The outer loop controller is designed to achieve a bandwidth roughly 5–10 times slower than the inner loop, which has a bandwidth of 25 Hz. Using a simple proportional gain, $C_{\text{outer}} = K_p = 25$, the outer loop controller provides a gain margin of 10 dB and a phase margin of 80°. The resulting closed-loop bandwidth is 5 Hz.

6.2.3 Friction compensation

In this case study, model-based friction compensation techniques are investigated using the data-based friction model developed in Chapter 3. The idea behind model-based friction compensation is depicted in Fig. 6.19. The true friction torque, T_f, is estimated using a model, and the estimate of the friction torque, $\hat{T}_f$, is added to the control signal to cancel out the effects. There are two primary friction compensation approaches: feedforward friction compensation and feedback friction compensation [27,28,30]. The feedforward approach, depicted in Fig. 6.19(a), is suitable for tracking applications when a non-zero velocity command, $\dot{\theta}_c$, is known in advance. The underlying assumption in the feedforward approach is that the velocity command is a good estimate of the actual velocity. Although this eliminates lag and noise effects on the velocity prediction, it is not suitable for inertial stabilization applications where the nominal velocity command is almost always zero. On the other hand, the feedback approach, depicted in Fig. 6.19(b), is suitable for inertial stabilization, but relies on having a good velocity estimate. In this case study, the outer axis optical encoder provides a high-resolution low-noise velocity measurement with minimal delay.

Clearly, the effectiveness of friction compensation depends on having a good friction model available. As previously discussed in Section 3.3, the data-based friction model developed in this research effort significantly improves model accuracy in both the time and frequency domains. Moreover, the data-based model is quite suitable for real-time implementation since it is implemented with a simple look up table. The performance of this data-based friction compensation approach is evaluated in Section 6.2.6.

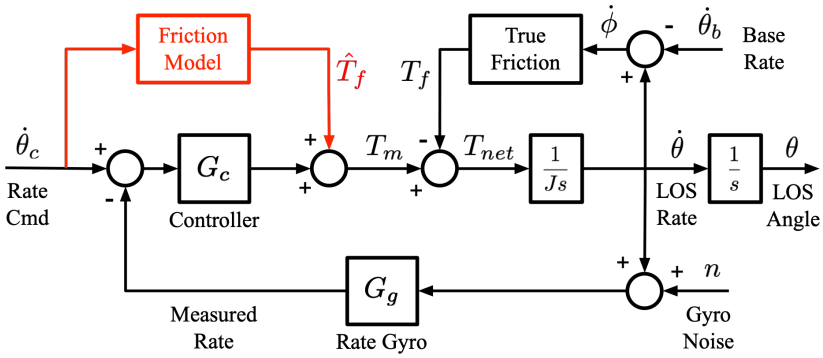

(a) Feedforward friction compensation

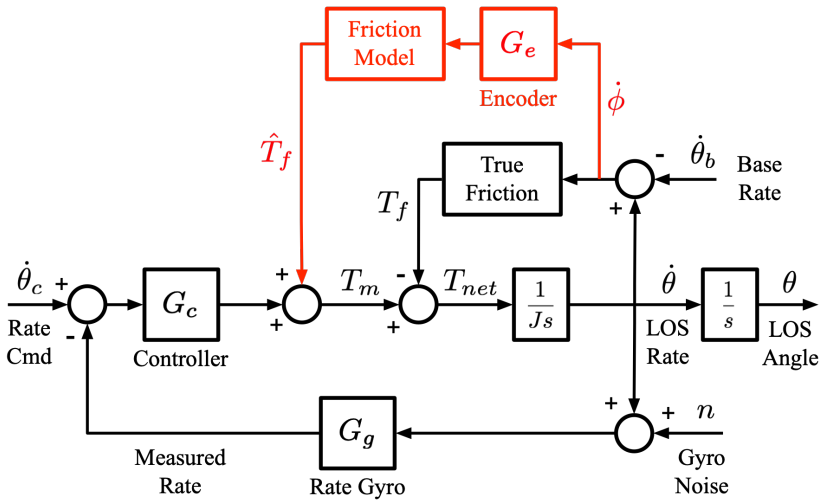

(b) Feedback friction compensation

Figure 6.19: Model-based friction compensation

6.2.4 Performance metrics

In order to make meaningful comparisons of performance between the poorly aligned and well-aligned controller designs, two performance metrics are defined. As discussed in Chapter 1, LOS jitter performance is critical in gimbaled pointing systems as it directly relates to the quality of the captured images. The second metric is control energy usage, which is particularly important in applications that have strict power requirements, such as aircraft or space vehicles.

Jitter performance

Jitter performance is commonly specified in terms of the RMS motion of the payload LOS [4]. The total RMS motion is expressed as

$$\theta_{\text{RMS}} = \sqrt{\frac{1}{N}\sum_{n=1}^{N}|\theta_n|^2} \tag{6.18}$$

where N is the number of samples over a window of interest for the evaluation of jitter. Alternatively, the standard deviation can be used when the motion is not about a zero mean. This is expressed as

$$\theta_{\text{RMS}} = \sqrt{\frac{1}{N}\sum_{n=1}^{N}|\theta_n - \bar{\theta}|^2} \tag{6.19}$$

where $\bar{\theta}$ is the mean value and is calculated as

$$\bar{\theta} = \frac{1}{N}\sum_{n=1}^{N}\theta_n \tag{6.20}$$

A total RMS jitter specification usually assumes that the motion consists primarily of high frequency random motion. As a result, the total RMS jitter metric can be misleading if the motion spectrum has significant low frequency content. Due to image sensor sampling effects, low frequency motions do not equally contribute to blurring. Thus, total RMS motion is not always an appropriate jitter metric [4].

In practice, it is often useful to estimate motion (jitter) over a sensor integration period.[1] For sinusoidal LOS motion, $\theta_m = \Theta_m \sin(2\pi F_m t + \phi_m)$, the actual motion detected over a sensor integration period, ΔT_i, is given by [8]

$$\Delta\theta_i = \left[1 - \frac{2 - 2\cos(2\pi F_m/F_i)}{(2\pi F_m/F_i)^2}\right]\Theta_m \tag{6.21}$$

where Θ_m is the amplitude of motion, F_m is the frequency of motion, and $F_i = 1/\Delta T_i$ is the sensor integration frequency. Evaluating Eq. (6.21) as a function of the normalized frequency, F_m/F_i, it

[1]The sensor integration period is the amount of time that an image sensor collects and accumulates charge due to incident photons. This is analogous to the shutter speed or exposure time in film cameras.

is shown in [4, 8] that the motion over a sensor integration period can be estimated using a high pass filter

$$\Delta\hat{\theta}_i(s) = \frac{s}{s + 2\pi(F_i/2\pi)}\theta_m(s) \tag{6.22}$$

where θ_m is the actual LOS motion. Thus, motions with spectral content lower than $F_i/2\pi$ will be weighted less than higher frequency content. The RMS jitter metric can then be calculated from the estimated motion, $\hat{\theta}_i$. The allowable motion during a sensor integration period will depend on the specific application as well as the image sensor characteristics and the imaging scenario. For the results presented in the following sections, a sensor integration period of $\Delta T_i = 1$ second is used.

Control energy usage

As discussed in Chapter 4, plant/controller alignment plays an important role in closed-loop performance at the plant input. Thus, another useful performance metric is the control energy usage. This is particularly important in applications that have strict power limitations. The instantaneous motor power can be calculated as

$$P_1 = i_1 V_1 = i_1^2 R_1 \quad \text{and} \quad P_2 = i_2 V_2 = i_2^2 R_2 \tag{6.23}$$

where i_1 and i_2 are the motor currents, V_1 and V_2 are the motor voltages, and $R_1 = 4.8\,\Omega$ and $R_2 = 6.8\,\Omega$ are the motor resistances for the coarse and fine actuators, respectively. The energy contribution for each actuator can be expressed as

$$E_1 = \int_0^t P_1 \, d\tau \quad \text{and} \quad E_2 = \int_0^t P_2 \, d\tau \tag{6.24}$$

where the integral is evaluated over the time interval of interest. The total control energy is then calculated as

$$E = E_1 + E_2 \tag{6.25}$$

6.2.5 Base motion profiles

Host vehicle vibration is typically specified in terms of amplitude and frequency using a power spectral density (PSD). Some common host vehicle vibration specifications can be found in the open literature. For example, the base motion for a "typical" space vehicle is given in [124]. The angular vibration specifications for a variety of different aircraft can be found in [125]. Once a PSD specification is known, base motion time histories can be synthesized by generating a series of randomly phased sinusoids with amplitudes that satisfy the PSD specification.

Figure 6.20 depicts the three base motion profiles that are used to evaluate jitter performance in this case study. The base motion PSDs in this study were obtained by modeling the PSD specifications for a typical space vehicle [124], and scaling them up to a level that was achievable in the inertial test configuration. The three base motion profiles are labeled as BM1, BM2, and BM3. As shown in Fig. 6.20(a), the cumulative spectral power (CSP) indicates the total contribution of RMS motion over frequency. BM1 provides lowest frequency content with a total RMS motion of 3 mrad. BM2 provides mid frequency content with a total RMS motion of 2.5 mrad. BM3 provides high frequency content with a total RMS motion of 2.1 mrad.

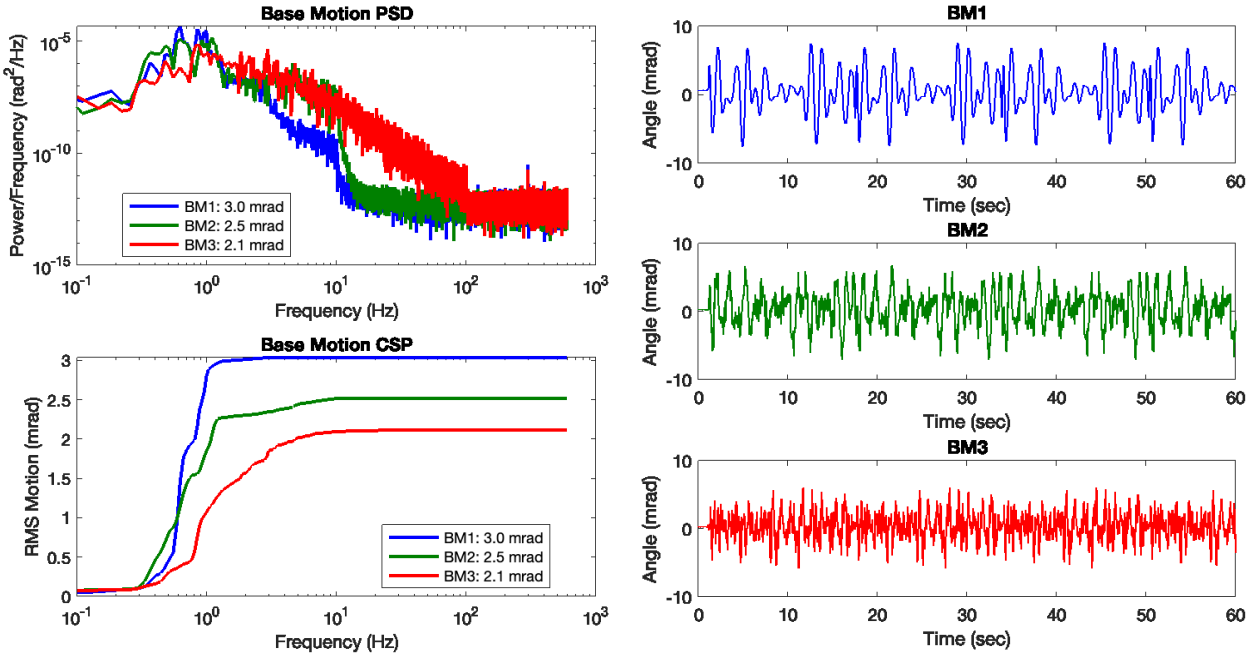

(a) (b)

Figure 6.20: Base motion profiles: (a) PSD, CSP, and (b) time histories

6.2.6 Simulated and experimental results

The two controller designs obtained in Section 6.2.2 were discretized using the bilinear (Tustin) approximation and implemented on the experimental testbed shown in Fig. 2.6. The three base motion profiles discussed in Section 6.2.5 were applied to the experimental system for a duration of 60 seconds each. The measured base motion disturbances from each test were recorded and then played back as an input to the nonlinear simulation. Figure 6.21 shows a snapshot comparing the simulated and experimental base disturbances responses. The simulated responses are in good agreement with the experimental results.

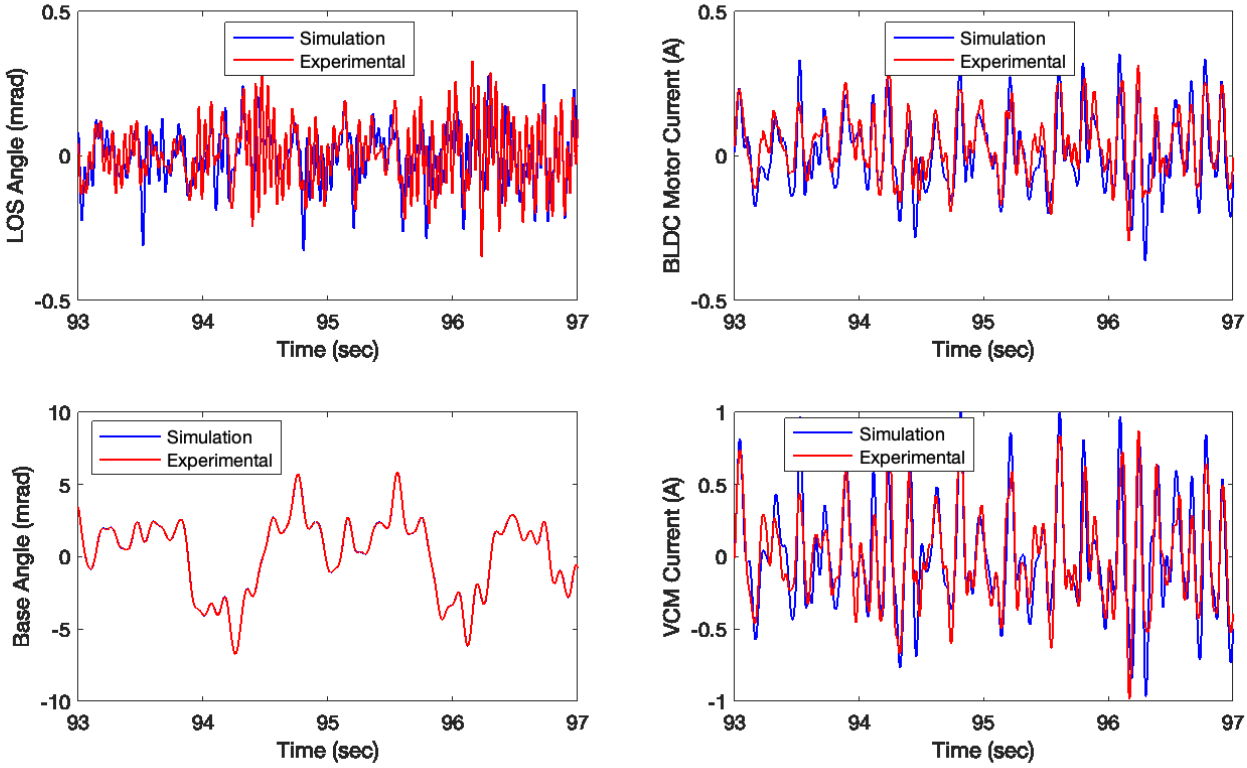

Figure 6.21: Comparison of simulated and experimental base disturbance responses

Figure 6.22 compares the experimental jitter performance for the BM1 profile. Relative jitter performance is compared against the baseline (open loop) case in Fig. 6.22(b). Here we see that the poorly aligned controller (Design #1) has the worst closed-loop performance. The well-aligned controller (Design #2) reduces jitter by nearly 60%. Using the model-based friction compensation technique described in Section 6.2.3, the jitter is reduced by nearly another 40%.

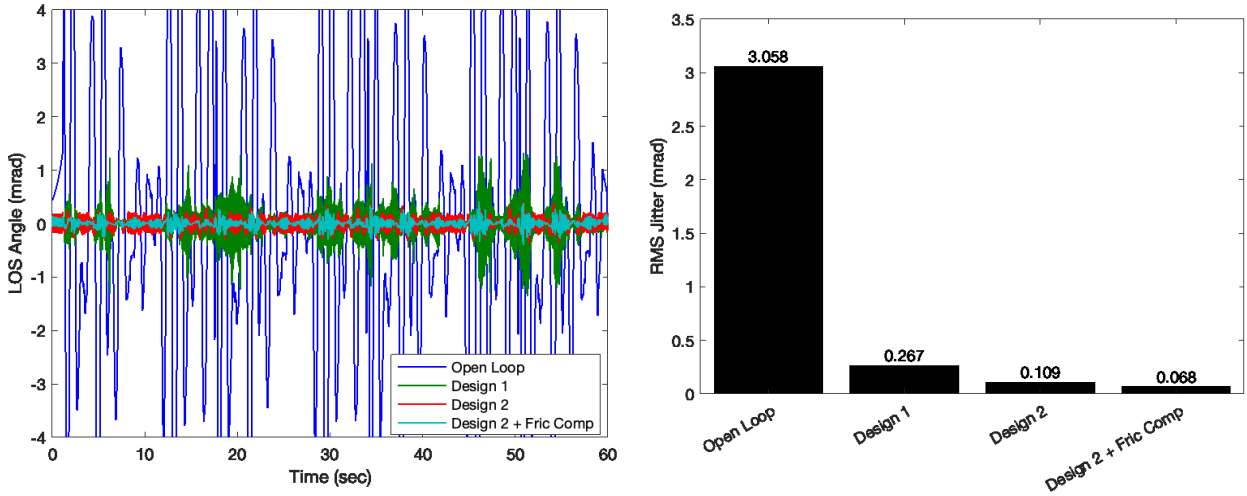

(a) (b)

Figure 6.22: Experimental jitter performance for the BM1 profile

Figure 6.23 compares the experimental control energy usage for the BM1 profile. Here we see that Design #1 uses significant control energy. The poor alignment of Design #1 causes excessive control activity and frequent saturation on the fine actuator channel, u_2, which dominates the control energy usage. The well-aligned controller reduces the control energy usage by approximately 95%. The use of model-based friction compensation provides another 25% reduction on the control energy usage.

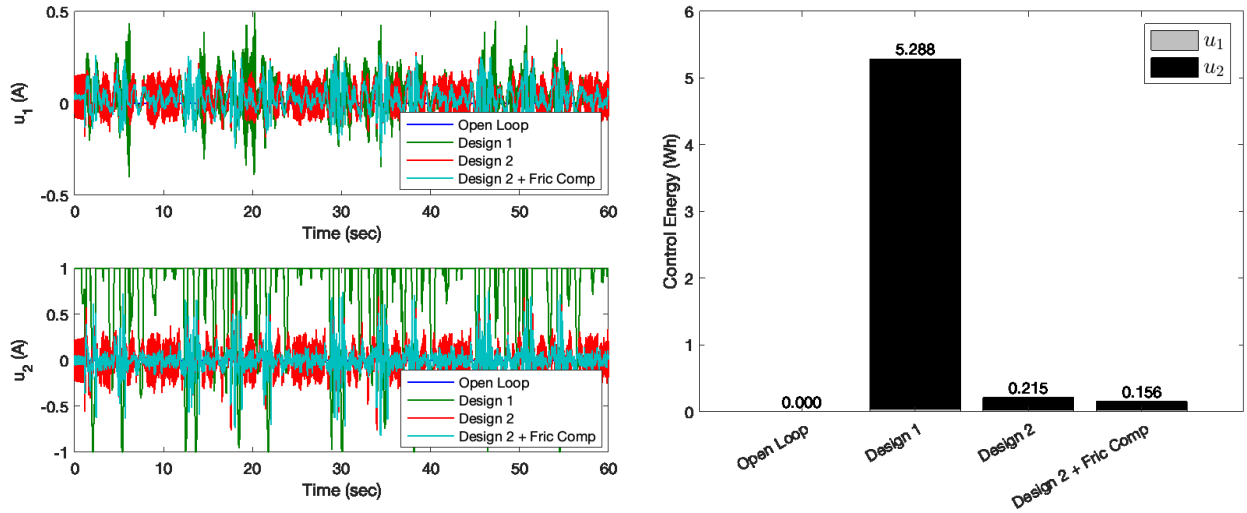

(a) (b)

Figure 6.23: Experimental control energy usage for the BM1 profile

Figure 6.24 compares the simulated and experimental jitter performance for all three base motion profiles. It is clear that the well-aligned control design provides better jitter performance than the poorly aligned control design in all three cases.

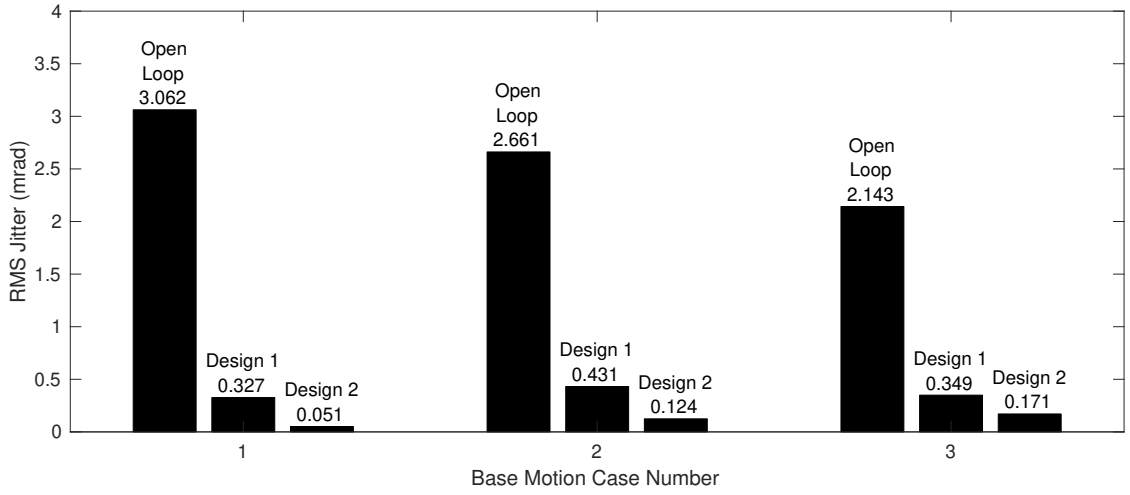

(a)

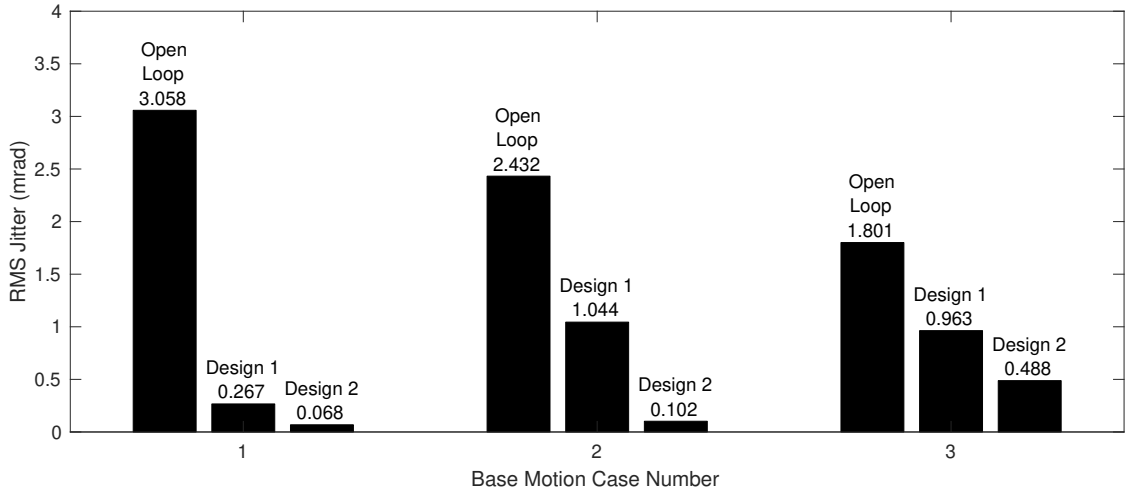

(b)

Figure 6.24: Comparison of (a) simulated and (b) experimental jitter performance

Figure 6.25 compares the simulated and experimental control energy for all three base motion profiles. The poorly aligned controller (Design #1) uses significantly more control energy than the well-aligned design in all cases. This is a result of the predicted large input sensitivities (see Fig. 6.17) caused by poor alignment.

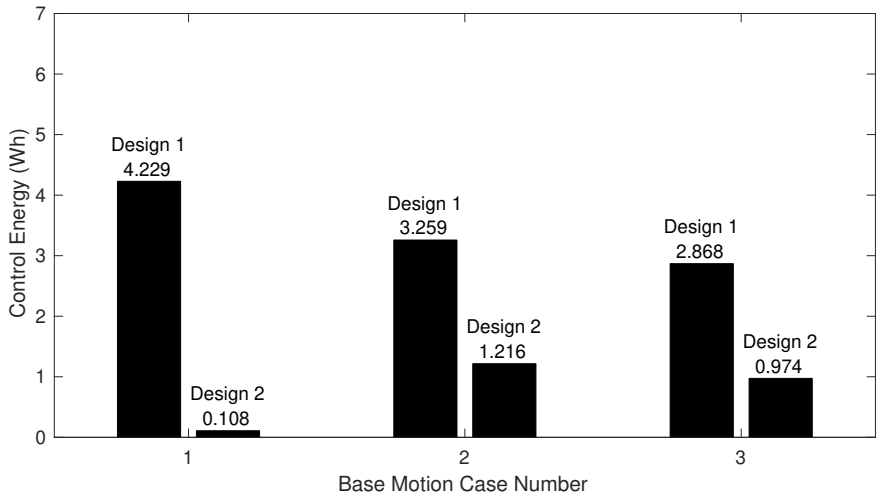

(a)

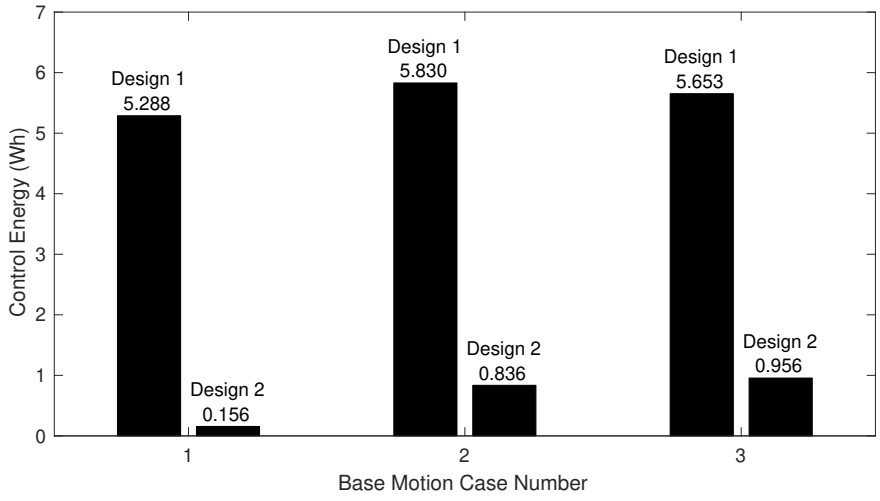

(b)

Figure 6.25: Comparison of (a) simulated and (b) experimental control energy

6.3 Chapter Summary

This chapter describes the application of the concepts of plant/controller alignment (from Chapter 4) and the graphical control design approach (from Chapter 5) to the hybrid flexure bearing testbed. Two case studies explore the performance of the hybrid flexure bearing concept. The first case study evaluates the tracking performance of the hybrid flexure testbed using relative position feedback. A design example shows the utility of the graphical control design approach using alignment contours. Two different control designs are compared: a controller that is poorly aligned with the plant, and a controller that is well aligned with the plant. The relative tracking performance

of both designs are evaluated and experimentally validated. Although the output performance of the two controllers are comparable (by design), the input performance is drastically different. The poorly aligned controller causes significant performance degradation at the plant input, leading to large control transients and significant interactions, as predicted by the alignment relationships described in Chapter 4.

The second case study explores the impact of plant/controller alignment on the pointing performance of the hybrid flexure bearing using inertial rate feedback for LOS stabilization in the presence of base motion disturbances. A well-aligned and poorly aligned controller are designed using the graphical design approach from Chapter 5. The pointing performance of each controller design is evaluated in simulation and validated with the experimental testbed under a variety base motion disturbances. This is accomplished with the inertial test configuration developed in Chapter 2. As predicted, the poorly aligned controller uses significantly more control energy than the well-aligned design. Moreover, the poorly aligned design has worse jitter performance due to excessive control activity and frequent saturation. Model-based friction compensation techniques are also investigated using the data-based dynamic friction model developed in Chapter 3. We show that the overall pointing performance is improved using the data-based friction compensation approach, reducing both jitter and control energy usage.

Chapter 7

Conclusions and Future Work

7.1 Summary of Research Contributions

This research seeks to advance the state-of-the-art in precision pointing through control design and evaluation of the hybrid flexure bearing concept. To achieve this goal, the following objectives are defined:

1) Develop an experimental testbed to fully characterize, model, and validate the hybrid flexure bearing prototype.
2) Develop an accurate model of the hybrid flexure bearing including nonlinear friction.
3) Identify and analyze closed-loop limitations.
4) Develop and evaluate potential control strategies for improved jitter rejection.
5) Validate control system approaches and performance with the experimental testbed.

Chapter 2 introduces the experimental system used to characterize and evaluate the hybrid flexure bearing concept. Building upon the foundations of previous work [21], this chapter describes several updates to the experimental testbed, including the integration of representative gimbal hardware and inertial sensors. These upgrades enable a new inertial test configuration to evaluate the hybrid flexure bearing under more realistic base disturbance environments.

Chapter 3 describes the development of linear and nonlinear dynamical models for the hybrid flexure bearing system. A significant challenge associated with the development of precision motion control systems is the identification and modeling of friction. In particular, dynamic presliding friction is often difficult to accurately model. For systems which undergo small motions with frequent velocity reversals, presliding friction effects dominate the system dynamics and the base motion disturbances and LOS become tightly coupled. An accurate friction model is crucial for assessing the impact of bearing friction on pointing performance. This chapter presents a data-based

dynamic friction model that significantly improves friction model accuracy in both the time and frequency domains. Key friction model features are identified to better match frictional behavior observed in experiments. Simulation results are validated with measured friction data collected from the experimental testbed.

Chapter 4 describes the properties of general two-input single-output (TISO) feedback systems and introduces the concepts of plant and controller "directions" and "alignment". Due to the unique structure of TISO feedback systems, several closed-loop properties can be characterized using the concept of plant/controller alignment. In general, it is desirable to design a controller that is well aligned with the plant in order to minimize the size of the closed-loop sensitivity functions and closed-loop interactions. Poor plant/controller alignment indicates significant limitations in terms of closed-loop performance.

Chapter 5 introduces a graphical controller design approach for general TISO systems which exploits the concept of plant/controller alignment. Although the concept of alignment can be a useful analysis tool for a given plant/controller pair, it is not obvious how a controller should be designed to achieve good alignment. This chapter presents a new graphical design approach, based on the PQ method [24], which explicitly incorporates knowledge of alignment into the control design process. This is accomplished by providing graphical information about the alignment angle on the Bode plot of the PQ frequency response. This allows the designer to easily determine the alignment over frequency for a given PQ loop shape. More importantly, the contours provide additional guidelines in the loop shaping process.

Chapter 6 describes the application of the concepts of plant/controller alignment and the graphical control design approach to the hybrid flexure bearing testbed. Two case studies explore the performance of the hybrid flexure bearing concept. The first case study evaluates the tracking performance of the hybrid flexure testbed using relative position feedback. A design example shows the utility of the graphical control design approach using alignment contours. Two different control designs are compared: a controller that is poorly aligned with the plant, and a controller that is well aligned with the plant. The relative tracking performance of both designs are evaluated and experimentally validated. The poorly aligned controller causes significant performance degradation at the plant input, leading to large control transients and significant interactions. The second case

study explores the impact of plant/controller alignment on the pointing performance of the hybrid flexure bearing using inertial rate feedback for LOS stabilization in the presence of base motion disturbances. The performance of a well-aligned and poorly aligned controller are evaluated in simulation and validated with the experimental testbed under a variety of base motion disturbances. As predicted, the poorly aligned controller uses significantly more control energy and has worse jitter performance due to excessive control activity and frequent saturation. Finally, model-based friction compensation techniques are investigated using the data-based friction model. The overall pointing performance is improved using the data-based approach, reducing both jitter and control energy usage.

7.2 Future Work

The contributions of this research establish initial efforts to advance the state-of-the-art in precision pointing through the control design and evaluation of the hybrid flexure bearing concept. Building on this work, the following topics are proposed as potential future research directions.

7.2.1 Coordinated plant/controller redesign for improved alignment

In this research effort, we primarily focused on the development and application of a new control design approach which can be used to shape a controller to achieve good alignment with a given plant over frequency. However, because the controller and plant both play a critical role in determining alignment, it is natural to consider how the concept of alignment can be used to inform changes to the plant to minimize closed-loop limitations and improve jitter performance. Alignment may be useful as a tool for plant modification and redesign. Ultimately, it is desirable to develop a coordinated design approach of both the plant and controller using the concepts of plant/controller alignment.

Open questions include:

- What are the optimal plant parameters, such as inertia ratio or flexure stiffness and damping?
- What is the optimal sensor and actuator placement?
- Are there alternate configurations that improve tracking and/or disturbance rejection?

7.2.2 Extension of plant/controller alignment to TITO feedback systems

In this work, the primary focus has been on TISO feedback systems. However, improvements could possibly be made through the use of an additional feedback sensor, thereby forming a TITO feedback system. Thus, it is natural to consider the extension of the plant/controller alignment approach to TITO feedback systems. For the TITO feedback configuration, the application of these concepts will involve studying alignment between the individual rows and columns of the plant and controller transfer matrices and their effect on closed-loop performance.

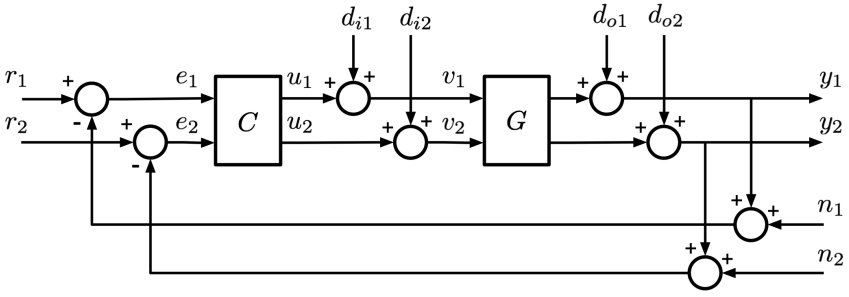

Figure 7.1: TITO feedback system

Consider the TITO feedback system in Fig. 7.1. The plant can be partitioned as

$$G = \begin{bmatrix} g_{11} & g_{12} \\ g_{21} & g_{22} \end{bmatrix} = \begin{bmatrix} G_{1\cdot} \\ G_{2\cdot} \end{bmatrix} \tag{7.1}$$

where $G_{i\cdot} \in \mathbb{C}^{1\times 2}$ denotes the i-th row of the plant transfer matrix. Similarly, the controller can be partitioned as

$$C = \begin{bmatrix} c_{11} & c_{12} \\ c_{21} & c_{22} \end{bmatrix} = \begin{bmatrix} C_{\cdot 1} & C_{\cdot 2} \end{bmatrix} \tag{7.2}$$

where $C_{\cdot j} \in \mathbb{C}^{2\times 1}$ denotes the j-th column of the controller. Thus, the plant/controller alignment can be defined by the two angles

$$\phi_1 \coloneqq \arccos\left(\frac{|G_{1\cdot}C_{\cdot 1}|}{\|G_{1\cdot}\|\|C_{\cdot 1}\|}\right) \tag{7.3}$$

$$\phi_2 \coloneqq \arccos\left(\frac{|G_{2\cdot}C_{\cdot 2}|}{\|G_{2\cdot}\|\|C_{\cdot 2}\|}\right) \tag{7.4}$$

where relationships between the alignment angles, ϕ_1 and ϕ_2, and the sizes of the closed-loop transfer functions, $\|S_I\|$ and $\|T_I\|$, can be obtained. To apply the concept of plant/controller alignment, controller elements are selected by treating the TITO control design problem as two sequential TISO design problems, as depicted in Fig. 7.2.

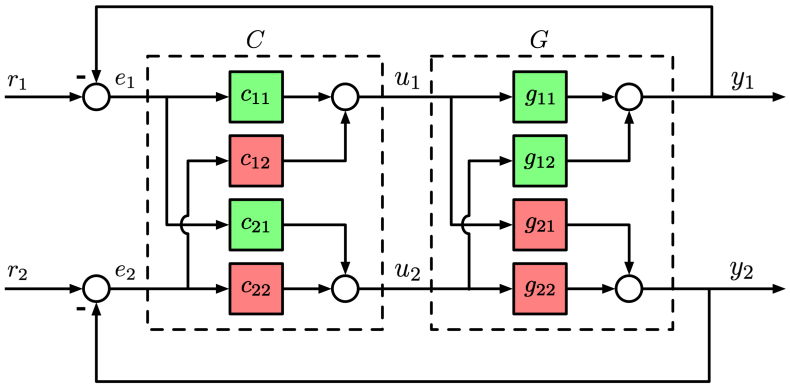

Figure 7.2: Proposed TITO design procedure: Treat the TITO control design problem as two sequential TISO design problems by first designing the green TISO subsystem to achieve good alignment, followed by the red TISO subsystem.

Although there are similar approaches which instead treat the TITO control design problem as two sequential SITO control designs [98, 99, 116], the resulting "alignment compensators" are rough approximations designed using knowledge of alignment at a single frequency, typically at DC only. Such compensators are typically chosen to be a simple static gain, thus only achieving good alignment in a small frequency range. One significant advantage of the control design approach developed in Chapter 5 is that it provides insight into shaping dynamic compensators to achieve a desired alignment over a wide frequency range.

7.2.3 Experimental testbed improvements

A limiting factor in the experimental testbed is the inability to apply more general base disturbance motions. This limitation is primarily due to 1) the relatively coarse resolution of the magnetic encoder used to measure the base motion, and 2) the lack of closed-loop control around the linear actuator which drives the base excitation. The 19-bit base encoder provides an angular resolution of 12 µrad. To achieve reasonable sub-microradian resolution, an encoder with at least 29-bit resolution is required. The use of an optical encoder similar to the unit installed in the single-axis

testbed would be an excellent candidate replacement option. Furthermore, closed-loop control of the base actuation system would provide more general wideband excitations to better approximate motions expected in real host vehicle disturbance environments. As discussed in Chapter 3, base motion amplitudes in the lower microradian range would allow the full evaluation of the frictional stiffness in the ball bearing joint.

Another limiting factor in the experimental testbed is the inherent delay in the IMU rate gyro measurement which limited the overall achievable bandwidth of the closed-loop system. The particular IMU used in this study provided a good balance between resolution, size, and weight. However, the overall closed-loop bandwidth could be improved by augmenting the IMU measurement with another high-bandwidth low-latency inertial sensor, such as an angular rate sensor (ARS) which is based on magnetohydrodynamic (MHD) principles [126, 127].

Finally, the experimental system would benefit from increased torque capability of the fine stage actuators. This would increase the maximum saturation levels of the fine stage, allowing for higher bandwidth control. Additional torque capability can be provided through the incorporation of additional VCMs into the rotational flexure axis.

References

[1] J. M. Hilkert, "Inertially stabilized platform technology: Concepts and principles," *IEEE Control Systems Magazine*, vol. 28, no. 1, pp. 26–46, Feb. 2008.

[2] "DJI handheld imaging products," https://www.dji.com, 2022.

[3] M. F. Winthrop and R. G. Cobb, "Survey of state-of-the-art vibration isolation research and technology for space applications," in *Proceedings of SPIE Smart Structures and Materials*, vol. 5052, San Diego, CA, Mar. 2003, pp. 13–26.

[4] J. M. Hilkert, M. Bowen, and J. Wang, "Specifications for image stabilization systems," in *Proceedings of SPIE Tactical Infrared Systems*, vol. 1498, Dallas, TX, May 1991, pp. 24–38.

[5] R. Miller, G. Mooty, and J. M. Hilkert, "Gimbal system configurations and line-of-sight control techniques for small UAV applications," in *Proceedings of SPIE*, vol. 8713, 2013, pp. 871 308–1–15.

[6] M. K. Masten, "Inertially stabilized platforms for optical imaging systems," *IEEE Control Systems Magazine*, vol. 28, no. 1, pp. 47–64, Feb. 2008.

[7] S. T. Jenkins and J. M. Hilkert, "Line of sight stabilization using image motion compensation," in *Proceedings of SPIE Acquisition, Tracking, and Pointing III*, vol. 1111, 1989.

[8] J. Hilkert, "Precision stabilized pointing and tracking systems," Georgia Tech Professional Education, DEF 8105P Short Course Notes, Atlanta, GA, July 2011.

[9] T. Andersen and A. Enmark, *Integrated Modeling of Telescopes*, ser. Astrophysics and Space Science Library. New York: Springer, 2011, vol. 377.

[10] S. Loewenthal, "SDIO tribomaterials/precision gimbal demonstration program," Air Force Materiel Command, Wright Patterson Air Force Base, OH, Tech. Rep. WL-TR-94-4094, Dec. 1993.

[11] C. A. Lagunowich, R. Sobek, M. McEver, and G. D. Danyo, "Friction effects on large gimbaled EO directors," in *Proceedings of SPIE Acquisition, Tracking, Pointing, and Laser Systems Technologies XXI*, vol. 6569, Orlando, FL, Apr. 2007, pp. 656 908–1–9.

[12] S. Cong, K. Deng, W. Shang, D. Kong, and H. Shen, "Isolation control for inertially stabilized platform based on nonlinear friction compensation," *Nonlinear Dynamics*, vol. 84, no. 3, pp. 1123–1133, 2016.

[13] J. M. Hilkert and B. Pautler, "A reduced-order disturbance observer applied to inertially stabilized line-of-sight control," in *Proceedings of SPIE Acquisition, Tracking, Pointing, and Laser Systems Technologies XXV*, vol. 8052, Orlando, FL, Apr. 2011, pp. 80 520H–1–12.

[14] P. J. Kennedy, R. L. Kennedy, and I. Agard, "Adaptive compensation for pointing and tracking systems applications," in *Proceedings of the IEEE International Conference on Control Applications*, Kohala Coast, Hawaii, Aug. 1999, pp. 279–284.

[15] M. Sweeney, E. Erdelyi, M. Ketabchi, and B. Kent, "Design considerations for optical pointing and scanning mechanisms," in *Proceedings of SPIE, Optomechanics*, vol. 5176, San Diego, CA, Aug. 2003, pp. 135–146.

[16] L. Zhuchong, L. Kun, and Z. Wei, "Inertially stabilized platform for airborne remote sensing using magnetic bearings," *IEEE/ASME Transactions on Mechatronics*, vol. 21, no. 1, pp. 288–301, Feb. 2016.

[17] M. N. Sweeney, G. A. Rynkowski, M. Ketabchi, and R. Crowley, "Design considerations for fast-steering mirrors (FSMs)," in *Proceedings of SPIE*, vol. 4773, 2002, pp. 63–73.

[18] J. M. Hilkert, "A comparison of inertial line-of-sight stabilization techniques using mirrors," in *Proceedings of SPIE Acquisition, Tracking, and Pointing XVIII*, vol. 5430, Orlando, FL, Apr. 2004, pp. 13–22.

[19] A. H. Slocum, *Precision Machine Design.* Dearborn, MI: Society of Manufacturing Engineers, 1992.

[20] S. T. Smith, *Flexures: Elements of Elastic Mechanisms.* Boca Raton, FL: CRC Press, 2000.

[21] P. S. Barney, N. A. Weir, and R. R. Rosenthal, "Combination bearing/flexure joint for large coarse motions and fine jitter control," Sandia National Laboratories, Albuquerque, NM, Tech. Rep. SAND2014-19413, Oct. 2014.

[22] T. E. Salas, P. S. Barney, A. M. Ison, R. L. Akau, and N. Weir, "Rotation flexure with temperature controlled modal frequency," U.S. Patent 9,759,263, Sep. 2017.

[23] ——, "Rotation flexure with temperature controlled modal frequency," U.S. Patent 10,288,121, May 2019.

[24] S. J. Schroeck, W. C. Messner, and R. J. McNab, "On compensator design for linear time-invariant dual-input single-output systems," *IEEE/ASME Transactions on Mechatronics*, vol. 6, no. 1, pp. 50–57, Mar. 2001.

[25] A. Lawrence, *Modern Inertial Technology.* New York: Springer-Verlag, 1993.

[26] S. Zotov, A. Srivastava, K. Kwon, J. Frank, E. Parco, M. Williams, S. Shtigluz, K. Lyons, M. Frazee, D. Hoyh, and A. Lu, "In-run navigation grade quartz MEMS-based IMU," in *Proceedings of the IEEE International Symposium on Inertial Sensors and Systems (INERTIAL)*, Hiroshima, Japan, Mar. 2020.

[27] B. Armstrong-Hélouvry, *Control of Machines with Friction.* Boston, MA: Kluwer Academic Publishers, 1991.

[28] B. Armstrong-Hélouvry, P. Dupont, and C. Canudas de Wit, "A survey of models, analysis tools and compensation methods for the control of machines with friction," *Automatica*, vol. 30, no. 7, pp. 1083–1138, 1994.

[29] ——, "Friction in servo machines: Analysis and control methods," *Applied Mechanics Reviews*, vol. 47, no. 7, pp. 275–305, Jul. 1994.

[30] H. Olsson, K. J. Åström, C. Canudas de Wit, M. Gäfvert, and P. Lischinsky, "Friction models and friction compensation," *European Journal of Control*, vol. 4, no. 3, pp. 176–195, 1998.

[31] F. Wang, T. Hurst, D. Abramovitch, and G. Franklin, "Disk drive pivot nonlinearity modeling part II: Time domain," in *Proceedings of the American Control Conference*, Baltimore, MD, Jun. 1994, pp. 2604–2607.

[32] R. H. A. Hensen, M. J. G. van de Molengraft, and M. Steinbuch, "Frequency domain identification of dynamic friction model parameters," *IEEE Transactions on Control Systems Technology*, vol. 10, no. 2, pp. 191–196, Mar. 2002.

[33] P. R. Dahl and R. Wilder, "Math model of hysteresis in piezo-electric actuators for precision pointing systems," in *Proceedings of the 8th Annual AAS Rocky Mountain Guidance and Control Conference*, Keystone, CO, Feb. 1985, pp. 61–88.

[34] P. R. Dahl and J. H. Ly, "Dynamic hysteresis modeling," in *Proceedings of the AIAA Modeling and Simulation Technologies Conference*, Denver, CO, Aug. 2000, pp. AIAA–2000–4094–1–13.

[35] N. A. Weir and A. G. Alleyne, "An improved dynamic friction model using a data-based approach," in *Proceedings of the ASME Dynamic Systems and Control Conference*, Tysons, VA, Oct. 2017.

[36] B. Feeny, A. Guran, N. Hinrichs, and K. Popp, "A historical review on dry friction and stick-slip phenomena," *Applied Mechanics Reviews*, vol. 51, no. 5, pp. 321–341, May 1998.

[37] J. Awrejcewicz and P. Olejnik, "Analysis of dynamic systems with various friction laws," *Applied Mechanics Reviews*, vol. 58, no. 6, pp. 389–411, Nov. 2005.

[38] F. Marques, P. Flores, J. C. Pimenta Claro, and H. M. Lankarani, "A survey and comparison of several friction force models for dynamic analysis of multibody mechanical systems," *Nonlinear Dynamics*, vol. 86, no. 3, pp. 1407–1443, 2016.

[39] D. Karnopp, "Computer simulation of stick-slip friction in mechanical dynamic systems," *Journal of Dynamic Systems, Measurement, and Control*, vol. 107, no. 1, pp. 100–103, Mar. 1985.

[40] S. Futami, A. Furutani, and S. Yoshida, "Nanometer positioning and its micro-dynamics," *Nanotechnology*, vol. 1, no. 1, pp. 31–37, 1990.

[41] B. A. Awabdy, W.-C. Shih, and D. M. Auslander, "Nanometer positioning of a linear motion stage under static loads," *IEEE/ASME Transactions on Mechatronics*, vol. 3, no. 2, pp. 113–119, Jun. 1998.

[42] B. J. Hamrock and D. Dowson, *Ball Bearing Lubrication: The Elastohydrodynamics of Elliptical Contacts*. New York: John Wiley & Sons, 1981.

[43] ——, "Ball bearing mechanics," NASA Lewis Research Center, Cleveland, OH, Technical Memorandum NASA-TM-81691, Jun. 1981.

[44] B. J. Hamrock and W. J. Anderson, "Rolling-element bearings," NASA Lewis Research Center, Cleveland, OH, NASA Reference Publication NASA-RP-1105, Jun. 1983.

[45] P. R. Dahl, "A solid friction model," The Aerospace Corporation, El Segundo, CA, Tech. Rep. TOR-0158(3107-18)-1, May 1968.

[46] C. Canudas de Wit, H. Olsson, K. J. Åström, and P. Lischinsky, "A new model for control of systems with friction," *IEEE Transactions on Automatic Control*, vol. 40, no. 3, pp. 419–425, Mar. 1995.

[47] P. Dupont, V. Hayward, B. Armstrong, and F. Altpeter, "Single state elastoplastic friction models," *IEEE Transactions on Automatic Control*, vol. 47, no. 5, pp. 787–792, May 2002.

[48] J. Swevers, F. Al-Bender, C. G. Ganseman, and T. Prajogo, "An integrated friction model structure with improved presliding behavior for accurate friction compensation," *IEEE Transactions on Automatic Control*, vol. 45, no. 4, pp. 675–686, Apr. 2000.

[49] V. Lampaert, F. Al-Bender, and J. Swevers, "A generalized Maxwell-slip friction model appropriate for control purposes," in *Proceedings of the IEEE International Conference on Physics and Control*, St. Petersburg, Russia, Aug. 2003, pp. 1170–1178.

[50] B. S. R. Armstrong and Q. Chen, "The Z-properties chart: Visualizing the presliding behavior of state-variable friction models," *IEEE Control Systems Magazine*, vol. 28, no. 5, pp. 79–89, Oct. 2008.

[51] P. R. Dahl, "Solid friction damping of spacecraft oscillations," in *Proceedings of the AIAA Guidance and Control Conference*, Boston, MA, Aug. 1975, pp. 75–1104–1–13.

[52] N. A. Osborne and D. L. Rittenhouse, "The modeling of friction and its effects on fine pointing control," in *Proceedings of the AIAA Mechanics and Control of Flight Conference*, Anaheim, CA, Aug. 1974, pp. 74–875–1–10.

[53] I. D. Mayergoyz, "Mathematical models of hysteresis," *IEEE Transactions on Magnetics*, vol. 22, no. 5, pp. 603–608, 1986.

[54] ——, *Mathematical Models of Hysteresis*. Springer-Verlag, 1991.

[55] P. R. Dahl, "Measurement of solid friction parameters of ball bearings," The Aerospace Corporation, El Segundo, CA, Tech. Rep. SAMSO-TR-77-132, Mar. 1977.

[56] V. Lampaert, J. Swevers, and F. Al-Bender, "Modification of the Leuven integrated friction model structure," *IEEE Transactions on Automatic Control*, vol. 47, no. 4, pp. 683–687, Apr. 2002.

[57] J. Y. Yoon and D. L. Trumper, "Friction modeling, identification, and compensation based on friction hysteresis and Dahl resonance," *Mechatronics*, vol. 24, no. 6, pp. 734–741, Sep. 2014.

[58] D. Abramovitch, F. Wang, and G. Franklin, "Disk drive pivot nonlinearity modeling part I: Frequency domain," in *Proceedings of the American Control Conference*, Baltimore, MD, Jun. 1994, pp. 2600–2603.

[59] F. Al-Bender and W. Symens, "Dynamic characterization of hysteresis elements in mechanical systems. I. Theoretical analysis," *Chaos*, vol. 15, no. 1, pp. 013 105–1–11, 2005.

[60] D. Helmick and W. Messner, "Describing function analysis of Dahl model friction," in *Proceedings of the American Control Conference*, St. Louis, MO, Jun. 2009, pp. 814–819.

[61] R. Pintelon and J. Schoukens, *System Identification: A Frequency Domain Approach*, 2nd ed. Hoboken, NJ: John Wiley & Sons, 2012.

[62] J. Schoukens, M. Vaes, and R. Pintelon, "Linear system identification in a nonlinear setting: Nonparametric analysis of the nonlinear distortions and their impact on the best linear approximation," *IEEE Control Systems Magazine*, vol. 36, no. 3, pp. 38–69, Jun. 2016.

[63] G. C. Goodwin, S. E. Graebe, and M. E. Salgado, *Control System Design*. Upper Saddle River, NJ: Prentice Hall, 2001.

[64] K. J. Åström and T. Hägglund, *Advanced PID Control*. Research Triangle Park, NC: International Society of Automation, 2006.

[65] S. Skogestad and I. Postlethwaite, *Multivariable Feedback Control: Analysis and Design*, 2nd ed. West Sussex, England: John Wiley & Sons, 2005.

[66] B. J. Lurie and P. J. Enright, *Classical Feedback Control: With MATLAB and Simulink*, 2nd ed. Boca Raton, FL: CRC Press, 2012.

[67] K. El Rifai, O. El Rifai, and K. Youcef-Toumi, "On dual actuation in atomic force microscopes," in *Proceedings of the American Control Conference*, Boston, MA, Jun. 2004.

[68] W. S. Nagel, G. M. Clayton, and K. K. Leang, "Master-slave control with hysteresis inversion for dual-stage nanopositioning systems," in *Proceedings of the American Control Conference*, Boston, MA, Jul. 2016.

[69] W. S. Nagel and K. K. Leang, "Cascading structure linear quadratic tracking control for dual-stage nanopositioning systems," in *Proceedings of the American Control Conference*, Denver, CO, Jul. 2020, pp. 70–75.

[70] Z. Wu, X. Chen, W. Hua, and J. Wang, "Design of coarse-fine control system for wafer stage of lithography using PQ method," in *Proceedings of ISSCAA*, Harbin, China, Jun. 2010.

[71] U. Boettcher, B. Raeymaekers, R. A. de Callafon, and F. E. Talke, "Dynamic modeling and control of a piezo-electric dual-stage tape servo actuator," *Transactions on Magnetics*, vol. 45, no. 7, pp. 3017–3024, Jul. 2009.

[72] K. Mori, T. Munemoto, H. Otsuki, Y. Yamaguchi, and K. Akagi, "A dual-stage magnetic disk drive actuator using a piezoelectric device for a high track density," *IEEE Transactions on Magnetics*, vol. 27, no. 6, pp. 5298–5300, Nov. 1991.

[73] T. Hirano, L.-S. Fan, W. Y. Lee, J. Hong, W. Imaino, S. Pattanaik, S. Chan, P. Webb, R. Horowitz, S. Aggarwal, and D. A. Horsley, "High-bandwidth high-accuracy rotary microactuators for magnetic hard disk drive tracking servos," *IEEE/ASME Transactions on Mechatronics*, vol. 3, no. 3, pp. 156–165, Sep. 1998.

[74] W. Guo, S. Weerasooriya, T. B. Goh, Q. H. Li, C. Bi, K. T. Chang, and T. S. Low, "Dual stage actuators for high density rotating memory devices," *IEEE Transactions on Magnetics*, vol. 34, no. 2, pp. 450–455, Mar. 1998.

[75] L. Guo, D. Martin, and D. Brunnett, "Dual-stage actuator servo control for high density disk drives," in *Proceedings of the IEEE/ASME International Conference on Advanced Intelligent Mechatronics*, Atlanta, GA, Sep. 1999, pp. 132–137.

[76] T. Semba, T. Hirano, J. Hong, and L.-S. Fan, "Dual-stage servo controller for HDD using MEMS microactuator," *IEEE Transactions on Magnetics*, vol. 35, no. 5, pp. 2271–2273, Sep. 1999.

[77] S.-H. Lee, Y.-H. Kim, and C. C. Chung, "Dual-stage actuator disk drives for improved servo performance: Track follow, track seek, and settle," *IEEE Transactions on Magnetics*, vol. 37, no. 4, pp. 1887–1890, Jul. 2001.

[78] R. Horowitz, Y. Li, K. Oldham, S. Kon, and X. Huang, "Dual-stage servo systems and vibration compensation in computer hard disk drives," *Control Engineering Practice*, vol. 15, no. 3, pp. 291–305, 2007.

[79] A. Al Mamun, G. Guo, and C. Bi, *Hard Disk Drive Mechatronics and Control*. Boca Raton, FL: CRC Press, 2007.

[80] G. Cherubini, C. C. Chung, W. C. Messner, and S. O. R. Moheimani, "Control methods in data-storage systems," *IEEE Transactions on Control Systems Technology*, vol. 20, no. 2, pp. 296–322, Mar. 2012.

[81] M. C. O'Neal and J. T. Spanos, "Optical pathlength control in the nanometer regime on the JPL phase B interferometer testbed," in *Proceedings of SPIE Active and Adaptive Optical Systems*, vol. 1542, San Diego, CA, Jul. 1991, pp. 359–370.

[82] G. W. Neat, J. D. O'Brien, N. M. Nerheim, R. J. Calvet, H. Singh, and S. B. Shaklan, "Microprecision interferometer test bed: First stabilized stellar fringes," in *Proceedings of SPIE, Spaceborne Interferometry II*, vol. 2477, Orlando, FL, 1995.

[83] G. W. Neat, J. W. Melody, and B. J. Lurie, "Vibration attenuation approach for spaceborne optical interferometers," *IEEE Transactions on Control Systems Technology*, vol. 6, no. 6, pp. 689–700, Nov. 1998.

[84] B. J. Lurie and F. Y. Hadaegh, "Control of systems with tiered actuators with application to interferometer optical delay line control," in *Proceedings of the 11th International Conference on Integrated Navigation Systems*, St. Petersburg, Russia, May 2004.

[85] M. Stalder, Y. Michellod, P. Mullhaupt, and D. Gillet, "Dedicated controller design for a dual-stage opto-mechatronic system," in *Proceedings of the IEEE/ASME International Conference on Advanced Intelligent Mechatronics*, Xi'an, China, Jul. 2008.

[86] S. Woody and S. Smith, "Design and performance of a dual drive system for tip-tilt angular control of a 300 mm diameter mirror," *Mechatronics*, vol. 16, no. 7, pp. 389–397, 2006.

[87] E. D. Miller and R. A. de Callafon, "Dual-stage servo control for an optical pointing system," in *Proceedings of the ASME Information Storage and Processing Systems Conference*, Santa Clara, CA, Jun. 2013.

[88] P. Gorzelic, E. Hellström, A. Stefanopoulou, L. Jiang, and S. Gopinath, "A coordinated approach for throttle and wastegate control in turbocharged spark ignition engines," in *Proceedings of the Chinese Control and Decision Conference*, Taiyuan, China, May 2012.

[89] S. Brennan and A. Alleyne, "Integrated vehicle control via coordinated steering and wheel torque inputs," in *Proceedings of the American Control Conference*, Arlington, VA, Jun. 2001.

[90] J. Freudenberg and R. Middleton, "Properties of single input, two output feedback systems," *International Journal of Control*, vol. 72, no. 16, pp. 1446–1465, 1999.

[91] K. Zhou, J. C. Doyle, and K. Glover, *Robust and Optimal Control*. Upper Saddle River, NJ: Prentice Hall, 1996.

[92] K. Scharnhorst, "Angles in complex vector spaces," *Acta Applicandae Mathematicae*, vol. 69, no. 1, pp. 95–103, 2001.

[93] A. R. Woodyatt, J. S. Freudenberg, and R. H. Middleton, "An integral constraint for single input two output feedback systems," *Automatica*, vol. 37, no. 11, pp. 1717–1726, 2001.

[94] A. R. Woodyatt, "Feedback control of multivariable non-square systems," Ph.D. dissertation, University of Newcastle, Callaghan, Australia, 1999.

[95] J. S. Freudenberg and D. P. Looze, "Right half plane poles and zeros and design tradeoffs in feedback systems," *IEEE Transactions on Automatic Control*, vol. 30, no. 6, pp. 555–565, Jun. 1985.

[96] ——, *Frequency Domain Properties of Scalar and Multivariable Feedback Systems*. Berlin: Springer-Verlag, 1988.

[97] M. M. Seron, J. H. Braslavsky, and G. C. Goodwin, *Fundamental Limitations in Filtering and Control*. London: Springer-Verlag, 1997.

[98] J. Freudenberg and R. Middleton, "Design rules for multivariable feedback systems," in *Proceedings of the IEEE Conference on Decision and Control*, Kobe, Japan, Dec. 1996, pp. 1980–1985.

[99] J. S. Freudenberg and A. Y. Karnik, "Reverse engineering a multivariable controller: A case study," in *Proceedings of the American Control Conference*, Portland, OR, Jun. 2005, pp. 733–738.

[100] N. A. Weir and A. G. Alleyne, "A graphical design approach for two-input single-output systems exploiting plant/controller alignment: Design and application," *Journal of Dynamic Systems, Measurement, and Control*, vol. 142, no. 1, p. 011006, Jan. 2020.

[101] ——, "Controller design for two-input single-output systems exploiting plant/controller alignment," in *Proceedings of the ASME Dynamic Systems and Control Conference*, Atlanta, GA, Oct. 2018.

[102] S.-M. Suh, C. C. Chung, and S.-H. Lee, "Design and analysis of dual-stage servo system for high track density HDDs," *Microsystem Technologies*, vol. 8, pp. 161–168, 2002.

[103] J. Freudenberg and R. Middleton, "Robustness of decoupling with almost redundant inputs," in *Proceedings of the American Control Conference*, Anchorage, AK, May 2002, pp. 2741–2746.

[104] J. S. Freudenberg and R. H. Middleton, "Scaling and redundancy for ill-conditioned two input, two output plants," *Automatica*, vol. 38, no. 3, pp. 499–505, 2002.

[105] T. Suzuki, T. Usui, M. Sasaki, F. Fujisawa, T. Yoshida, and H. Hirai, "Comparison of robust track-following control systems for a dual stage hard disk drive," in *Proceedings of the International Conference on Micromechatronics for Information and Precision Equipment*, 1997, pp. 101–118.

[106] S.-M. Suh, C. Choo, and S.-H. Lee, "Discrete-time LQG/LTR dual-stage controller design in magnetic disk drives," *IEEE Transactions on Magnetics*, vol. 37, no. 4, pp. 1891–1895, Jul. 2001.

[107] Y. Li and R. Horowitz, "Design and testing of track-following controllers for dual-stage servo systems with PZT actuated suspensions," *Microsystem Technologies*, vol. 8, pp. 194–205, 2002.

[108] M. Rotunno, R. A. De Callafon, and F. E. Talke, "Comparison and design of servo controllers for dual-stage actuators in hard disk drives," *IEEE Transactions on Magnetics*, vol. 39, no. 5, pp. 2597–2599, Sep. 2003.

[109] G. Herrmann and G. Guo, "HDD dual-stage servo-controller design using a μ-analysis tool," *Control Engineering Practice*, vol. 12, no. 3, pp. 241–251, Mar. 2004.

[110] X. Huang, R. Nagamune, R. Horowitz, and Y. Li, "Design and analysis of a dual-stage disk drive servo system using an instrumented suspension," in *Proceedings of the American Control Conference*, Boston, MA, Jul. 2004, pp. 535–540.

[111] X. Huang and R. Horowitz, "Robust controller design of a dual-stage disk drive servo system with an instrumented suspension," *IEEE Transactions on Magnetics*, vol. 41, no. 8, pp. 2406–2413, Aug. 2005.

[112] X. Huang, R. Horowitz, and Y. Li, "A comparative study of MEMS microactuators for use in a dual-stage servo with an instrumented suspension," *IEEE/ASME Transactions on Mechatronics*, vol. 11, no. 5, pp. 524–532, Oct. 2006.

[113] X. Huang, R. Nagamune, and R. Horowitz, "A comparison of multirate robust track-following control synthesis techniques for dual-stage and multisensing servo systems in hard disk drives," *IEEE Transactions on Magnetics*, vol. 42, no. 7, pp. 1896–1904, Jul. 2006.

[114] J. Ding, M. Tomizuka, and H. Numasato, "Design and robustness analysis of dual stage servo system," in *Proceedings of the American Control Conference*, Chicago, IL, Jun. 2000, pp. 2605–2609.

[115] U. Boettcher, R. A. De Callafon, and F. E. Talke, "Modeling and control of a dual stage actuator hard disk drive," *Journal of Advanced Mechanical Design, Systems, and Manufacturing*, vol. 4, no. 1, pp. 107–118, 2010.

[116] M. Kerr, C.-Y. Lan, and S. Jayasuriya, "Control of two-input two-output systems exploiting alignment," in *Proceedings of the IEEE Conference on Decision and Control*, San Diego, CA, Dec. 2006, pp. 4393–4398.

[117] A. Saberi and P. Sannuti, "Squaring down by static and dynamic compensators," *IEEE Transactions on Automatic Control*, vol. 33, no. 4, pp. 358–365, Apr. 1988.

[118] E. J. Davison, "Some properties of minimum phase systems and 'squared-down' systems," *IEEE Transactions on Automatic Control*, vol. 28, no. 2, pp. 221–222, Feb. 1983.

[119] W. Messner, "Some advances in loop shaping controller design with applications to disk drives," *IEEE Transactions on Magnetics*, vol. 37, no. 2, pp. 651–656, Mar. 2001.

[120] S. C. Smith and W. Messner, "Loop shaping with closed-loop magnitude contours on the Bode plot," in *Proceedings of the American Control Conference*, Anchorage, AK, May 2002.

[121] L. Xia and W. Messner, "An improved version of the RBode plot," in *Proceedings of the American Control Conference*, Seattle, WA, Jun. 2008.

[122] T. Atsumi and W. C. Messner, "Modified Bode plots for robust performance in SISO systems with structured and unstructured uncertainties," *IEEE Transactions on Control Systems Technology*, vol. 20, no. 2, pp. 356–368, Mar. 2012.

[123] H. W. Bode, *Network Analysis and Feedback Amplifier Design.* New York: D. Van Nostrand Company, 1945.

[124] J. Negro and S. Griffin, "Inertially stabilized platforms for precision pointing: Applications to directed-energy weapons and space-based lasers," Boeing-SVS, Albuquerque, NM, Tech. Rep. AFRL-VS-PS-JA-2006-1017, 2006.

[125] P. Merritt, J. Donaldson, D. O'Brien, K. Coleman, and G. Pyles, "Angular vibration survey of various aircraft," in *Proceedings of SPIE, Laser Systems Technology*, vol. 5087, Orlando, FL, Apr. 2003, pp. 35–45.

[126] D. Laughlin and D. Smith, "ARS-12G inertial angular vibration sensor provides nanoradian measurement," in *Proceedings of SPIE Acquisition, Tracking, and Pointing XV*, vol. 4365, Orlando, FL, Apr. 2001, pp. 168–175.

[127] D. Laughlin, H. Sebesta, and D. Eckelkamp-Baker, "A dual function magnetohydrodynamic (MHD) device for angular motion measurement and control," in *Proceedings of the 25th Annual AAS Guidance and Control Conference*, vol. 111, Breckenridge, CO, Feb. 2002, pp. 335–347.

[128] K. Ogata, *Modern Control Engineering*, 3rd ed. Upper Saddle River, NJ: Prentice Hall, 1997.

Appendix A

Testbed Characterization

A.1 Motor Characterization

A.1.1 Brushless torque motor

The back EMF for the brushless torque motor was measured via manual motion tests on both the rigid (1-DOF) and flexure (2-DOF) testbeds. The measured back EMF voltages are shown in Fig. A.1. The back EMF constant is estimated using a least-squares linear fit of the data. The motor torque constant is equivalent to the back EMF constant with the appropriate units. The measured brushless torque motor parameter values are compared to the nominal manufacturer values in Table A.1. Note that the measured parameters are nearly identical for both testbeds since the same type of brushless motor is used.

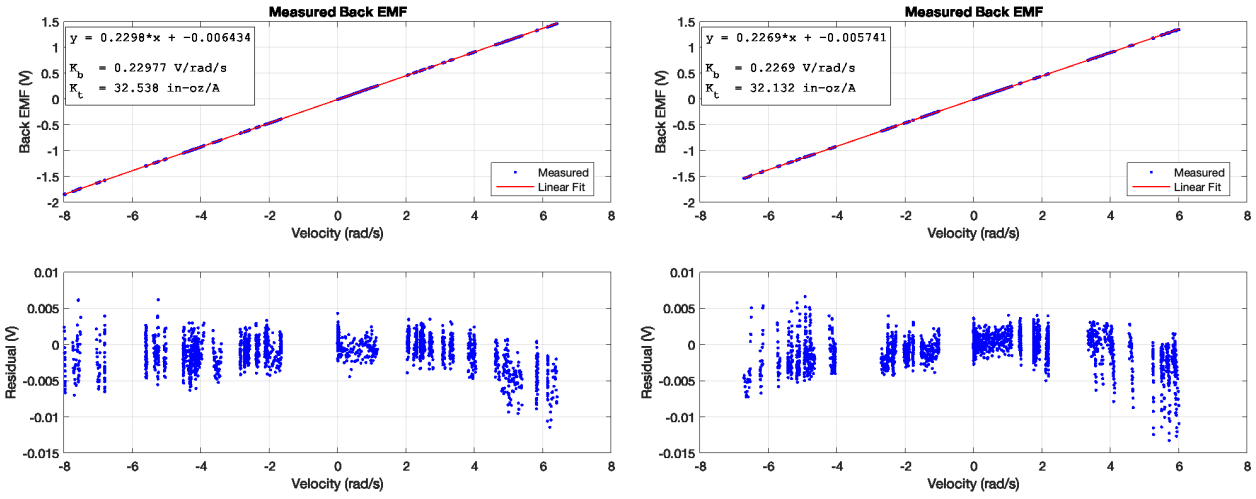

(a) Measured back EMF for TB1

(b) Measured back EMF for TB2

Figure A.1: Brushless torque motor back EMF measurements

Table A.1: Brushless torque motor parameters

Parameter	**Symbol**	**Nominal**	**Measured (1-DOF)**	**Measured (2-DOF)**	**Units**
Back EMF constant	K_b	$0.235 \pm 10\%$	0.230	0.227	V/rad/s
Torque constant	K_t	$34.0 \pm 10\%$	32.5	32.1	in-oz/A
Motor resistance	R	$5.0 \pm 12.5\%$	4.8	4.8	Ω
Motor inductance	L	$8.0 \pm 30\%$	—	—	mH

A.1.2 Voice coil motor

The back EMF for the voice coil motor (VCM) was measured via "pluck" tests with the outer flexure axis locked. The free response and measured back EMF voltage are shown in Fig. A.2. The four VCMs are connected in series, thus the measurement reflects the combined back EMF contributions from all four actuators. The total effective back EMF constant, K_b, is estimated from the slope of the least-squares linear fit of the data shown in Fig. A.2(b). The measured VCM parameter values are compared to the nominal manufacturer values in Table A.2. The effective torque constant, K_t, is calculated using a lever arm of 2.21 inches, which is the radius from the center of rotation to the VCM applied tangential force.

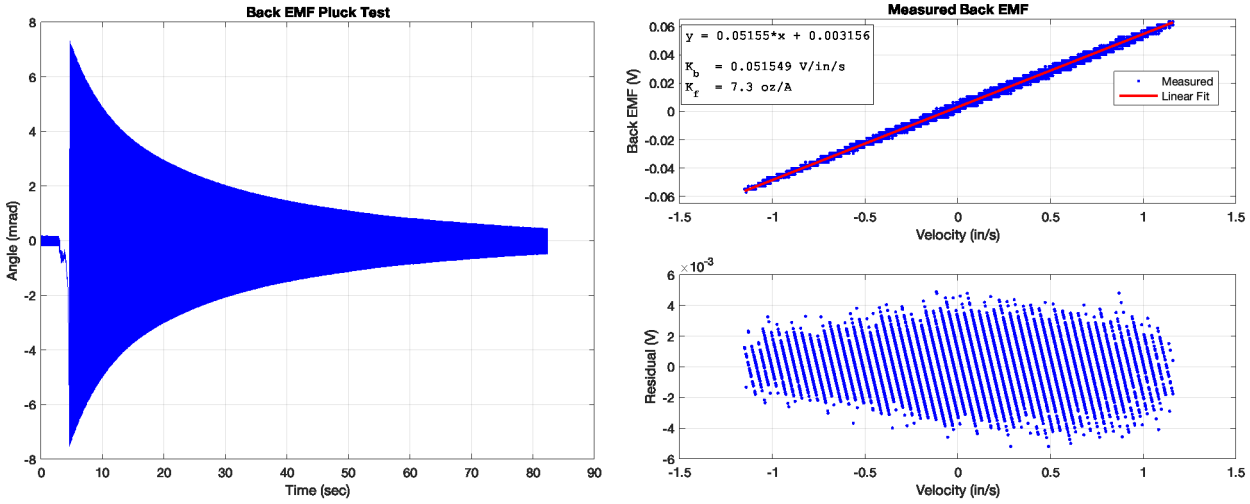

(a) Pluck test response

(b) Measured back EMF

Figure A.2: Voice coil motor back EMF measurements

Table A.2: Voice coil motor parameters

Parameter	**Symbol**	**Nominal (×4)**	**Measured**	**Units**
Back EMF constant	K_b	$0.01 \times 4 = 0.04$	0.05	V/in/s
Force constant	K_f	$1.6 \times 4 = 6.4$	7.3	oz/A
Effective torque constant (@2.21 in)	K_t	$3.54 \times 4 = 14.1$	16.1	in-oz/A
Motor resistance	R	$1.5 \times 4 = 6.0$	6.8	Ω
Motor inductance	L	$63 \times 4 = 252$	—	µH

A.2 Flexure Characterization

A.2.1 Quasistatic stiffness test

To determine the flexure stiffness, a slow torque ramp profile was applied to the VCM as shown in Fig. A.3(a). The applied torque is calculated as $T = K_t i_{\text{cmd}}$ where K_t is the effective VCM torque constant and i_{cmd} is the commanded motor current. The resulting torque versus displacement relationship is plotted in Figure A.3(b). The flexure stiffness is estimated from the slope of the least-squares linear fit of the data, yielding a rotational stiffness value of $k = 26.3$ in-oz/mrad (at 27 °C). It is important to note that the flexure stiffness is sensitive to changes in temperature. As discussed in [21–23], an interesting feature of the flexure is that its stiffness can be controlled by applying a temperature differential across the inner and outer flexure rings. However, to simplify testing in this study, all tests are conducted under ambient conditions without additional temperature controls. As a result, small variations in ambient temperature or internal heating will cause variations in flexure stiffness. Care is taken to note the stiffness for a given test condition so that models can be adjusted accordingly to better match test results.

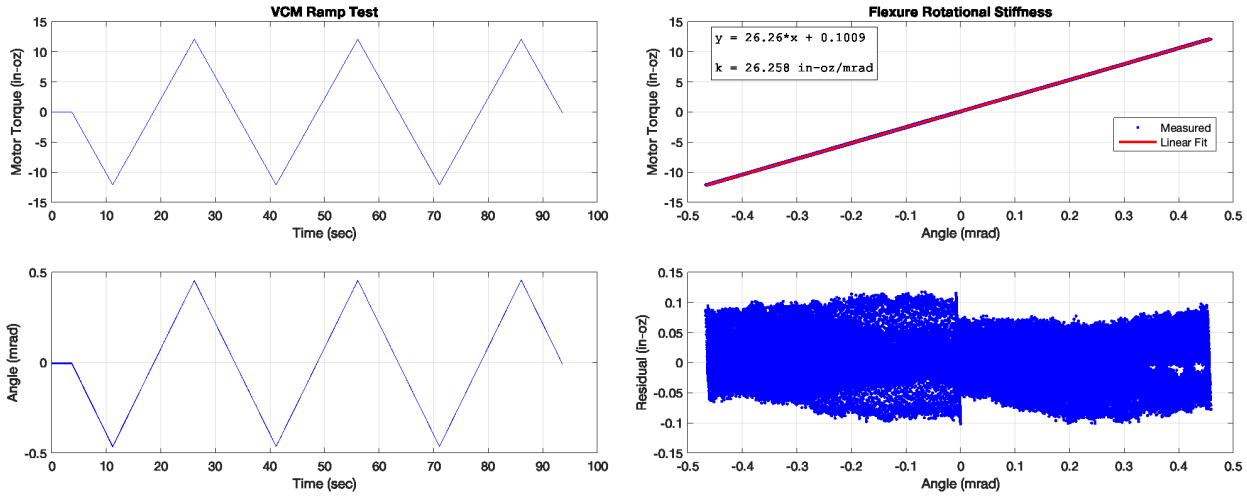

(a) VCM ramp test

(b) Flexure rotational stiffness

Figure A.3: Flexure stiffness measurement

A.2.2 Damping estimate

Damping estimates, via the logarithmic decrement method [128], were obtained from the free response of the inner axis with the outer axis locked. Initial test results yielded a linear decay envelope which is indicative of frictional rubbing (i.e., Coulomb friction). The testbed was disassembled and mechanical interference was discovered between the voice coil and magnet assembly. The voice coil was realigned to prevent rubbing. This improved the damping to approximately 0.1% as shown in Figure A.4. Note the amplitude dependent behavior of the damping ratio and damped natural frequency. This trend indicates a "stiffening spring" type behavior where larger displacements produce a higher natural frequency (i.e., stiffness). The measured flexure parameters are summarized in Table A.3.

Table A.3: Measured flexure parameters

Parameter	**Symbol**	**Value**	**Units**
Flexure stiffness (at 27 °C)	k	26300	in-oz/rad
Flexure damping coefficient	b	1.21	in-oz-s/rad

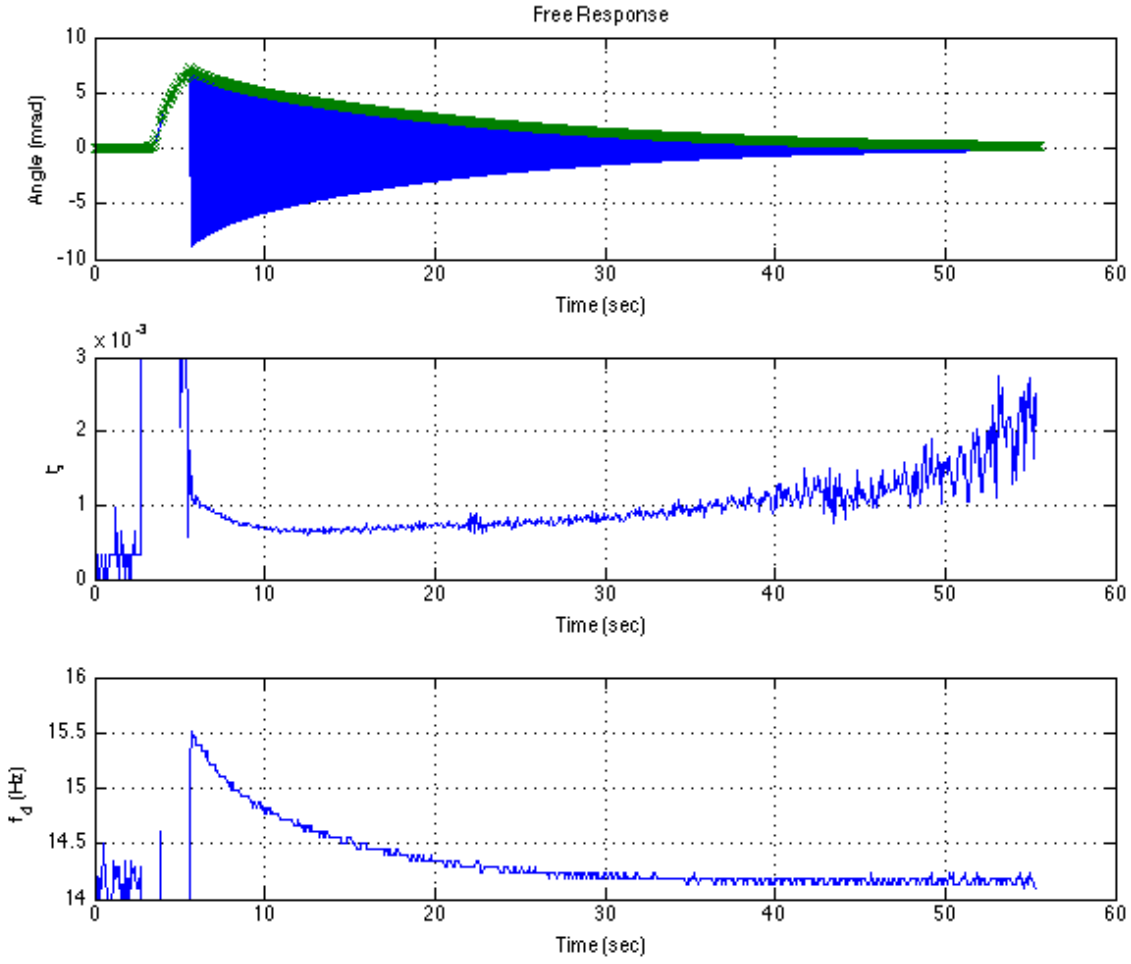

Figure A.4: Flexure damping estimate

A.3 Testbed Mass Properties

The testbed moments of inertia (MOIs) are obtained from CAD models or are determined empirically through system identification methods. Figure A.5 depicts the testbed components which contribute to the total moment of inertia about the axis of rotation. The experimentally validated inertia values for the various testbed components and total assemblies are given in Table A.4.

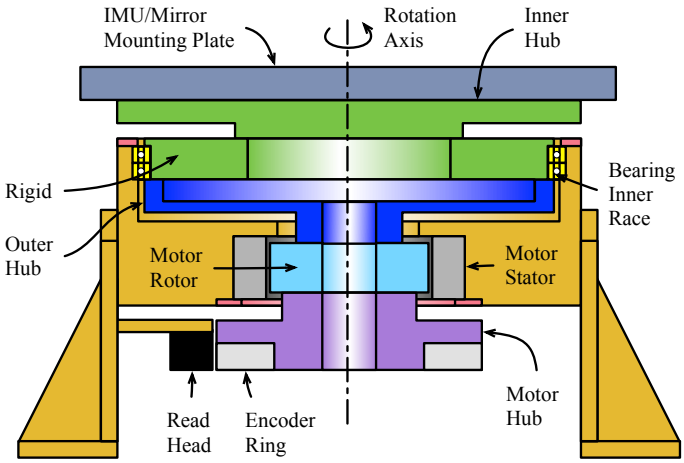

(a) 1-DOF testbed

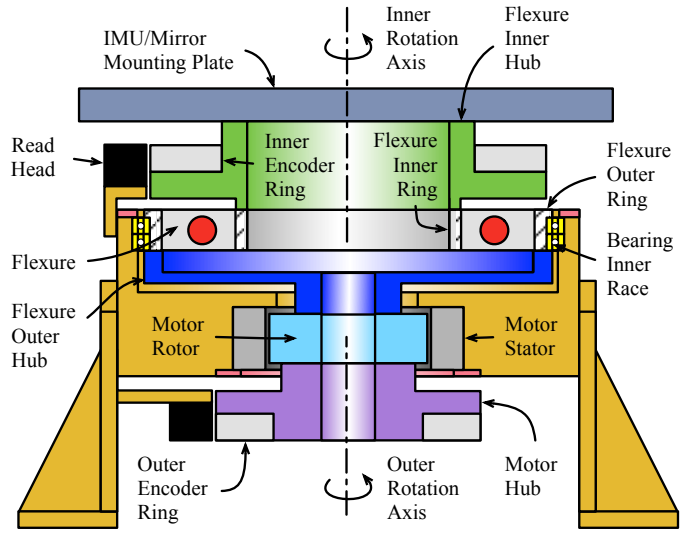

(b) 2-DOF testbed

Figure A.5: Testbed moments of inertia

Table A.4: Testbed moments of inertia

Component	**Value**	**Units**
Motor rotor	0.579	lb-in^2
Motor hub	1.01	lb-in^2
Flexure outer ring	2.822	lb-in^2
Flexure inner ring	0.419	lb-in^2
Flexure outer hub	3.891	lb-in^2
Flexure inner hub	5.291	lb-in^2
Rigid inner hub	11.9	lb-in^2
Bearing inner race (2x)	1.037	lb-in^2
Outer encoder ring	2.372	lb-in^2
Inner encoder ring	11.38	lb-in^2
IMU	1.151	lb-in^2
Mirror (as mounted)	4.995	lb-in^2
IMU/mirror mounting plate	19.9	lb-in^2
Disk inertia (optional)	52.9	lb-in^2
Totals (without plate/mirror/IMU)		
Rigid testbed, J	21.82	lb-in^2
Flexure testbed outer axis, J_1	12.75	lb-in^2
Flexure testbed inner axis, J_2	17.09	lb-in^2
Totals (with plate/mirror/IMU/disk)		
Rigid testbed, J	47.87	lb-in^2
Flexure testbed outer axis, J_1	65.65	lb-in^2
Flexure testbed inner axis, J_2	43.14	lb-in^2

A.4 Friction Characterization

A.4.1 Steady-state friction

A variety of constant velocity ramp profiles (0.01–50 deg/s) were run on each testbed to obtain the steady-state friction characteristics depicted in Figs. A.6 and A.7.

A.4.2 Dynamic friction

Dynamic (presliding) friction behavior was characterized using various amplitude triangular wave profiles to achieve a constant velocity of 0.001 deg/s in each direction. The resulting hysteresis curves are shown in Figs. A.8 and A.9. Highly repeatable torque ripple, due to bearing and/or motor irregularities, was observed in the measured data. The torque ripple was removed in post-processing using spectral decomposition to simplify hysteresis curve fitting.

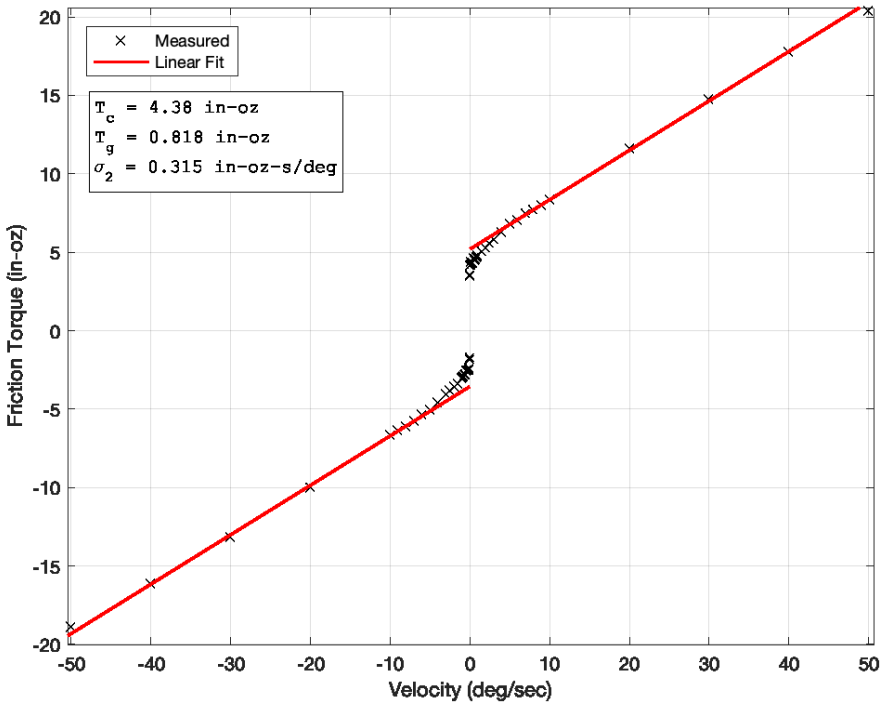

Figure A.6: Steady-state friction for the 1-DOF testbed

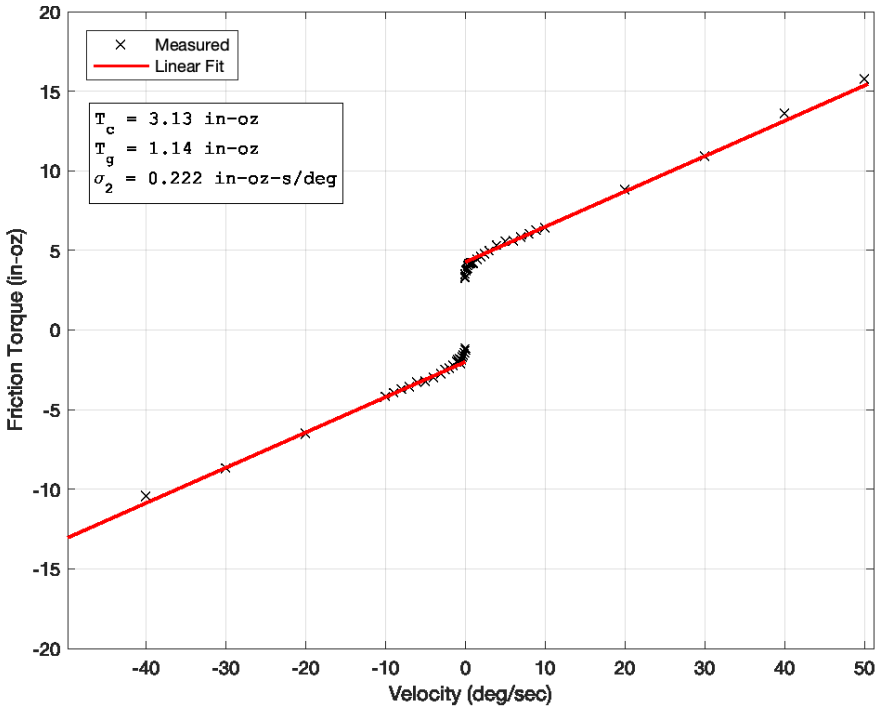

Figure A.7: Steady-state friction for the 2-DOF testbed

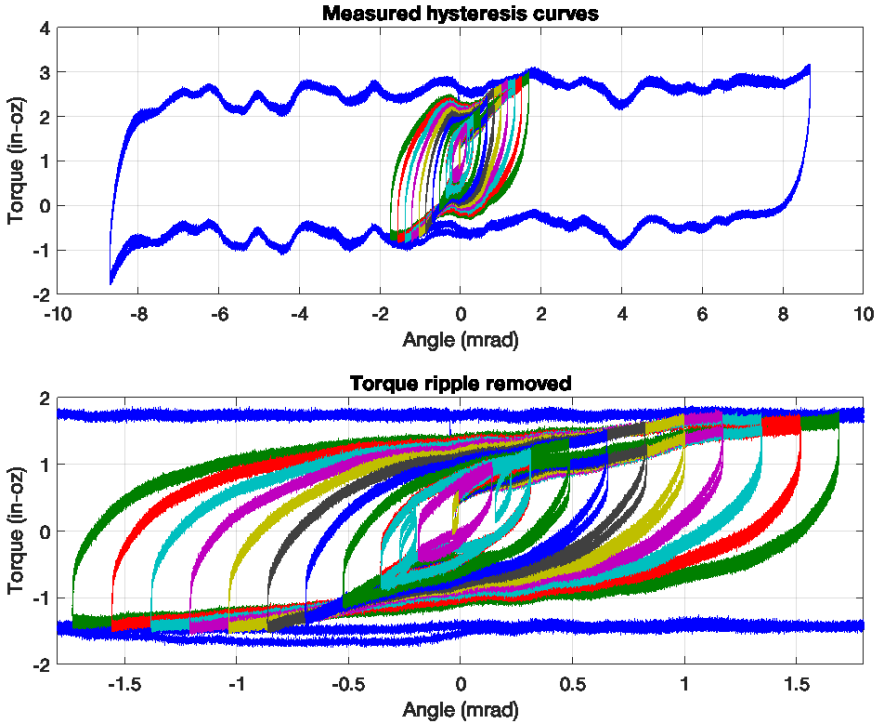

Figure A.8: Measured hysteresis curves for the 1-DOF testbed

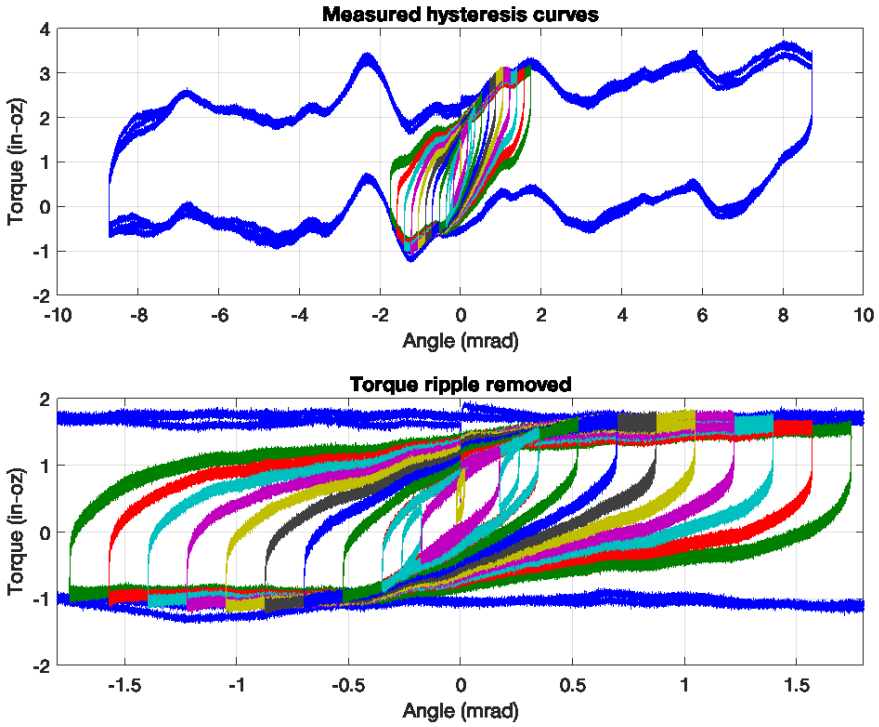

Figure A.9: Measured hysteresis curves for the 2-DOF testbed

A.5 System Identification and Nonlinear Model Validation

The nonlinear simulation is validated with experimental test data using frequency domain system identification techniques [61,62]. Comparisons are made between experimental and simulated FRFs in the figures on the following pages. The experimental FRFs were obtained by applying various amplitude, open-loop random excitations to the 2-DOF testbed. The same open-loop excitations were applied in the nonlinear simulation to generate the simulated FRFs. Note the good agreement between the experimental and simulated FRFs in all cases. Some FRF plots exhibit low frequency noise which is due to low coherence in certain cases as a result of slow drift in the experimental data. These system identification tests were used to facilitate estimation of the model parameters including:

- Outer axis inertia: J_1
- Inner axis inertia: J_2
- Flexure stiffness: k
- Flexure damping: b
- Linearized friction model parameters: k_f, b_f
- Sensor dynamics and delay

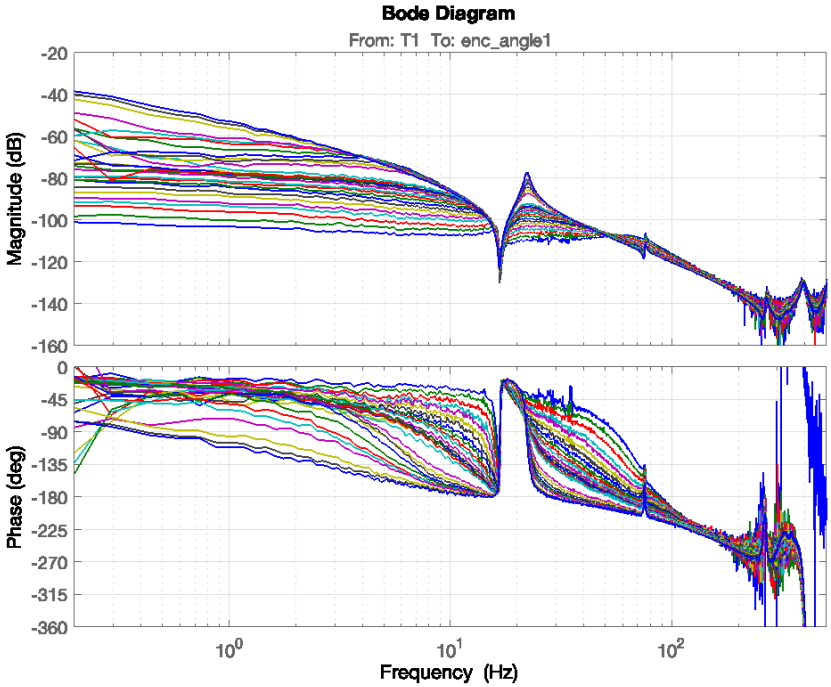

(a) Experimental FRFs

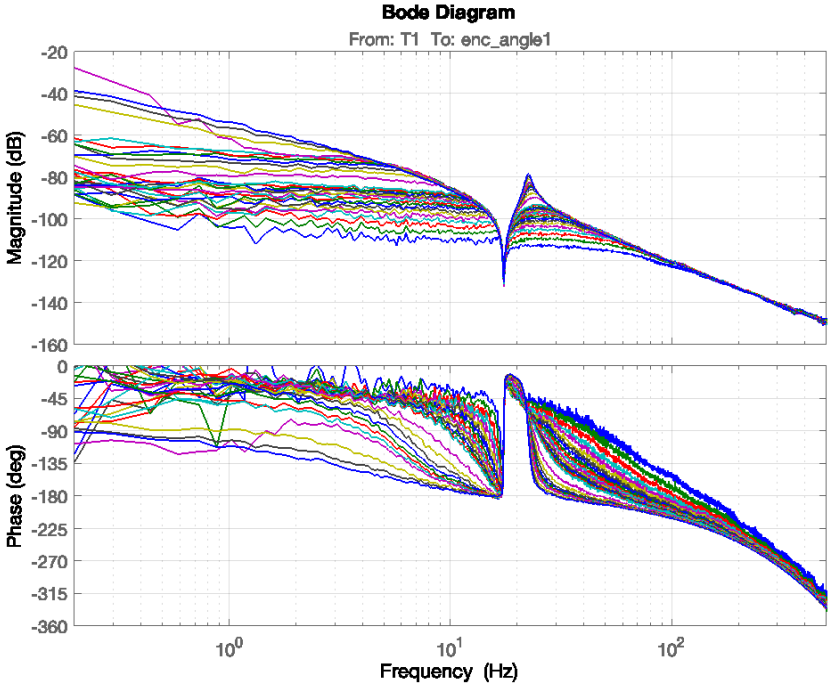

(b) Simulated FRFs

Figure A.10: Experimental and simulated FRFs from T_1 to ϕ_1

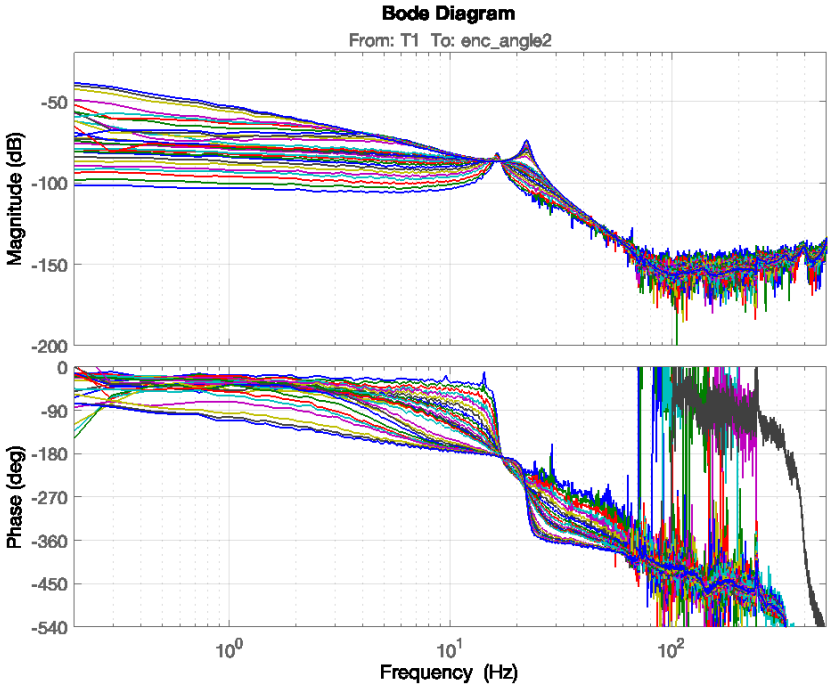

(a) Experimental FRFs

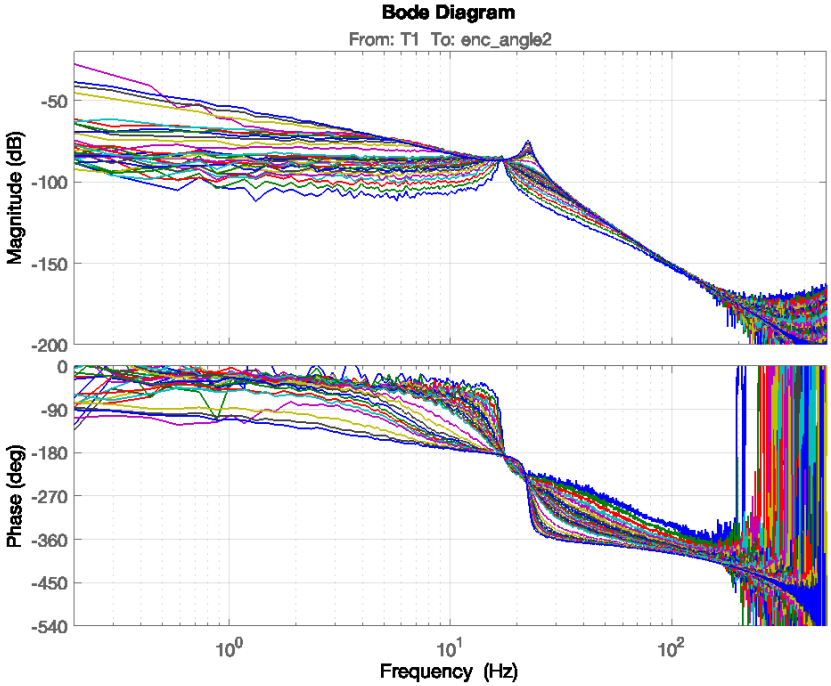

(b) Simulated FRFs

Figure A.11: Experimental and simulated FRFs from T_1 to ϕ_2

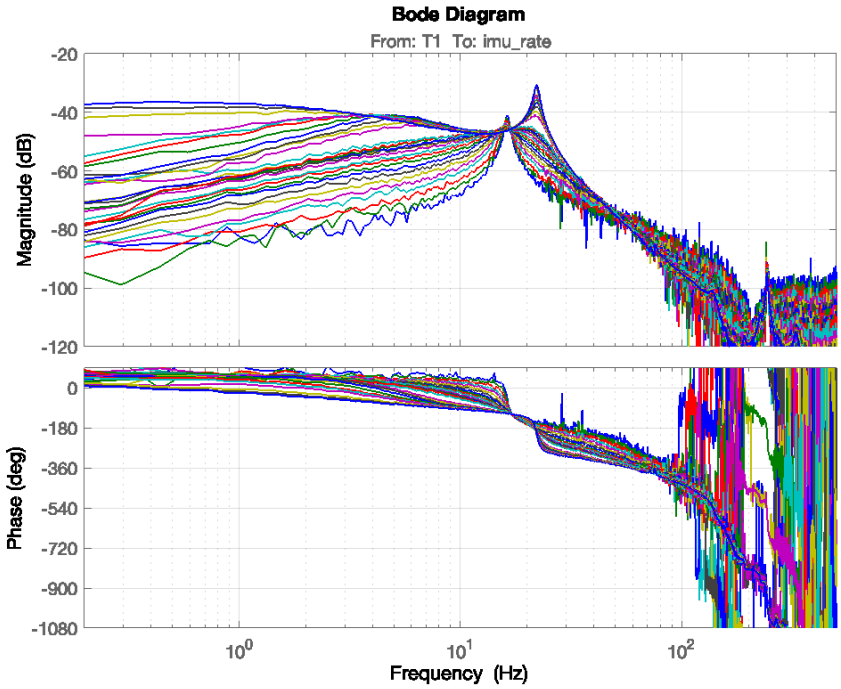

(a) Experimental FRFs

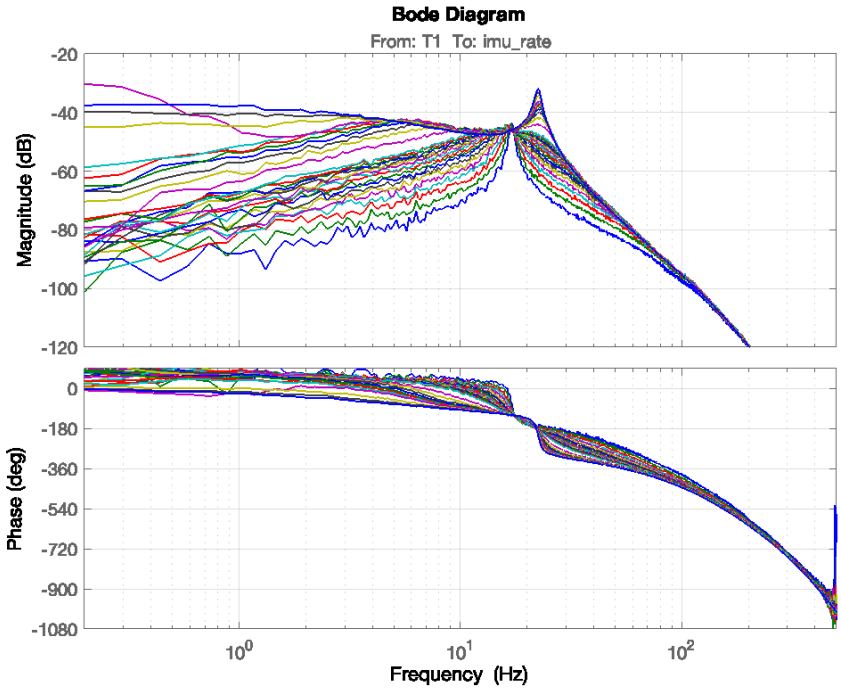

(b) Simulated FRFs

Figure A.12: Experimental and simulated FRFs from T_1 to $\dot{\theta}_2$

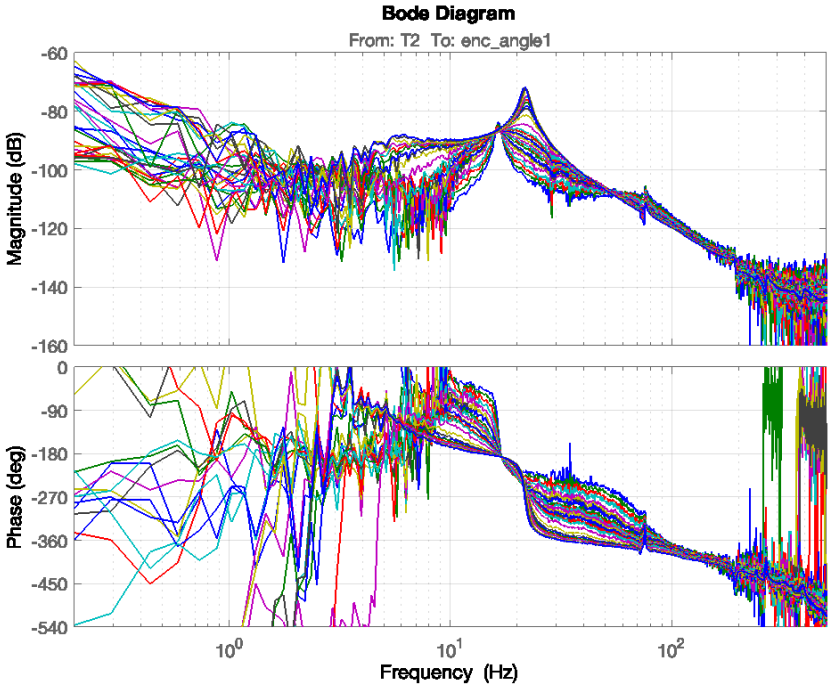

(a) Experimental FRFs

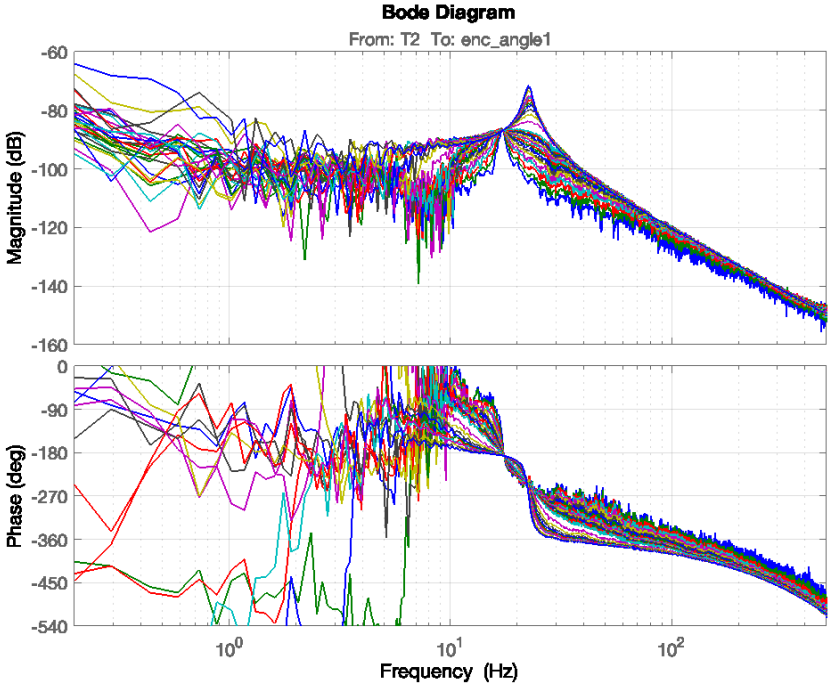

(b) Simulated FRFs

Figure A.13: Experimental and simulated FRFs from T_2 to ϕ_1

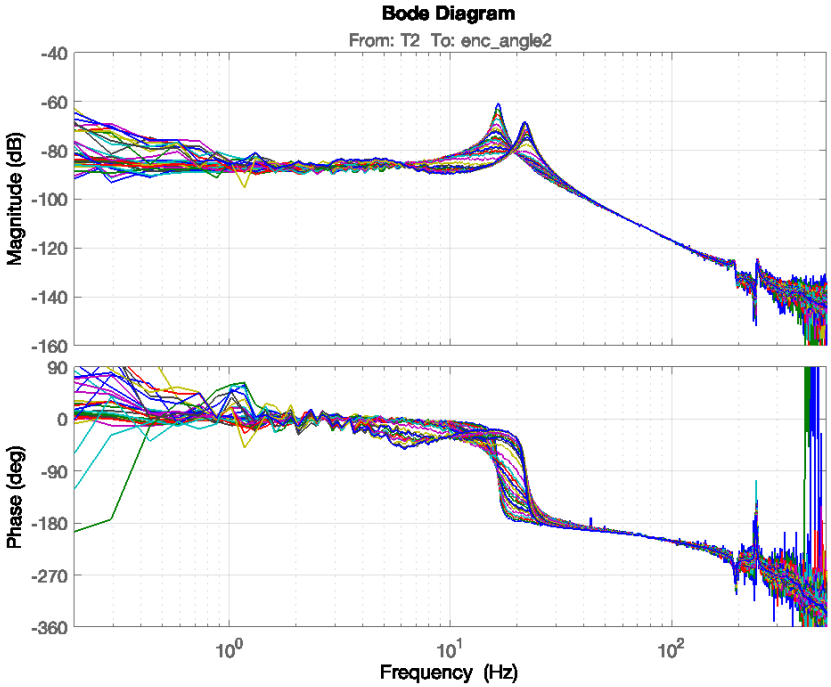

(a) Experimental FRFs

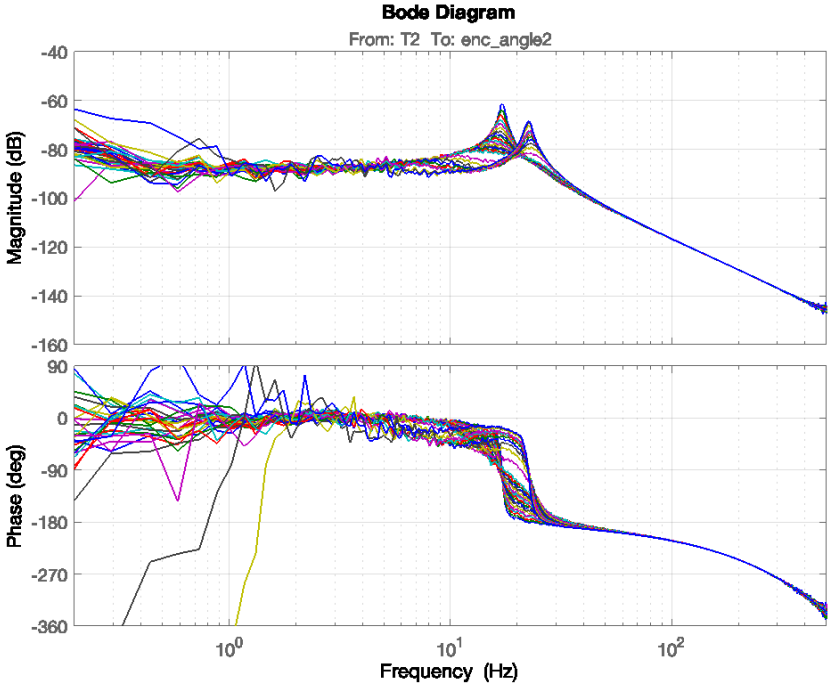

(b) Simulated FRFs

Figure A.14: Experimental and simulated FRFs from T_2 to ϕ_2

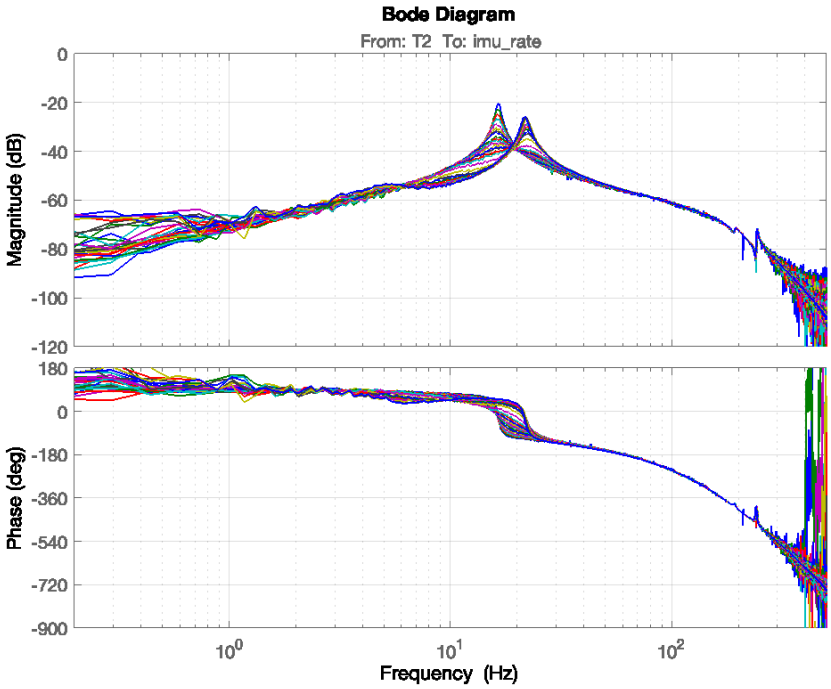

(a) Experimental FRFs

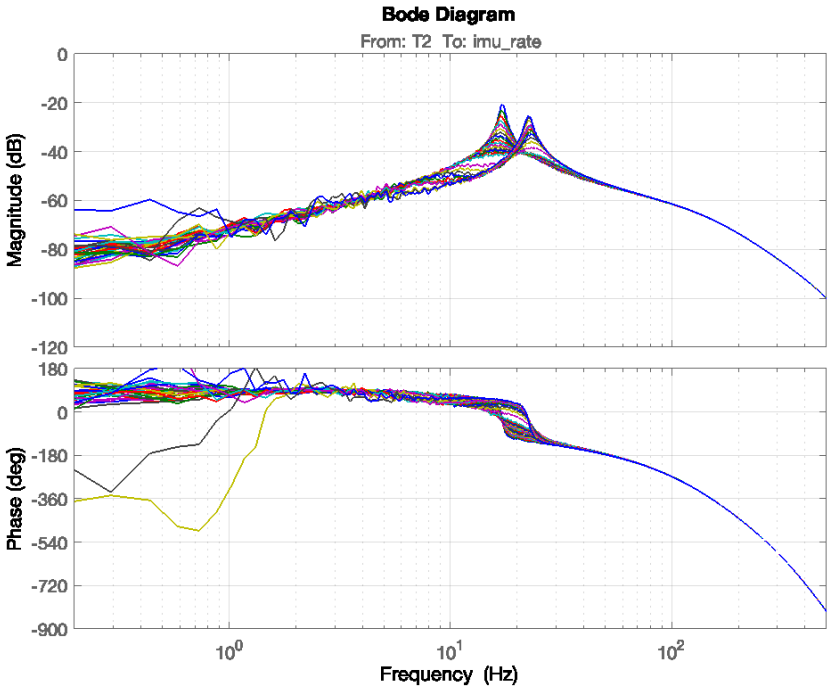

(b) Simulated FRFs

Figure A.15: Experimental and simulated FRFs from T_2 to $\dot{\theta}_2$

Appendix B

State Space Models

This appendix contains the derivation of the linear state space equations for the two different testbed configurations. The state space models are used in linear analysis and simulation.

B.1 1-DOF Testbed

B.1.1 Equations of motion

The equation of motion (EOM) for the 1-DOF testbed configuration, depicted in Fig. B.1(a), is expressed as

$$J\ddot{\theta} = T_m - T_f(\phi, \dot{\phi}) \tag{B.1}$$

where J is the moment of inertia about the rotation axis, θ is the inertial LOS angle, T_m is the applied motor torque, and T_f is the bearing friction torque. The friction torque, $T_f = T_f(\phi, \dot{\phi})$, is expressed as a general nonlinear function of the relative motion between the LOS and the base, where $\phi = \theta - \theta_b$ and $\dot{\phi} = \dot{\theta} - \dot{\theta}_b$.

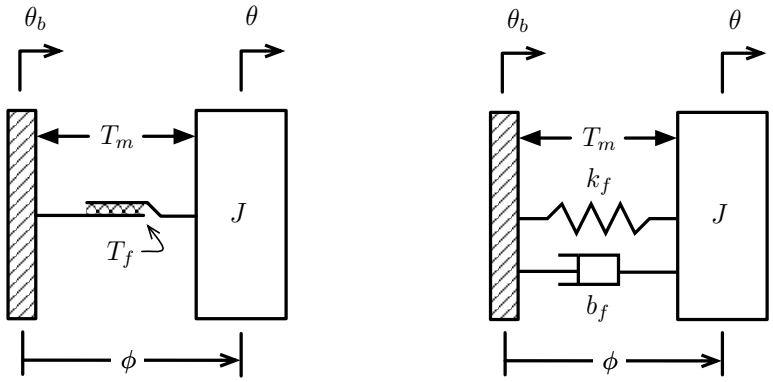

Figure B.1: 1-DOF testbed models with (a) nonlinear bearing friction and (b) linearized friction

To simplify analysis, a linear model is obtained under the assumption that presliding friction can be approximated by an effective linear stiffness, k_f, and viscous damping term, b_f, as depicted in Fig. B.1(b). This approximation is valid under certain steady-state operating conditions (i.e, small amplitude motion about a nominal position). Under these conditions, the friction torque can be expressed as a linear function of the relative motion between the base and the LOS

$$\begin{aligned} T_f &= T_f(\phi, \dot{\phi}) \\ &= k_f \phi + b_f \dot{\phi} \\ &= k_f(\theta - \theta_b) + b_f(\dot{\theta} - \dot{\theta}_b) \end{aligned} \tag{B.2}$$

where k_f is the effective frictional stiffness and b_f is the viscous damping coefficient. The linearized friction parameter values, k_f and b_f, depend on the particular operating condition or amplitude of motion. Combining Eqs. (B.1) and (B.2), the linearized EOM becomes

$$J\ddot{\theta} + b_f\dot{\theta} + k_f\theta = T_m + b_f\dot{\theta}_b + k_f\theta_b \tag{B.3}$$

B.1.2 Formulation 1: Base position disturbance

The states are chosen such that the base angular position is a disturbance input. Define the states as

$$x_1 = \dot{\theta} - \frac{b_f}{J}\theta_b \tag{B.4}$$

$$x_2 = \theta \tag{B.5}$$

The linearized EOM given in Eq. (B.3) can be expressed in state space form

$$\dot{x}_1 = \frac{1}{J}\left[-b_f\left(x_1 + \frac{b_f}{J}\theta_b\right) - k_f x_2 + T_m + k_f\theta_b\right] \tag{B.6}$$

$$\dot{x}_2 = x_1 + \frac{b_f}{J}\theta_b \tag{B.7}$$

In matrix form $\dot{x} = Ax + Bu$

$$\begin{bmatrix} \dot{x}_1 \\ \dot{x}_2 \end{bmatrix} = \begin{bmatrix} -\frac{b_f}{J} & -\frac{k_f}{J} \\ 1 & 0 \end{bmatrix} \begin{bmatrix} x_1 \\ x_2 \end{bmatrix} + \begin{bmatrix} \frac{1}{J} & \left(\frac{k_f}{J} - \frac{b_f^2}{J^2}\right) \\ 0 & \frac{b_f}{J} \end{bmatrix} \begin{bmatrix} T_m \\ \theta_b \end{bmatrix} \tag{B.8}$$

where the output equation is $y = Cx + Du$

$$\begin{bmatrix} \dot{\theta} \\ \theta \\ \phi \end{bmatrix} = \begin{bmatrix} 1 & 0 \\ 0 & 1 \\ 0 & 1 \end{bmatrix} \begin{bmatrix} x_1 \\ x_2 \end{bmatrix} + \begin{bmatrix} 0 & \frac{b_f}{J} \\ 0 & 0 \\ 0 & -1 \end{bmatrix} \begin{bmatrix} T_m \\ \theta_b \end{bmatrix} \tag{B.9}$$

B.1.3 Formulation 2: Base velocity disturbance

The states are chosen such that the base angular velocity is a disturbance input. Define the states as

$$x_1 = \dot{\theta} \tag{B.10}$$

$$x_2 = \theta - \theta_b = \phi \tag{B.11}$$

The linearized EOM given in Eq. (B.3) can be expressed in state space form

$$\dot{x}_1 = \frac{1}{J}\left[-b_f x_1 - k_f x_2 + T_m + b_f \dot{\theta}_b\right] \tag{B.12}$$

$$\dot{x}_2 = x_1 - \dot{\theta}_b \tag{B.13}$$

In matrix form $\dot{x} = Ax + Bu$

$$\begin{bmatrix} \dot{x}_1 \\ \dot{x}_2 \end{bmatrix} = \begin{bmatrix} -\frac{b_f}{J} & -\frac{k_f}{J} \\ 1 & 0 \end{bmatrix} \begin{bmatrix} x_1 \\ x_2 \end{bmatrix} + \begin{bmatrix} \frac{1}{J} & \frac{b_f}{J} \\ 0 & -1 \end{bmatrix} \begin{bmatrix} T_m \\ \dot{\theta}_b \end{bmatrix} \tag{B.14}$$

where the output equation is $y = Cx + Du$

$$\begin{bmatrix} \dot{\theta} \\ \phi \end{bmatrix} = \begin{bmatrix} 1 & 0 \\ 0 & 1 \end{bmatrix} \begin{bmatrix} x_1 \\ x_2 \end{bmatrix} \tag{B.15}$$

B.2 2-DOF Testbed

B.2.1 Equations of motion

The 2-DOF testbed is modeled by the lumped two-mass system shown in Fig. B.2(a). The 2-DOF testbed EOMs are derived by summing the moments about the outer and inner rotation axes, respectively. The EOMs can be expressed as a system of second-order ODEs

$$J_1\ddot{\theta}_1 - b(\dot{\theta}_2 - \dot{\theta}_1) - k(\theta_2 - \theta_1) = T_1 - T_2 - T_f(\phi_1, \dot{\phi}_1) \tag{B.16}$$

$$J_2\ddot{\theta}_2 + b(\dot{\theta}_2 - \dot{\theta}_1) + k(\theta_2 - \theta_1) = T_2 \tag{B.17}$$

where J_1 and J_2 are the moments of inertia of the outer and inner axes, k and b are the flexure stiffness and damping coefficient, T_1 and T_2 are the applied motor torques, and T_f is the ball bearing friction torque. The ball bearing friction torque, $T_f = T_f(\phi_1, \dot{\phi}_1)$, is expressed as a general nonlinear function of the relative motion between the outer axis and the base, where $\phi_1 = \theta_1 - \theta_b$ and $\dot{\phi}_1 = \dot{\theta}_1 - \dot{\theta}_b$.

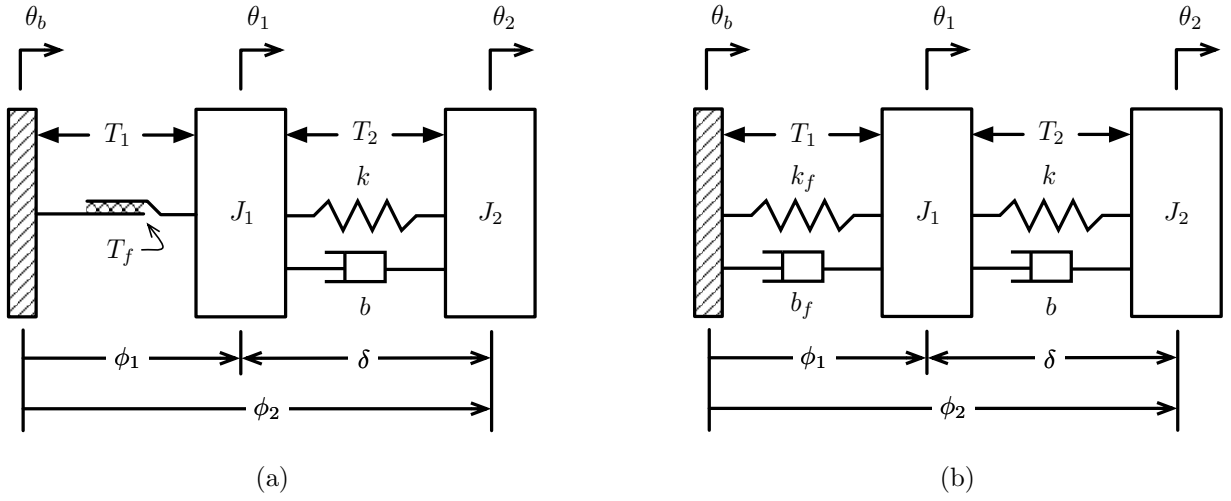

Figure B.2: 2-DOF testbed models with (a) nonlinear bearing friction and (b) linearized friction

To simplify analysis, a linear model is obtained under the assumption that presliding friction can be approximated by an effective linear stiffness, k_f, and viscous damping term, b_f, as depicted in Fig. B.2(b). This approximation is valid under certain steady-state operating conditions (i.e, small amplitude motion about a nominal position). Under these conditions, the friction torque can

be expressed as a linear function of the relative motion between the base and the outer axis

$$\begin{aligned} T_f &= T_f(\phi_1, \dot{\phi}_1) \\ &= k_f\phi_1 + b_f\dot{\phi}_1 \\ &= k_f(\theta_1 - \theta_b) + b_f(\dot{\theta}_1 - \dot{\theta}_b) \end{aligned} \tag{B.18}$$

where k_f is the effective frictional stiffness and b_f is the viscous damping coefficient. The linearized friction parameter values, k_f and b_f, depend on the particular operating condition or amplitude of motion. Combining Eqs. (B.16), (B.17), and (B.18), the linearized EOMs become

$$J_1\ddot{\theta}_1 + (b + b_f)\dot{\theta}_1 + (k + k_f)\theta_1 - b\dot{\theta}_2 - k\theta_2 = T_1 - T_2 + b_f\dot{\theta}_b + k_f\theta_b \tag{B.19}$$

$$J_2\ddot{\theta}_2 + b\dot{\theta}_2 + k\theta_2 - b\dot{\theta}_1 - k\theta_1 = T_2 \tag{B.20}$$

B.2.2 Formulation 1: Base position disturbance

The states are chosen such that the base angular position is a disturbance input. Define the states as

$$x_1 = \dot{\theta}_1 - \frac{b_f}{J_1}\theta_b \tag{B.21}$$

$$x_2 = \theta_1 \tag{B.22}$$

$$x_3 = \dot{\theta}_2 \tag{B.23}$$

$$x_4 = \theta_2 \tag{B.24}$$

The linearized EOMs given in Eqs. (B.19) and (B.20) can be expressed in state space form

$$\dot{x}_1 = \frac{1}{J_1}\left[-(b + b_f)x_1 - (k + k_f)x_2 + bx_3 + kx_4 + T_1 - T_2 + \left(k_f - \frac{b_f}{J_1}(b + b_f)\right)\theta_b\right] \tag{B.25}$$

$$\dot{x}_2 = x_1 + \frac{b_f}{J_1}\theta_b \tag{B.26}$$

$$\dot{x}_3 = \frac{1}{J_2}\left[bx_1 + kx_2 - bx_3 - kx_4 + T_2 + \frac{bb_f}{J_1}\theta_b\right] \tag{B.27}$$

$$\dot{x}_4 = x_3 \tag{B.28}$$

In matrix form $\dot{x} = Ax + Bu$

$$\begin{bmatrix} \dot{x}_1 \\ \dot{x}_2 \\ \dot{x}_3 \\ \dot{x}_4 \end{bmatrix} = \begin{bmatrix} -\frac{(b+b_f)}{J_1} & -\frac{(k+k_f)}{J_1} & \frac{b}{J_1} & \frac{k}{J_1} \\ 1 & 0 & 0 & 0 \\ \frac{b}{J_2} & \frac{k}{J_2} & -\frac{b}{J_2} & -\frac{k}{J_2} \\ 0 & 0 & 1 & 0 \end{bmatrix} \begin{bmatrix} x_1 \\ x_2 \\ x_3 \\ x_4 \end{bmatrix} + \begin{bmatrix} \frac{1}{J_1} & -\frac{1}{J_1} & \left(\frac{k_f}{J_1} - \frac{b_f(b+b_f)}{J_1^2}\right) \\ 0 & 0 & \frac{b_f}{J_1} \\ 0 & \frac{1}{J_2} & \frac{bb_f}{J_1 J_2} \\ 0 & 0 & 0 \end{bmatrix} \begin{bmatrix} T_1 \\ T_2 \\ \theta_b \end{bmatrix} \tag{B.29}$$

where the output equation is $y = Cx + Du$

$$\begin{bmatrix} \theta_1 \\ \dot{\theta}_1 \\ \theta_2 \\ \dot{\theta}_2 \\ \phi_1 \\ \phi_2 \\ \delta \end{bmatrix} = \begin{bmatrix} 0 & 1 & 0 & 0 \\ 1 & 0 & 0 & 0 \\ 0 & 0 & 0 & 1 \\ 0 & 0 & 1 & 0 \\ 0 & 1 & 0 & 0 \\ 0 & 0 & 0 & 1 \\ 0 & -1 & 0 & 1 \end{bmatrix} \begin{bmatrix} x_1 \\ x_2 \\ x_3 \\ x_4 \end{bmatrix} + \begin{bmatrix} 0 & 0 & 0 \\ 0 & 0 & \frac{b_f}{J_1} \\ 0 & 0 & 0 \\ 0 & 0 & 0 \\ 0 & 0 & -1 \\ 0 & 0 & -1 \\ 0 & 0 & 0 \end{bmatrix} \begin{bmatrix} T_1 \\ T_2 \\ \theta_b \end{bmatrix} \tag{B.30}$$

B.2.3 Formulation 2: Base velocity disturbance

The states are chosen such that the base angular velocity is a disturbance input. The states are defined as

$$x_1 = \dot{\theta}_1 \tag{B.31}$$

$$x_2 = \theta_1 - \theta_b = \phi_1 \tag{B.32}$$

$$x_3 = \dot{\theta}_2 \tag{B.33}$$

$$x_4 = \theta_2 - \theta_1 = \delta \tag{B.34}$$

The linearized EOMs given in Eqs. (B.19) and (B.20) can be expressed in state space form

$$\dot{x}_1 = \frac{1}{J_1}\left[-(b+b_f)x_1 - k_f x_2 + b x_3 + k x_4 + T_1 - T_2 + b_f \dot{\theta}_b\right] \tag{B.35}$$

$$\dot{x}_2 = x_1 - \dot{\theta}_b \tag{B.36}$$

$$\dot{x}_3 = \frac{1}{J_2}\left[b x_1 - b x_3 - k x_4 + T_2\right] \tag{B.37}$$

$$\dot{x}_4 = x_3 - x_1 \tag{B.38}$$

In matrix form $\dot{x} = Ax + Bu$

$$\begin{bmatrix} \dot{x}_1 \\ \dot{x}_2 \\ \dot{x}_3 \\ \dot{x}_4 \end{bmatrix} = \begin{bmatrix} -\frac{(b+b_f)}{J_1} & -\frac{k_f}{J_1} & \frac{b}{J_1} & \frac{k}{J_1} \\ 1 & 0 & 0 & 0 \\ \frac{b}{J_2} & 0 & -\frac{b}{J_2} & -\frac{k}{J_2} \\ -1 & 0 & 1 & 0 \end{bmatrix} \begin{bmatrix} x_1 \\ x_2 \\ x_3 \\ x_4 \end{bmatrix} + \begin{bmatrix} \frac{1}{J_1} & -\frac{1}{J_1} & \frac{b_f}{J_1} \\ 0 & 0 & -1 \\ 0 & \frac{1}{J_2} & 0 \\ 0 & 0 & 0 \end{bmatrix} \begin{bmatrix} T_1 \\ T_2 \\ \dot{\theta}_b \end{bmatrix} \tag{B.39}$$

where the output equation is $y = Cx + Du$

$$\begin{bmatrix} \dot{\theta}_1 \\ \dot{\theta}_2 \\ \phi_1 \\ \phi_2 \\ \delta \end{bmatrix} = \begin{bmatrix} 1 & 0 & 0 & 0 \\ 0 & 0 & 1 & 0 \\ 0 & 1 & 0 & 0 \\ 0 & 1 & 0 & 1 \\ 0 & 0 & 0 & 1 \end{bmatrix} \begin{bmatrix} x_1 \\ x_2 \\ x_3 \\ x_4 \end{bmatrix} \tag{B.40}$$

Appendix C

Simulink Models

This appendix contains details regarding the implementation of the dynamic friction models discussed in Section 3.2.

C.1 Friction Model Implementation

Four different friction models, depicted in Fig. C.1, are evaluated: SFM, DHM, DB-SFM, and DB-DHM. Figure C.2 shows the Simulink diagrams for each friction model.

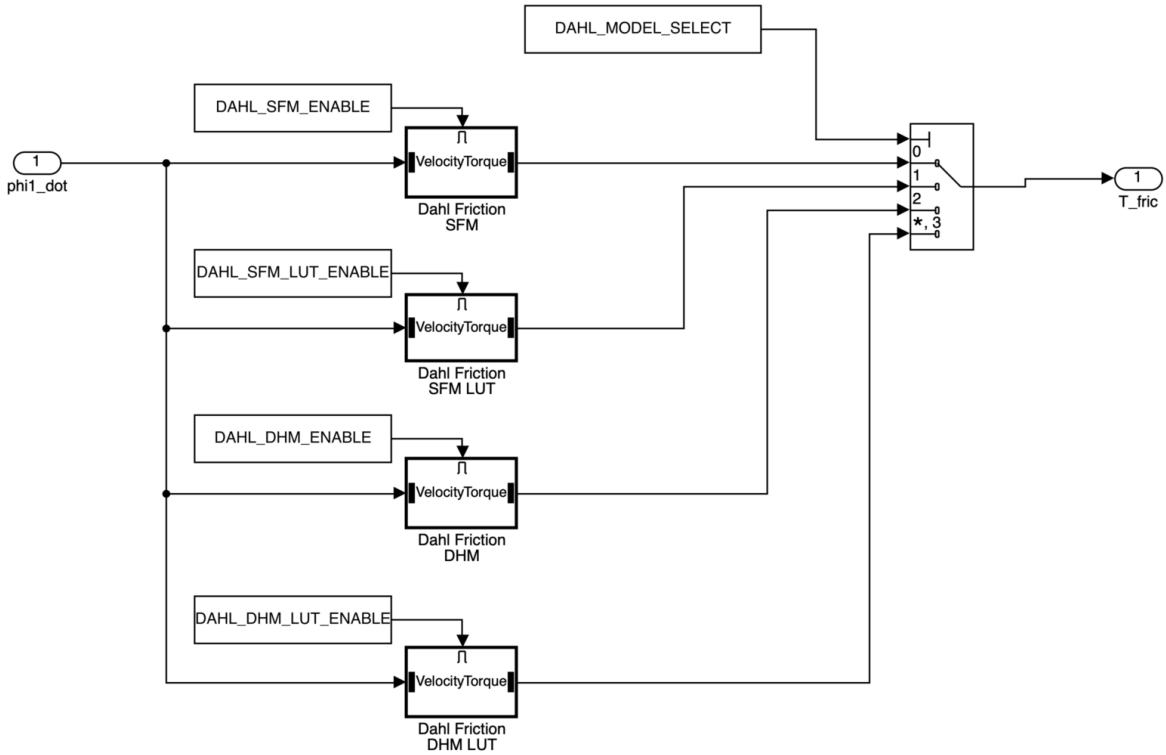

Figure C.1: Friction model implementation

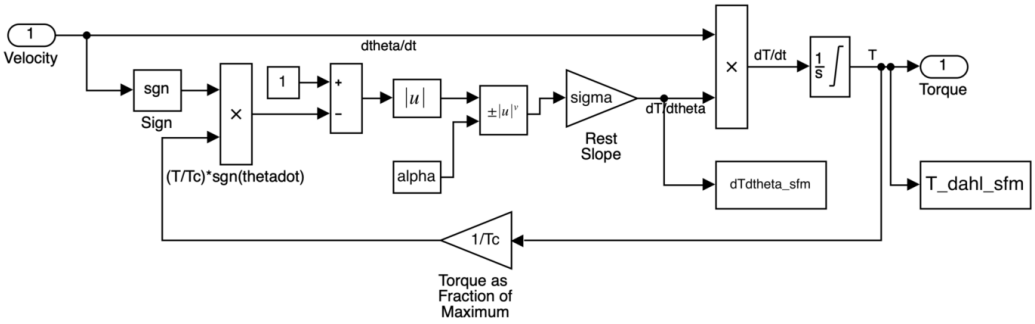

(a)

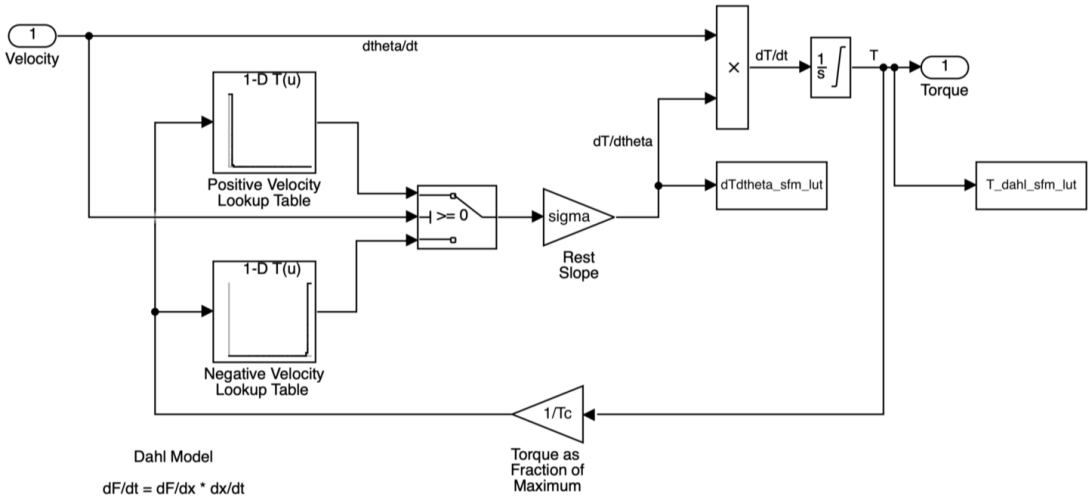

(b)

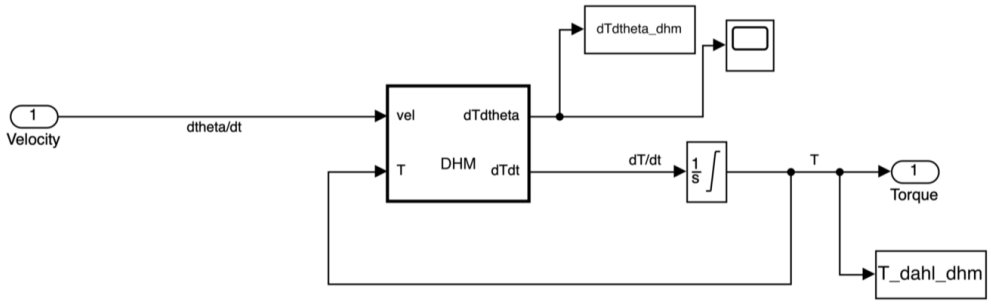

(c)

Figure C.2: Simulink models: (a) SFM, (b) DB-SFM, (c) DHM and DB-DHM

C.1.1 DHM code

The DHM block, depicted in Fig. C.2(c), is implemented using a custom MATLAB function. The code for this MATLAB function is given below.

```
function [dTdtheta, dTdt] = DHM(vel, T, sigma, Tc, alpha)
%#codegen

persistent k f vold init err lutxp lutyp lutxn lutyn
max_states = 100000;

if isempty(init)
  k = 0;
  if vel >= 0
    k = 2;
  end
  if vel < 0
    k = 3;
  end
  f = zeros(max_states,1);
  f(3) = Tc;
  f(2) = -Tc;
  err = Tc/400;
  vold = vel;
end

if mysign(vel) == mysign(vold)  % Check for velocity reversal
  % Continue on current branch
  if k > 2        % If on minor loop branch
    if abs(T+err-f(k)) >= abs(f(k)-f(k-1))  % Check for minor loop closure
      k = k - 2;  % Minor loop closed, forget last two branches
    end
  end
else  % If velocity reversal
  k = k + 1;      % Start new reversed branch
  if k > max_states
    k = 3;
    f = zeros(max_states,1);
    f(3) = T;
    f(2) = T;
    fprintf('Exceeded %f friction states... resetting!\n', max_states);
  end
  f(k) = T;       % Store turnaround friction
end

init = true;      % Flag as initialized
```

```
42  vold = vel;       % Store current velocity for next time through
43
44  % Compute the value of the friction slope function from the model
45  dTdtheta = sigma*((2 - mysign(vel)*(T - f(k))/Tc))^alpha;
46
47  % Ensure the slope function is always non-negative
48  if dTdtheta < 0
49    dTdtheta = 0;
50  end
51
52  % Make sure any extrapolation is bounded
53  dTdtheta_max = sigma*lutyp(1);
54  if dTdtheta > dTdtheta_max
55    dTdtheta = dTdtheta_max;
56  end
57
58  % Compute the time derivative of the friction torque
59  dTdt = vel*dTdtheta;
60
61  % Define my own sign function since the Matlab built-in function returns
62  % sign(0) = 0
63  function y = mysign(x)
64  y = -1;
65  if x >= 0
66    y = 1;
67  end
```

C.1.2 DB-DHM code

The DB-DHM block, depicted in Fig. C.2(c), is implemented with a custom MATLAB function. The code for this MATLAB function is given below.

```
function [dTdtheta, dTdt] = DHM(vel, T, sigma, Tc, lutx, luty)
%#codegen

persistent k f vold init err lutxp lutyp lutxn lutyn
max_states = 100000;

if isempty(init)
  k = 0;
  if vel >= 0
    k = 2;
  end
  if vel < 0
    k = 3;
  end
  f = zeros(max_states,1);
  f(3) = Tc;
  f(2) = -Tc;
  err = Tc/400;
  vold = vel;
  % Shift lutx to be in range [0, 2]
  lutxp = lutx + 1;
  lutyp = luty;
  % Mirror negative velocity LUT across vertical axis
  lutxn = -flip(lutxp);
  lutyn = flip(lutyp);
end

if mysign(vel) == mysign(vold)  % Check for velocity reversal
  % Continue on current branch
  if k > 2        % If on minor loop branch
    if abs(T+err-f(k)) >= abs(f(k)-f(k-1))  % Check for minor loop closure
      k = k - 2;  % Minor loop closed, forget last two branches
    end
  end
else  % If velocity reversal
  k = k + 1;      % Start new reversed branch
  if k > max_states
    k = 3;
    f = zeros(max_states,1);
    f(3) = T;
    f(2) = T;
```

```
42      fprintf('Exceeded %f friction states... resetting!\n', max_states);
43    end
44    f(k) = T;       % Store turnaround friction
45  end
46
47  init = true;      % Flag as initialized
48  vold = vel;       % Store current velocity for next time through
49
50  % Compute the value of the friction slope function from the LUT
51  if mysign(vel) >= 0
52    dTdtheta = sigma*interp1(lutxp, lutyp, (T - f(k))/Tc, 'linear', 'extrap');
53  else
54    dTdtheta = sigma*interp1(lutxn, lutyn, (T - f(k))/Tc, 'linear', 'extrap');
55  end
56
57  % Ensure the slope function is always non-negative
58  if dTdtheta < 0
59    dTdtheta = 0;
60  end
61
62  % Make sure any extrapolation is bounded
63  dTdtheta_max = sigma*lutyp(1);
64  if dTdtheta > dTdtheta_max
65    dTdtheta = dTdtheta_max;
66  end
67
68  % Compute the time derivative of the friction torque
69  dTdt = vel*dTdtheta;
70
71  % Define my own sign function since the Matlab built-in function returns
72  % sign(0) = 0
73  function y = mysign(x)
74  y = -1;
75  if x >= 0
76    y = 1;
77  end
```